

ESD ACCESSION LIST

TRI Call No.

Copy No.

73346

of

2

REV

ESD RECORD COPY

RETURN TO

SCIENTIFIC & TECHNICAL INFORMATION DIVISION
(TRI), Building 1210

4

Solid State Research

1971

Prepared under Electronic Systems Division Contract F19628-70-C-0230 by

Lincoln Laboratory

MASSACHUSETTS INSTITUTE OF TECHNOLOGY

Lexington, Massachusetts



A0736501

Approved for public release; distribution unlimited.

/

4

1971

Solid State Research

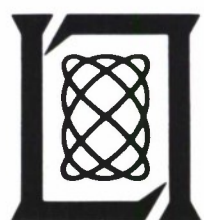
Issued 26 January 1972

Prepared under Electronic Systems Division Contract F19628-70-C-0230 by

Lincoln Laboratory

MASSACHUSETTS INSTITUTE OF TECHNOLOGY

Lexington, Massachusetts



Approved for public release; distribution unlimited.

U.S. AIR FORCE-7 FEBRUARY 1972 (37360/930)

The work reported in this document was performed at Lincoln Laboratory, a center for research operated by Massachusetts Institute of Technology, with the support of the Department of the Air Force under Contract F19628-70-C-0230.

This report may be reproduced to satisfy needs of U.S. Government agencies.

Non-Lincoln Recipients
PLEASE DO NOT RETURN

Permission is given to destroy this document
when it is no longer needed.

ABSTRACT

This report covers in detail the solid state research work of the Solid State Division at Lincoln Laboratory for the period 1 August through 31 October 1971. The topics covered are Solid State Device Research, Quantum Electronics, Materials Research, Physics of Solids and Microelectronics. The Microsound work is sponsored by ABMDA and is reported under that program.

Accepted for the Air Force
Joseph R. Waterman, Lt. Col., USAF
Chief, Lincoln Laboratory Project Office

CONTENTS

Abstract	iii
Introduction	vii
Reports on Solid State Research	xi
Organization	xvii
I. SOLID STATE DEVICE RESEARCH	1
A. p-n Junction Photodiodes in PbTe Prepared by Sb ⁺ Ion Implantation	1
B. Electrical Characteristics of Guarded n-p InSb Photodiodes Fabricated by Proton Bombardment	1
1. Diode Fabrication	2
2. MOS Measurements	3
3. Diode C-V Measurements	5
4. Diode I-V Measurements	7
C. High Gain GaAs Schottky-Barrier Avalanche Photodiodes	11
D. ZnO/GaAs Overlay Transducers	13
E. X-Ray Lithography: A High Resolution Replication Process	13
F. Observation of the Far Field Mode Pattern of a PbTe Diode Laser Using Upconversion in a ZnS Phosphor	17
G. Calibration of Tunable Diode Lasers Using a Confocal Fabry-Perot Interferometer	17
H. Stripe-Geometry - Pb _{1-x} Sn _x Te Diode Lasers	19
II. QUANTUM ELECTRONICS	23
A. Optically Pumped Room Temperature In _x Ga _{1-x} As Lasers	23
B. Determination of the ν_1 -Band Center of SO ₂ by Tunable Laser Spectroscopy	25
C. Raman Scattering in Paratellurite: Tellurium Dioxide	27
III. MATERIALS RESEARCH	31
A. Czochralski Growth of FeO Single Crystals	31
B. Oxidizing Potential of Some Laboratory Gases	33
C. Influence of Madelung Energy and Covalency on the Structure of A ⁺ B ⁵⁺ O ₃ Compounds	35
D. Structure of V _{0.95} Cr _{0.05} O ₂	36
E. Effect of Pressure on the Magnetic Behavior of MnP	37
IV. PHYSICS OF SOLIDS	43
A. Secondary Electron Emission	43
B. Phosphor Upconversion	44
1. Rare Earth Phosphors for Near-Infrared to Visible Upconversion	44
2. Infrared Stimulation of Visible Luminescence in ZnS Phosphors	45
C. Metal-Insulator Transitions	47
1. Material Preparation and Characterization	47
2. Model of Electronic Switching	48

D. High Resolution Laser Spectroscopy	49
1. Pressure-Induced Line Shift and Broadening in the Vibration-Rotation Spectrum of CO	49
2. Observation of Zeeman Splitting and Lambda Doubling in NO	50
3. Infrared Magnetic Rotation in NO	53
4. Laser Light Scattering in Antiferromagnets	54
E. Electronic Band Structure	55
1. Infrared Laser Determination of Effective Mass in GaAs-InAs Alloys	55
2. Resistivity of $Pb_{1-x}Sn_xSe$ Under Hydrostatic Pressure	57
V. MICROELECTRONICS	61
A. Aluminum Interconnections and Beam Leads on Polyimide- Coated, Thin, Copper Substrates	61
B. Semiconductor Program	61
C. Mask Making Laboratory	63
D. Bonding and Packaging	63
E. Integrated Circuit Testing	64

INTRODUCTION

I. SOLID STATE DEVICE RESEARCH

High quality n-p junction photodiodes have been fabricated in p-type PbTe using Sb⁺ ion implantation to form the n-type regions. At 77°K, 15-mil-square diodes have exhibited zero bias impedances as high as 15 megohms and peak detectivities at 4.4 μ m in reduced background as high as 1.5×10^{12} cmHz^{1/2}/W. This value appears to be limited by amplifier noise.

The surface properties and current-voltage characteristics of planar n-p InSb photodiodes fabricated by proton bombardment have been investigated in diode structures with annular guard rings formed by peripheral field plates. Low surface state densities were obtained by passivation with pyrolytic SiON, which allowed the surface potential to be controlled by the field plate. At an optimum field-plate voltage, diode leakage currents as small as 11 nA for a 13-mil-diameter device have been observed at a reverse-bias voltage of -1.0V.

High-gain GaAs Schottky barrier avalanche photodiodes have been fabricated using Pt barriers on lightly doped n-type GaAs epitaxial layers. Guard rings were formed using proton bombardment. Small signal gains as large as 4500 were measured on $n = 2.5 \times 10^{14}$ cm⁻³ material compared with 100 to 300 observed previously on more heavily doped $n \cong 10^{16}$ cm⁻³ material.

Coupling to GaAs acoustic surface waves was increased by more than a factor of four by sputtering a 2.5- μ m ZnO film over the interdigital transducers, the radiation impedance being increased to 17 ohms. Calculations indicate that another factor-of-five improvement should be possible using this technique.

A pattern replication process utilizing soft x-rays has been developed which is capable of submicron resolution over areas of several square centimeters. By using soft x-rays instead of ultraviolet radiation, the wavelength related diffraction problems which limit the resolution of photolithography are effectively eliminated. This technique has been demonstrated using a chrome-gold transducer pattern with 2.5- μ m spacings on a 3.5- μ m-thick membrane of epitaxial Si.

Far-field patterns of a 6.5- μ m PbTe diode laser have been directly observed using the infrared upconversion properties of ZnS phosphor powder excited by ultraviolet light. A complex spatial mode pattern was observed, although 80 percent of the laser power was in a single frequency mode. This may be due to complex internal reflection of the mode.

A confocal Fahry-Perot interferometer has been used to accurately calibrate the tuning rate of current-tuned PbS_{1-x}Se_x diode lasers operating near 5.2 μ m. This technique provides a convenient and precise method for calibrating the tuning rate of tunable infrared laser sources.

In order to avoid off-axis and parasitic modes which occur in conventional rectangular diode laser structures, 50- μm -wide, 500- μm -long stripe geometry lasers have been fabricated in vapor-grown $\text{Pb}_{0.88}\text{Sn}_{0.12}\text{Te}$. The laser frequency spectra consisted of regularly spaced modes corresponding to the longitudinal cavity. The far-field pattern was a single lobe with beam angles of 20° in the vertical plane and 8° in the horizontal plane, corresponding to the fundamental spatial mode of the emitting region.

II. QUANTUM ELECTRONICS

Studies have been continued on room temperature $\text{In}_x\text{Ga}_{1-x}\text{As}$ lasers optically pumped by a Q-switched Nd:YAG laser. Above threshold, the axial-mode spacing was found to be 0.9 nm, in close agreement with the theoretical value for the 150- μm cavity. Pump threshold intensities were estimated to be on the order of 10⁵ W/cm² and conversion efficiencies up to 1 percent were observed.

Tunable laser spectroscopy has been carried out on the ν_1 -band of SO_2 using a lead-tin-telluride diode laser. A value of $1151.72 \pm 0.01 \text{ cm}^{-1}$ has been found for the band center. The Raman spectra of TeO_2 in the tetragonal D_4^4 (paratellurite) form have been obtained. All Raman active optical branches have been observed except $1\text{A}_1 + 2\text{E}$ and have been identified by their polarization selection rules. The observations indicate large polarizabilities and weak anharmonic forces, which is in agreement with the observed strong acousto-optic properties of this material.

III. MATERIALS RESEARCH

Wüstite (FeO) crystals of centimeter dimensions have been pulled from the melt in a tri-arc Czochralski furnace. Single crystals were easily grown when the melt composition was $\text{FeO}_{1.094}$, but polycrystalline boules were obtained for melt compositions of $\text{FeO}_{1.08}$ and $\text{FeO}_{1.12}$.

An oxygen meter utilizing stabilized zirconia as a solid-state electrolyte has been used to measure the oxidizing potential of several laboratory gases subjected to various treatments. Gettering with hot titanium foil or chips is found to be an effective method for reducing the oxygen content of argon and hydrogen.

In order to study the factors influencing the structure of $\text{A}^+\text{B}^{5+}\text{O}_3$ compounds, four new compounds of this type have been synthesized at high pressures and retained in metastable form at atmospheric pressure. Both RbNbO_3 (orthorhombic) and RbTaO_3 (cubic) are perovskites, but as a result of the strong Sb-O covalency RbSbO_3 and TiSbO_3 are not.

The results of a more detailed x-ray diffraction study of powdered $\text{V}_{0.95}\text{Cr}_{0.05}\text{O}_2$ are consistent with the orthorhombic structure previously assigned to this material, but do not conclusively rule out the monoclinic structure which has been established for $\text{V}_{0.976}\text{Cr}_{0.024}\text{O}_2$. Therefore, a single crystal investigation has been undertaken to obtain an unambiguous structure determination for $\text{V}_{0.95}\text{Cr}_{0.05}\text{O}_2$.

The effect of pressure on the magnetic behavior of MnP, which is ferromagnetic at atmospheric pressure, has been studied by measuring initial permeability as a function of temperature for samples subject to fixed pressures up to 50 kbar. A transition to antiferromagnetic ordering, which probably results from pressure broadening of the Mn d-bands, appears to occur between 25 and 35 kbar.

IV. PHYSICS OF SOLIDS

During this past year, several new exploratory programs have been initiated: secondary electron emission, phosphor upconversion and metal-insulator transitions.

The secondary electron emission program is aimed at finding and understanding materials with high secondary yields at low primary electron energies. One of the systems under investigation, NiO:Li⁺, appears quite promising in this respect.

Two phosphor upconversion studies are under way – one concerned with the efficient conversion of laser infrared radiation ($\sim 1\mu\text{m}$) to the visible using rare-earth ions, and the other with optimization of the infrared stimulability of visible luminescence in ZnS. In the former program, erbium and ytterbium are being placed in hosts having the garnet structure; initial results, without any optimization, indicate an efficiency comparable with that of YF₃:Yb,Er, which is the most efficient infrared-to-green upconverter listed in the literature. In the latter program, several experiments have been performed on the transient as well as steady state infrared stimulation effect in ZnS:Cu,Al under conditions of steady ultraviolet pumping. A model has been set up and the response of the system has been formulated in terms of coupled rate equations. Computer solutions are presently being carried out. In a second phase of this research, other phosphors also are being prepared and tested for infrared stimulability.

In the metal-insulator transition program, films of V₂O₃ and Ti₃O₅ have been made and are being characterized by optical and electrical measurements. A theoretical model of electronic switching near the metal-insulator transition has been formulated and is now under investigation.

High resolution spectroscopic studies in CO and NO have continued, using current-tuned CW diode lasers. In CO, our previous measurements of the fundamental vibration-rotation absorption band taken at low gas pressures (< 1 torr), with a PbS_{0.82}Se_{0.18} laser, have been extended to high pressures (< 200 torr); the self-induced pressure shift in the center and the broadening of the P(9) absorption line at $4.745\mu\text{m}$ have been obtained for the first time. In NO, a 5.255- μm PbS_{0.62}Se_{0.38} laser was used for taking quantitative measurements of the Zeeman splitting and Lambda doubling of the R(15/2)_{1/2, 3/2} absorption lines and of the magnetic rotation spectrum of the R(15/2)_{1/2} absorption line.

In an effort to understand the temperature dependence of light scattering from antiferromagnets, the effect of including additional graphical perturbation theory diagrams on

the intensity of two-magnon Raman scattering have been examined. While neglect of these extra diagrams leads to vanishing intensity at T_N , their inclusion gives a finite value, as observed experimentally. The calculations of parallel susceptibility, perpendicular susceptibility and staggered parallel susceptibility using graphical perturbation theory have also been formulated.

For the first time, far-infrared H_2O and HCN lasers have been used to carry out precise cyclotron resonance experiments in thin epitaxial films of $Ge_{1-x}In_xAs$ alloys, in the range $0 < x < 0.105$. Although existing theories predict a nonlinear dependence of the effective mass with concentration, an almost linear variation is observed.

Study continues on the band structure of $Pb_{1-x}Sn_xSe$ alloys, for compositions $x = 0.17$ and 0.20 (i.e., near zero gap) and carrier concentrations from 2×10^{17} to $2 \times 10^{18} \text{ cm}^{-3}$. Surprisingly, the value of pressure at the resistivity minimum, which is expected to occur when the energy gap goes through zero, has been found to depend on carrier concentration and also carrier type.

V. MICROELECTRONICS

Beam-leaded substrates employing polyimide-coated copper with multilevel aluminum interconnections have been fabricated successfully and their bonding characteristics are being evaluated.

The particle detector arrays, which require double-sided wafer processing, are being tested to determine their characteristics in beta particle bombardment. The results of these tests will determine the action taken in the next phase of the program.

Several other silicon devices or integrated circuits have reached a satisfactory level of performance and are described in Sec. V B, Semiconductor Program.

The yield of masks has been improved by a concentrated effort to trace the source of mask defects. Further improvements are expected when the mask-making area is modified to reduce particle contamination.

Packaging of devices for high power applications is continuing and improvements in thermal resistance characteristics of the E-Bird and TRAPATT devices have been significant.

Prototype hybrid limiter circuits for the LES system have been fabricated and electrical tests indicate satisfactory performance has been achieved. Several more units will be fabricated for system and environmental tests before the production units are undertaken.

The dynamic testing characteristics of the laser scanning system for integrated circuits have been explored by adding a second laser beam to change the logic states of the integrated circuit and to permit greater electrical evaluation without the usual mechanical probes. The system is particularly useful for diagnostic evaluation of the internal features of the monolithic structure.

REPORTS ON SOLID STATE RESEARCH

15 August through 15 November 1971

PUBLISHED REPORTS

Journal Articles*

JA No.

3791	Theory of Electron-Surface-Plasmons Interactions in Tunneling, Low-Energy-Electron Diffraction, and Photoemission	K. L. Ngai E. N. Economou [†]	Phys. Rev. B <u>4</u> , 2132 (1971)
3806	Temporal and Spatial Gain in Stimulated Light Scattering	N. M. Kroll [†] P. L. Kelley	Phys. Rev. A <u>4</u> , 763 (1971)
3818	A High Temperature Study of Native Defects in ZnTe	F. T. J. Smith	J. Phys. Chem. Solids <u>32</u> , 2201 (1971)
3838	Far-Infrared Mixing in High-Purity GaAs	B. Y. Lao M. M. Litvak	J. Appl. Phys. <u>42</u> , 3357 (1971)
3840	Anomalous Properties of the Vanadium Oxides	J. B. Goodenough	<u>Annual Review of Materials Science</u> , Vol. 1, R. A. Huggins, Ed. (Annual Reviews Inc., Palo Alto, California, 1971), p. 101
3867	Spin-Wave Approach to Two-Magnon Raman Scattering in a Simple Antiferromagnet	R. W. Davies S. R. Chinn H. J. Zeiger	Phys. Rev. B <u>4</u> , 992 (1971)
3868	The Two Components of the Crystallographic Transition in VO_2	J. B. Goodenough	J. Solid State Chem. <u>3</u> , 490 (1971)
3890	Infrared Spectroscopy of CO Using a Tunable PbSSe Diode Laser	K. W. Nill F. A. Blum A. R. Calawa T. C. Harman	Appl. Phys. Letters <u>19</u> , 79 (1971)
3915	The Tetragonal High-Pressure Form of TaOPO_4	J. M. Longo [†] J. W. Pierce J. A. Kafalas	Mater. Res. Bull. <u>6</u> , 1157 (1971)
3916	"Mass Anomaly" in the Zeeman Effect of GaAs Donor 2p Levels	G. E. Stillman D. M. Larsen C. M. Wolfe	Phys. Rev. Letters <u>27</u> , 989 (1971)
3928	Coexistence of Localized and Itinerant d Electrons	J. B. Goodenough	Mater. Res. Bull. <u>6</u> , 967 (1971)

* Reprints available.

[†] Author not at Lincoln Laboratory.

Meeting Speeches

MS No.

2754	Narrow-Gap Semiconductor Lasers	T. C. Harman	<u>The Physics of Semimetals and Narrow-Gap Semiconductors</u> , D. L. Carter and R. T. Bate, Eds. (Pergamon, New York, 1971), p. 363 [J. Phys. Chem. Solids <u>32</u> , Suppl. 1 (1971)]
2756	Shubnikov-de Haas Measurements in $Pb_{1-x}Sn_xTe$ Under Hydrostatic Pressure	J. Melngailis J. A. Kafalas T. C. Harman	<u>The Physics of Semimetals and Narrow-Gap Semiconductors</u> , D. L. Carter and R. T. Bate, Eds. (Pergamon, New York, 1971), p. 407 [J. Phys. Chem. Solids <u>32</u> , Suppl. 1 (1971)]
2757	Metal-Semiconductor Contacts on $Pb_{1-x}Sn_xTe$	K. W. Nill J. N. Walpole* A. R. Calawa T. C. Harman	<u>The Physics of Semimetals and Narrow-Gap Semiconductors</u> , D. L. Carter and R. T. Bate, Eds. (Pergamon, New York, 1971), p. 383 [J. Phys. Chem. Solids <u>32</u> , Suppl. 1 (1971)]
2763	Recent Experiments on Zero Gap Semiconductors	S. H. Groves	<u>The Physics of Semimetals and Narrow-Gap Semiconductors</u> , D. L. Carter and R. T. Bate, Eds. (Pergamon, New York, 1971), p. 447 [J. Phys. Chem. Solids <u>32</u> , Suppl. 1 (1971)]
2765	Electronic Properties of the Group V Semimetals	M. S. Dresselhaus	<u>The Physics of Semimetals and Narrow-Gap Semiconductors</u> , D. L. Carter and R. T. Bate, Eds. (Pergamon, New York, 1971), p. 3 [J. Phys. Chem. Solids <u>32</u> , Suppl. 1 (1971)]
2770	$k \cdot p$ Theory for the Conduction and Valence Bands of $Pb_{1-x}Sn_xTe$ and $Pb_{1-x}Sn_xSe$ Alloys	J. O. Dimmock	<u>The Physics of Semimetals and Narrow-Gap Semiconductors</u> , D. L. Carter and R. T. Bate, Eds. (Pergamon, New York, 1971), p. 319 [J. Phys. Chem. Solids <u>32</u> , Suppl. 1 (1971)]
2780	Raman Scattering from $Hg_{1-x}Cd_xTe$	A. Mooradian T. C. Harman	<u>The Physics of Semimetals and Narrow-Gap Semiconductors</u> , D. L. Carter and R. T. Bate, Eds. (Pergamon, New York, 1971), p. 297 [J. Phys. Chem. Solids <u>32</u> , Suppl. 1 (1971)]
2845	High-Resolution Magnetospectroscopy of Graphite	P. R. Schroeder* M. S. Dresselhaus A. Javan*	<u>The Physics of Semimetals and Narrow-Gap Semiconductors</u> , D. L. Carter and R. T. Bate, Eds. (Pergamon, New York, 1971), p. 139 [J. Phys. Chem. Solids <u>32</u> , Suppl. 1 (1971)]

* Author not at Lincoln Laboratory.

MS No.

3141	Metallurgical and Electronic Properties of CdTe Related to Preparation of Single Crystals	A. J. Strauss	<u>Proceedings of the International Symposium on Cadmium Telluride</u> , Strasbourg, France, 29-30 June 1971, P. Siffert and A. Cornet, Eds. (Centre de Recherches Nucléaires, Strasbourg, 1971), p.1-1
* * * *			

UNPUBLISHED REPORTS

Journal ArticlesJA No.

3775	Partial Pressures in the Cd-Te and Zn-Te Systems	R. F. Brebrick	Accepted by J. Electrochem. Soc.
3894	High Apparent Mobility in Inhomogeneous Semiconductors	C. M. Wolfe G. E. Stillman J. A. Rossi	Accepted by J. Electrochem. Soc
3898	Persistent Photo-Dielectric Lens Effect in Cadmium Sulfide	K. B. Kanarek* C. D. Wyche A. S. Pine	Accepted by J. Appl. Phys.
3899	Exciton Bands in Antiferromagnetic Cr ₂ O ₃	R. M. Macfarlane* J. W. Allen	Accepted by Phys. Rev.
3913A	Precision Verification of Effective Mass Theory for Shallow Donors in GaAs	G. E. Stillman D. M. Larsen C. M. Wolfe R. C. Brandt*	Accepted by Solid State Commun.
3918	Capacitance-Voltage Characteristics of Metal Barriers on p-PbTe and n-InAs: Effects of the Inversion Layer	J. N. Walpole* K. W. NiII	Accepted by J. Appl. Phys.
3920	EuTe II: Resistivity and Hall Effect	Y. Shapira* S. Foner* N. F. Oliveira, Jr.* T. B. Reed	Accepted by Phys. Rev.
3921	EuTe III: Ultrasonic Behavior	Y. Shapira* T. B. Reed	Accepted by Phys. Rev.
3937	Fourier Expansion for Electronic Bands in Trigonal Tellurium and Selenium	G. Dresselhaus	Accepted by Phys. Rev. B.

* Author not at Lincoln Laboratory.

Reports

<u>JA No.</u>			
3940	Raman Scattering from Europium Chalcogenides	R. K. Ray* J. C. Tsang* M. S. Dresselhaus R. L. Aggarwal* T. B. Reed	Accepted by Phys. Letters A
3946	Aluminum Interconnections and Beam Leads on Polyimide-Coated, Copper Substrates	F. J. Bachner	Accepted by IEEE Transactions on Parts, Hybrids, and Packaging
3949	Pb _{1-x} Sn _x Te Photovoltaic Diodes and Diode Lasers Produced by Proton Bombardment	J. P. Donnelly A. R. Calawa T. C. Harman A. G. Foyt W. T. Lindley	Accepted by Solid State Electron.
3951	Carrier Freeze-out and Acceptor Energies in p-Type Hg _{1-x} Cd _x Te	C. T. Elliott* I. Melngailis T. C. Harman A. G. Foyt	Accepted by J. Phys. Chem. Solids
3953	Measurements of the Lattice Parameter of Wüstite at High Temperature	M. Hayakawa* J. B. Cohen* T. B. Reed	Accepted by J. Am. Ceram. Soc.
<u>MS No.</u>			
2727	Theory of Antiferromagnetism and Ferrimagnetism	J. B. Goodenough	Accepted as chapter in <u>Physics of Electronic Ceramics</u> (Marcel Dekker, Inc., New York)
2993	Application of Heat Pipe Technology to Crystal Growth	J. Steininger T. B. Reed	Accepted by J. Crystal Growth
3018A	Phase Diagrams and Crystal Growth of Pseudobinary Alloy Semiconductors	J. Steininger A. J. Strauss	Accepted by J. Crystal Growth
3146	Infrared Detectors and Applications	J. O. Dimmock	Accepted by J. Electronic Materials
3153	Preparation and Properties of Pb _{1-x} Cd _x S	A. R. Calawa J. A. Mroczkowski T. C. Harman	Accepted by J. Electronic Materials
3155	The Use of Lasers in Pollution Monitoring	I. Melngailis	Accepted by IEEE Trans. Geosci. Electron.

* Author not at Lincoln Laboratory.

Meeting Speeches*MS No.

2917A	High Purity GaAs	C. M. Wolfe G. E. Stillman	Materials Science Seminar, University of Southern California, Los Angeles, 12 November 1971
2951B	Localized and Itinerant d Electrons in Transition- Metal Compounds	J. B. Goodenough	Chemistry Department Seminar, Brookhaven National Laboratory, Upton, New York, 30 September 1971
2951C, E	Itinerant vs Localized Electrons	J. B. Goodenough	Solid-State Student Seminar, M. I. T., 1 November 1971; Department of Physics & Astronomy Seminar, Uni- versity of Florida, 11 November 1971
3090	Influence of Madelung Energy and Covalency on Structure of $A^+B^{5+}O_3$ Compounds	J. A. Kafalas	Fifth Materials Research Symposium on Solid State Chemistry, Gaithers- burg, Maryland, 18-21 October 1971
3120	Preparation and Structure of a Pyrochlore and Perovskite in the $BiRhO_{3+x}$ System	J. M. Longo [†] P. M. Raccah J. A. Kafalas J. W. Pierce	
3110A	Raman Spectroscopy of Solids	A. Mooradian	Esfahan Symposium on Fundamental and Applied Laser Physics, Univer- sity of Esfahan, Iran, 29 August – 5 September 1971
3138B	Tunable Infrared Lasers and Their Applications	P. L. Kelley	
3110C	Raman Spectroscopy of Solids	A. Mooradian	Tenth National Meeting of Society for Applied Spectroscopy, St. Louis, 18-22 October 1971
3138	Tunable Infrared Lasers and Their Applications	P. L. Kelley	
3110D	Raman Spectroscopy of Solids	A. Mooradian	Seminar, University of Toronto, Ontario, Canada, 7 October 1971
3134A, B	Infrared Photodiodes Fabri- cated by Proton Bombardment	J. O. Dimmock A. G. Foyt J. P. Donnelly T. C. Harman W. T. Lindley	Seminar, Navy Electronics Labora- tory Center, San Diego, 23 August 1971; Seminar, Hughes Aircraft, Malibu, 2 September 1971
3144	Materials and Processing Techniques for the Fabri- cation of High Quality Millimeter Wave Diodes	B. J. Clifton W. T. Lindley R. W. Chick R. A. Cohen	Conference on High Frequency Generation and Amplification: Devices and Applications, Cornell University, 17-19 August 1971
3148	Tunable $PbS_{1-x}Se_x$ Diode Lasers in the $5\mu m$ Region	K. W. Nill F. A. Blum A. R. Calawa T. C. Harman	Device Research Conference, University of Michigan, 28 June – 1 July 1971

* Titles of Meeting Speeches are listed for information only. No copies are available for distribution.

[†] Author not at Lincoln Laboratory.

MS No.

3146	Infrared Detectors and Applications	J. O. Dimmock	Thirteenth Annual Conference of the Electronic Materials Committee of the Metallurgical Society of AIME, San Francisco, 29 August – 1 September 1971
3153	Preparation and Properties of $Pb_{1-x}Cd_xS$	A. R. Calawa J. A. Mroczkowski T. C. Harman	
3146A, B	Infrared Detectors and Applications	J. O. Dimmock	Seminar, Night Vision Laboratory, Ft. Belvoir, Virginia, 20 October 1971; Alloy Physics-Solid State Physics Colloquium, National Bureau of Standards, Gaithersburg, Maryland, 21 October 1971
3152A	Acoustical and Optical Activity in Crystals	A. S. Pine	Seminar, Purdue University, 5 November 1971
3155	The Use of Lasers in Pollution Monitoring	I. Melngailis	International Geoscience Electronics Symposium, Washington, D.C., 25-27 August 1971
3157	Single Particle Transmission in the Trigonal Faraday Geometry in Bismuth	R. A. Murphy A. L. McWhorter	U. S.-Japanese Seminar, Cornell University, 8 September 1971
3160	Optical de Haas-Shubnikov Effect	M. S. Dresselhaus	
3175	Various Aspects of Magnetic Semiconductors	J. B. Goodenough	Europhysics Conference on "Metal Insulator Transition and the Development of Narrow Energy Bands," Aussois, France, 6-11 September 1971
3192	Tunable Infrared Lasers and Their Applications	P. L. Kelley E. D. Hinkley A. Mooradian	NEREM, Boston, 3-5 November 1971

ORGANIZATION

SOLID STATE DIVISION

A. L. McWhorter, *Head*
P. E. Tannenwald, *Associate Head*
C. R. Grant, *Assistant*

QUANTUM ELECTRONICS

A. Mooradian, *Leader*
P. L. Kelley, *Associate Leader*
Bmeck, S. R. J. Johnson, E. J.
Burke, J. W. Moulton, P. F.*
Chinn, S. R. Pine, A. S.
Eng, R. S. Rossi, J. A.
Hancock, R. C.

ELECTRONIC MATERIALS

J. B. Goodenough, *Leader*
A. J. Strauss, *Associate Leader*

Anderson, C. H., Jr. LaFleur, W. J.
Batson, D. A. Lavine, M. C.†
Button, M. J. Mastromattei, E. I.
Coppola, A. J. Mikkelsen, J. C., Jr.
Delaney, E. J. Mroczkowski, I. H.
Fahey, R. E. Owens, E. B.
Finn, M. C. Pantano, J. W.
Hong, H. Y-P Pierce, J. W.
Hsieh, J. J. Plonko, M. G.
Iseler, G. W. Reed, T. B.
Kafalas, J. A. Tracy, D. M.

MICROELECTRONICS

R. E. McMahon, *Leader*

Bachner, F. J. Gray, R. V.
Beatrice, P. A. McGonagle, W. H.
Clough, T. F. Mountain, R. W.
Cohen, R. A. Pichler, H. H.
Davis, C.† Pybus, V. J.
Durant, G. L. Smythe, D. L.
Grant, L. L. Wilde, R. E.

SOLID STATE PHYSICS

J. G. Mavroides, *Co-Leader*
H. J. Zeiger, *Co-Leader*
G. B. Wright, *Assistant Leader (LOA)*
Allen, J. W. Henrich, V. E.
Barch, W. E. Johnson, L.*
Blum, F. A., Jr. Kernan, W. C.
Brodersen, R. W.* Kolesar, D. F.
Davies, R. W. Korn, D. M.
Defeo, W. E. Larsen, D. M.
Dresselhaus, G. F. Melngailis, J.
Dresselhaus, M. S.† Menyuk, N.
Dwight, K., Jr. Nill, K. W.
Feldman, B. Parker, C. D.
Fetterman, H. Seccombe, D.*
Groves, S. H.

APPLIED PHYSICS

J. O. Dimmock, *Leader*
T. C. Harman, *Assistant Leader*
I. Melngailis, *Assistant Leader*
Belanger, L. J. McBride, W. F.
Calawa, A. R. Murphy, R. A.
Carter, F. B. Orphanos, W. G.
DeMeo, N. Paladino, A. E.
Donnelly, J. P. Ralston, R. W.
Ferrante, G. A. Spears, D. L.
Foyt, A. G. Stillman, G. E.
Hurwitz, C. E. Ward, J. H. R., III
Krohn, L., Jr. Wolfe, C. M.
Lincoln, G. A. Youtz, P.
Lindley, W. T.

MICROSOUND

E. Stern, *Leader*
Alusow, J. A. Chen, F.
Brogan, W. T. Smith, H. I.
Burke, B. E. Williamson, R.

* Research Assistant

† Part Time

I. SOLID STATE DEVICE RESEARCH

A. p-n JUNCTION PHOTODIODES IN PbTe PREPARED BY Sb⁺ ION IMPLANTATION

Sb⁺ ion implantation has been used to convert layers of p-type PbTe into n-type material and to fabricate high quality p-n junction photodiodes. The p-type PbTe crystals used in these experiments were grown by a new slush-recrystallization technique¹ and subsequently annealed. At 77°K, the p-type carrier concentration was approximately $1 \times 10^{18}/\text{cm}^3$. After standard polishing and etching, the samples were coated with a thick layer of photoresist and an array of 15-mil squares on 20-mil centers opened in this photoresist. This photoresist is sufficiently thick to completely stop the Sb⁺ ions in the subsequent ion implantation step and therefore acts as a suitable ion implantation mask. The Sb ion implantation was carried out with the PbTe samples at room temperature using 400-keV Sb⁺ ions. A total ion fluence of 1 to $2 \times 10^{14}/\text{cm}^2$ was used in these experiments. Following implantation, the photoresist implantation mask was removed and the samples were coated with 1500 Å of pyrolytic SiO₂ at 340°K. This SiO₂ deposition step took 5 minutes and also acted to effectively anneal out the radiation damage caused by the room temperature Sb⁺ ion implantation. Following this process, holes were opened in the oxide and gold contacts electroplated on the sample.

With the sample at 77°K, Hall effect measurements of the van der Pauw² type, thermoelectric probe measurements and current-voltage measurements all showed that the Sb implanted areas were converted to n-type, while unimplanted portions of the crystal remained p-type. The van der Pauw² measurements gave an n-type sheet carrier concentration in the Sb implanted region of about $10^{14}/\text{cm}^2$, indicating a high doping efficiency. Assuming a junction depth of between 0.1 to 0.2 μm, which is approximately that predicted by Lindhard, Scharff and Schiott range theory,³ an effective average carrier concentration is obtained in the implanted layer of between 5×10^{18} and $10^{19}/\text{cm}^3$.

The 15-mil-square photodiodes prepared by this technique have exhibited zero-bias resistances as high as 15 megohms for a resistance area product of $2.1 \times 10^4 \text{ ohm}\cdot\text{cm}^2$ at 77°K. The capacitance of these devices was approximately 4500 pF, giving a zero-bias RC time constant of 67 msec. Preliminary photometric measurements have shown that at 77°K these diodes have a peak responsivity at a wavelength of 4.4 μm, where the peak quantum efficiency is 40 percent. The cutoff wavelength (responsivity 50 percent of peak) was at about 5.1 μm. The measured peak detectivity in reduced background was $1.5 \times 10^{12} \text{ cm} \sqrt{\text{Hz}}/\text{W}$, which is half of the calculated Johnson noise limited detectivity of $3 \times 10^{12} \text{ cm} \sqrt{\text{Hz}}/\text{W}$. A large portion of this difference appears to be due to amplifier noise.

J. P. Donnelly T. C. Harman
A. G. Foyt W. T. Lindley

B. ELECTRICAL CHARACTERISTICS OF GUARDED n-p InSb PHOTODIODES FABRICATED BY PROTON BOMBARDMENT

The surface properties and current-voltage characteristics of planar n-p InSb photodiodes fabricated by proton bombardment have been investigated in diode structures with annular guard rings formed by peripheral field plates. The potential of the guard ring, or field plate, can be

Section I

varied independently of the diode bias to regulate the surface potential around the diode, thereby compensating for the built-in surface charge. Diode arrays were made on p-type substrates of concentration $2 \times 10^{14} \text{ cm}^{-3}$ and $4 \times 10^{15} \text{ cm}^{-3}$. The n-type regions were created by proton bombardment.⁴ MOS capacitance-voltage measurements of the guard rings, as well as capacitance-voltage and current-voltage measurements of the diodes were performed to characterize the surface states of the structures and to determine the diode current flow mechanisms. It was found that variation of a few volts in field plate voltage could significantly alter the diode characteristic, and that the fabrication processes produced flat-band surface charge densities of $\sim 4 \times 10^{11} \text{ cm}^{-2}$. The reverse current at low bias was found to scale with the diode area and appears to be due to carrier generation in the diode depletion layer. At higher bias, the reverse current scaled with diode perimeter and is believed to be due to tunneling phenomena. The reverse bias leakage currents of these devices are very small at the optimum field plate voltage. At a reverse bias voltage of 1.0 V, leakage currents as small as 11 nA for a 13-mil-diameter device and 31 nA for a 20-mil-diameter device have been measured.

1. Diode Fabrication

Figure I-1 is a cross section of a typical diode. Prior to bombardment, each substrate was etched for 3 sec in 2:1:1 HNO₃:HF:HAc, then coated with a 900-Å layer of pyrolytic SiON. This SiON layer was formed by the reaction of silane, oxygen and ammonia in a nitrogen-rich atmosphere at 210 °C. Some wafers were then annealed in hydrogen at 300 °C or 350 °C for one hour.

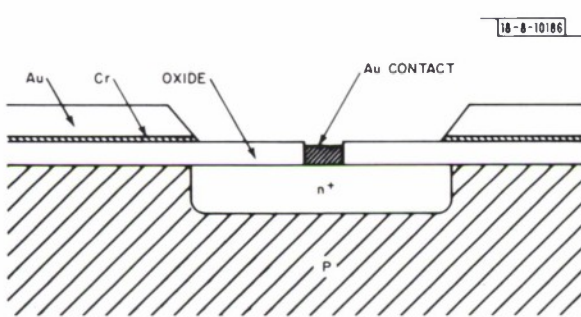


Fig. I-1. Cross section of a guarded diode. The n⁺ region is approximately 1 μm deep; the oxide, 0.14 μm thick; the Cr-Au layer is 0.9 μm thick. The Au contact is about 0.1 μm thick. The graded field plate is due to the etching process.

Each sample was then given a 500-Å overcoat of PSK-3 glass by sputtering in an oxygen and argon plasma. Next, a thin layer of chromium was sputtered to form a strong bond with the oxide, then a 9000-Å layer of gold was sputtered over the chromium. The wafer was patterned and etched, leaving annular rings in the Cr-Au layer. These annular rings serve as a bombardment mask to define the p-n junction and also as a field plate for the diode. The taper at the edge of the ring, which results from the etching process, insures that the edge of the field plate will overlap the edge of the p-n junction. After the etching of the bombardment

mask, the wafer was again coated with photoresist and 5-mil holes were opened in the oxide. A thin gold layer (500 to 1000 Å) was electroplated in the holes to serve as a contact to the n-type layer. The wafer was then bombarded with a 0.075- $\mu\text{A}/\text{cm}^2$, 140-kV proton beam for 5 minutes. The beam penetrated the thin gold contact and the oxide, creating approximately 1- μm -deep n-type regions of 10^{17} cm^{-3} concentration in the crystal. The diode contacts were then further plated and a contact was electroplated to the back of the substrate. The wafer was then mounted on a TO8 header and placed in a vacuum dewar, which allowed the sample to be cooled to 77 °K in the dark. All measurements in this work were made with the diode in the dark, so that carrier generation due to ambient radiation incident on the wafer would be eliminated.

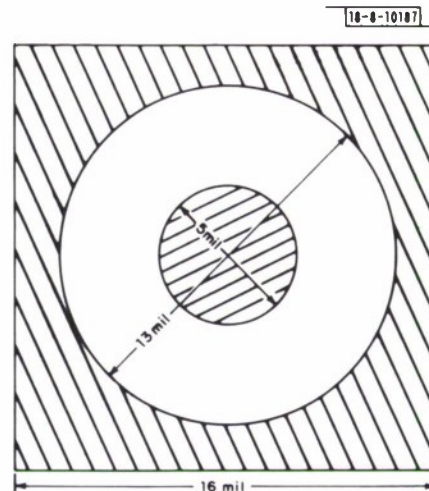


Fig. I-2. Tap view of guarded diode pattern. The pattern is repeated on 20-mil centers. Wafers with this array pattern are numbered with a "p" prefix in the data.

The diodes were fabricated in two array patterns. The first pattern, shown in Fig. I-2, consists of a 13-mil-diameter diode inside a 16-mil square. The diode contact is 5 mils in diameter and the pattern is repeated on 20-mil centers. These diode arrays are numbered with a "p" prefix in the data and were used to acquire most of the data.

The second pattern is shown in Fig. I-3. It consists of six diodes of various diameters: two 8-mil and one each of size 10, 20, 40 and 80 mils. The diodes have 5-mil-diameter contacts and annular guard rings 5 mils wide; this pattern is repeated on 130-mil centers. These arrays are numbered with an "A" prefix in the data and were used to examine the effects of diode size on the I-V characteristics.

2. MOS Measurements

Capacitance-voltage measurements were made on the MOS structure formed by the p-type substrate, oxide and metal field plate. From these measurements, various surface properties were determined.

Using the method of Grove, *et al.*,⁵ the flat band surface charge density was calculated. It was assumed that the experimental C-V curves corresponded to an ideal MOS structure, augmented by surface charge Q_{SS} at the oxide-semiconductor interface and a work function difference $\Delta\varphi_m$ between the InSb and the Cr, so that the applied voltage $V' = \Delta\varphi_m + (Q_{SS}/C_o) + V$, where C_o is the oxide capacitance and V is the voltage across an ideal MOS structure.

Having determined the oxide dielectric constant ϵ_o from the MOS capacitance for a strongly accumulated surface, the ideal MOS flat band (i.e., zero applied bias) capacitance was calculated from⁶

$$C_{fb} = \frac{\epsilon_o A}{d + \frac{\epsilon_o}{\epsilon_s} \frac{L_D}{\sqrt{2}}} ,$$

Section I

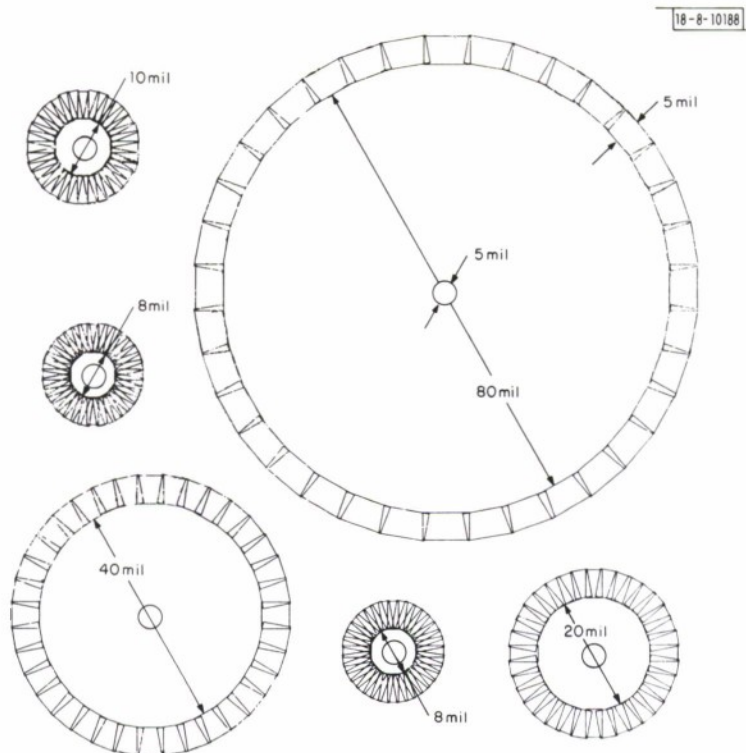


Fig. I-3. Tap view of the six-diameter diode pattern. All diode contacts are 5 mils in diameter, and all field plates are 5 mils wide. The pattern is repeated an 130-mil centers. Wafers with this array pattern are numbered with an "A" prefix in the data.

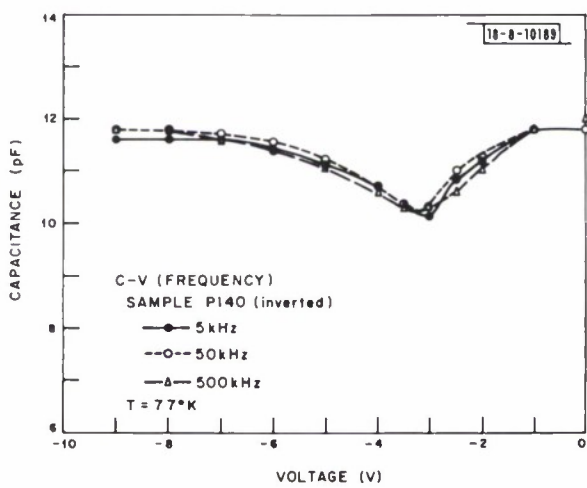


Fig. I-4. MOS capacitance-voltage curve for P140 ($4 \times 10^{15} \text{ cm}^{-3}$ substrate, 3500 Å SiON oxide). Measurements were taken at 5, 50 and 500 kHz. Flat-band calculations indicate an inverted surface with a negative surface charge density of $5.4 \times 10^{11} \text{ cm}^{-2}$.

where $\epsilon_s = 17.5$ is the InSb dielectric constant, d is the oxide thickness, A is the area of the MOS structure and L_D is the extrinsic Debye length. [Here, $L_D = (2kT/P_{\rho_0}q^2)^{1/2}$, where q is the electronic charge, k is the Boltzmann constant, T is temperature in degrees Kelvin and P_{ρ_0} is the carrier concentration of the substrate.]

The voltage difference ΔV between zero bias and the voltage at which this flat-band capacitance occurred was then used to calculate the surface charge density N_{SS} . This voltage difference was usually large compared to the work function difference $\Delta\varphi_m$ of 0.15 V. For P140, as shown in Fig. 1-4, $\Delta V = -5.9$ V, indicating a positively charged surface state density $N_{SS} = 5.4 \times 10^{11} \text{ cm}^{-2}$ (surface inverted).

For wafers without a hydrogen anneal, the average charged surface state density was $4 \times 10^{11} \text{ cm}^{-2}$ and most surfaces were inverted, although two samples had non-inverted surfaces. For several wafers annealed in hydrogen at 300°C, the samples also had inverted surfaces and a charged surface state density of $4 \times 10^{11} \text{ cm}^{-2}$. However, one wafer annealed in hydrogen at 350°C had a non-inverted surface and a negatively charged surface state density of $4 \times 10^{10} \text{ cm}^{-2}$.

These C-V measurements were made in the range 5 to 500 kHz. For a field plate voltage corresponding to a depleted surface, the measured capacitance decreased with increasing frequency. This observed drop in capacitance suggests the presence of surface states which cannot respond to the voltage oscillations at high frequency, and therefore no longer contribute to the device capacitance. If these states are modeled according to Terman,⁷ their time constants are estimated to be on the order of 2×10^{-6} sec.

For samples annealed in hydrogen, the C-V curves exhibited deeper minima than those observed in non-hydrogen annealed samples. This suggests that the hydrogen anneal reduced the interface charge density, creating a relatively deeper depletion layer in the semiconductor for a given frequency and bias. Similar charge reduction has been observed in hydrogen annealing experiments in silicon.⁸

It should be noted that no hysteresis in the C-V characteristics was observed in these measurements. This suggests that SiON is not characterized by slow trapping states, such as those found in anodized InSb oxides.⁹

Finally, from the C-V measurements, the average dielectric constant for the composite layer at 900 Å of SiON and 500 Å of PSK-3 glass is 4.6. This value appears to be independent of the hydrogen anneal.

3. Diode C-V Measurements

Differential capacitance measurements of diodes were made with field plate voltages set for an optimal I-V characteristic, as defined by a minimum current at a particular reverse bias. These measurements permit a concentration profile to be determined for a one-sided junction¹⁰

$$N(x) = \frac{C^3}{A^2 \epsilon_s q \left(-\frac{dC}{dV} \right)}$$

From these measurements, there was no apparent grading in the concentration of the p-region beneath the junction and the one-sided abrupt junction model was substantiated. Moreover, it was found that the hydrogen anneals did not alter the carrier concentrations in wafers with good diodes on 10^{14} cm^{-3} material. However, as discussed below, diodes made on several of the

Section I

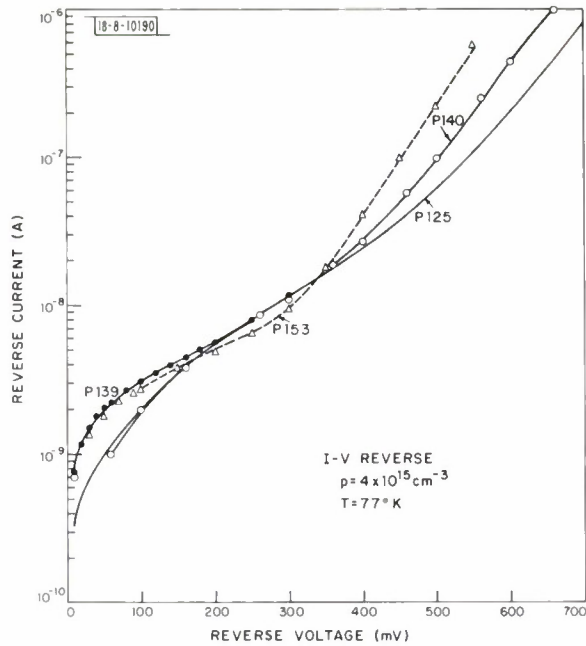
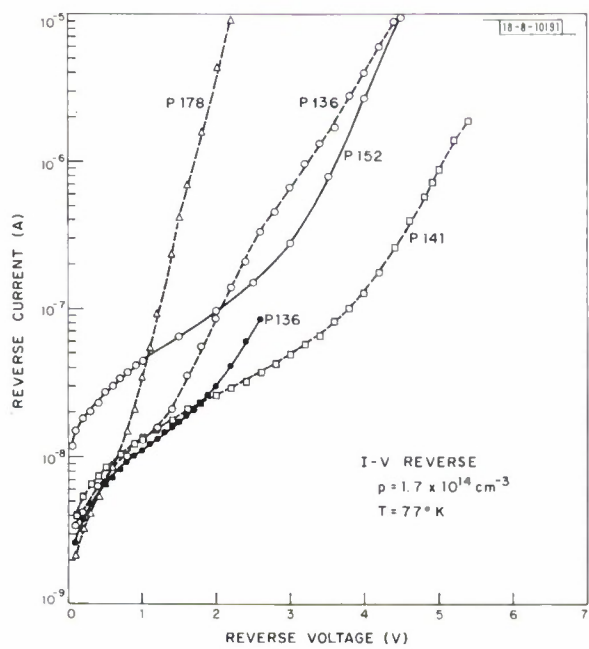


Fig. I-6. Reverse I-V characteristics for all wafers with $2 \times 10^{14} \text{ cm}^{-3}$ substrate concentrations fabricated in the 16-mil-square pattern. Variations in oxide thickness and use of a H_2 anneal had little effect on reverse current below 0.7 V. However, significant variation in breakdown is evident. Characteristics were determined at an optimum field plate voltage for each wafer.



hydrogen annealed wafers exhibited anomalously low breakdown voltages. C-V measurements on these diodes indicated an increase in the carrier concentration to ~ 5 to $10 \times 10^{14} \text{ cm}^{-3}$ with little grading.

4. Diode I-V Measurements

Diode I-V measurements were made using two electrometers. For each diode, the field plate voltage was adjusted to yield minimum current at a particular reverse bias (usually 1 V for the lightly doped substrate and 0.1 V for the heavily doped substrate) which was chosen for each chip. It is interesting to note that this field plate voltage was quite close to the calculated flat-band potential for the 5-kHz MOS C-V curves.

Reverse characteristics for diodes on the 16-mil-square pattern are summarized in Figs. I-5 and I-6. The diodes fabricated on $4 \times 10^{15} \text{ cm}^{-3}$ substrates showed little variation due to surface treatment or oxide thickness and can be characterized by a 0.65-V breakdown (breakdown defined at a reverse current of $1 \mu\text{A}$). Changes of ± 0.5 V from optimal field voltage did not affect the reverse current at low bias, but did vary the breakdown voltage. However, diodes made on $2 \times 10^{14} \text{ cm}^{-3}$ substrates did show substantial variation in breakdown, ranging from 5.1 V for P141 with a 3500 Å oxide to 3.5 V for the standard 1400 Å – no hydrogen anneal – oxide to 1.7 V for the 1400 Å, 300°C hydrogen post-anneal oxide. At voltages below 0.7 V, the I-V characteristics of diodes on all the lightly doped wafers were similar. The reverse current below breakdown in these diodes was much more sensitive to field plate voltage than was the case for $4 \times 10^{15} \text{ cm}^{-3}$ material.

In forward bias, the voltage dependence of the current conformed to the $e^{qV/nkT}$ model,⁶ with average values of $n = 1.58$ for the $4 \times 10^{15} \text{ cm}^{-3}$ material and $n = 1.42$ for $2 \times 10^{14} \text{ cm}^{-3}$ material with no hydrogen anneal. For wafers annealed in hydrogen at 300°C, $n = 1.25$ and for those annealed at 350°C, $n = 1.29$. At present, it is not clear whether these variations in n values are due to shifts in the relative size of the diffusion currents with respect to recombination current,⁶ or to a variation in location in the energy gap of the trapping levels.¹¹

To better understand the current flow mechanisms, the I-V characteristics were studied as a function of diode size using the six-diameter diode pattern shown in Fig. I-3. The forward and reverse I-V characteristics for A-7, which had a 350°C hydrogen anneal, are shown in Figs. I-7 and I-8. The curves are for 10-, 20- and 40-mil-diameter diodes and were taken with a field plate voltage of 0.3 V, which corresponded to a minimum current at 1-V reverse bias. In forward bias, the diode current scales with diode area. In reverse bias, below 0.8 V, the current also scales with diode area; but at higher voltages, the current scales with perimeter, indicating an edge breakdown.

By plotting these reverse characteristics on log-log scales, as shown in Fig. I-9, it may be seen that the low bias current depends approximately on the square root of the voltage, suggesting that this current is due to generation in the space charge layer.¹² Similar log-log plots for all the other diode wafers on both heavily and lightly doped substrates exhibit this $V^{1/2}$ dependence at biases below 0.2 V in $4 \times 10^{15} \text{ cm}^{-3}$ material and 0.9 V in $2 \times 10^{14} \text{ cm}^{-3}$ material.

From this data, a minority carrier lifetime τ_o in the space charge layer may be estimated. Using the Sah, Noyce and Shockley theory¹¹ for carrier generation in the space charge layer of a reverse biased p-n junction, and assuming the capture cross section of electrons and holes

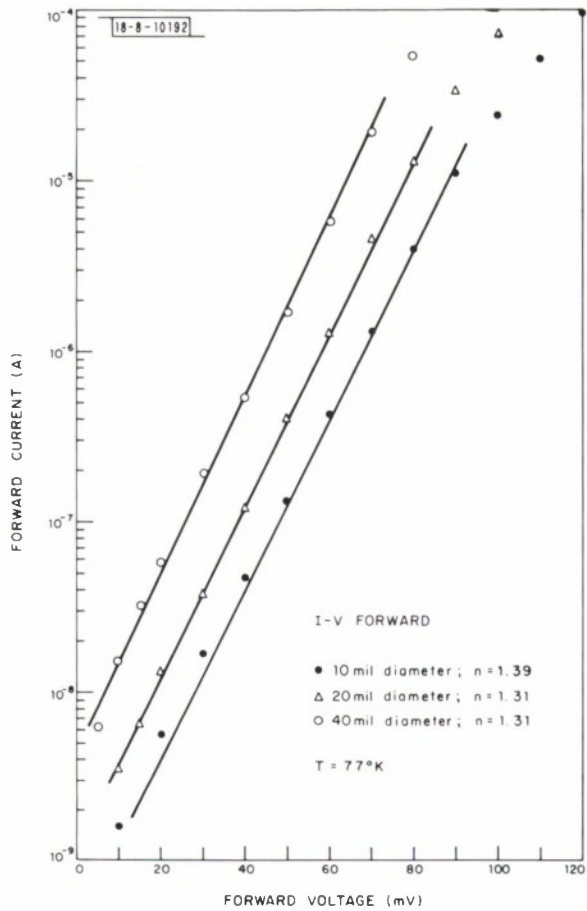


Fig. I-7. Forward I-V characteristics for a 10-, a 20- and a 40-mil-diameter diode on wafer A-7 ($2 \times 10^{14} \text{ cm}^{-3}$, 350°C H_2 past-anneal). The current scales with diode area and for all diodes measured on A-7 $n_{\text{ave}} = 1.29$. Field plate voltage was set for minimum current at 1.0-V reverse bias.

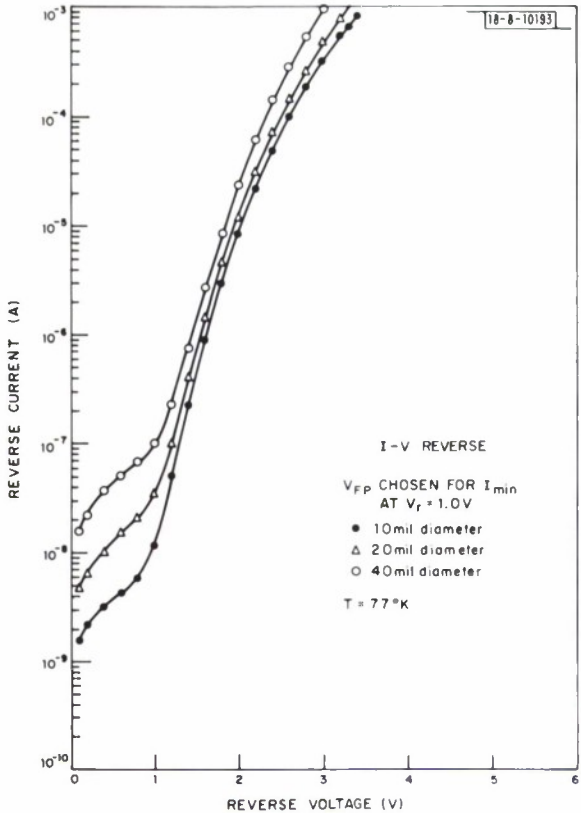


Fig. I-8. Reverse I-V characteristics for a 10-, a 20- and a 40-mil-diameter diode on wafer A-7 ($2 \times 10^{14} \text{ cm}^{-3}$, 350°C H_2 past-anneal). For voltage less than 0.8 V, current scales with diode area and tends toward a perimeter scaling above 1.5 V. Field plate voltage was set for minimum current at 1.0-V reverse bias.

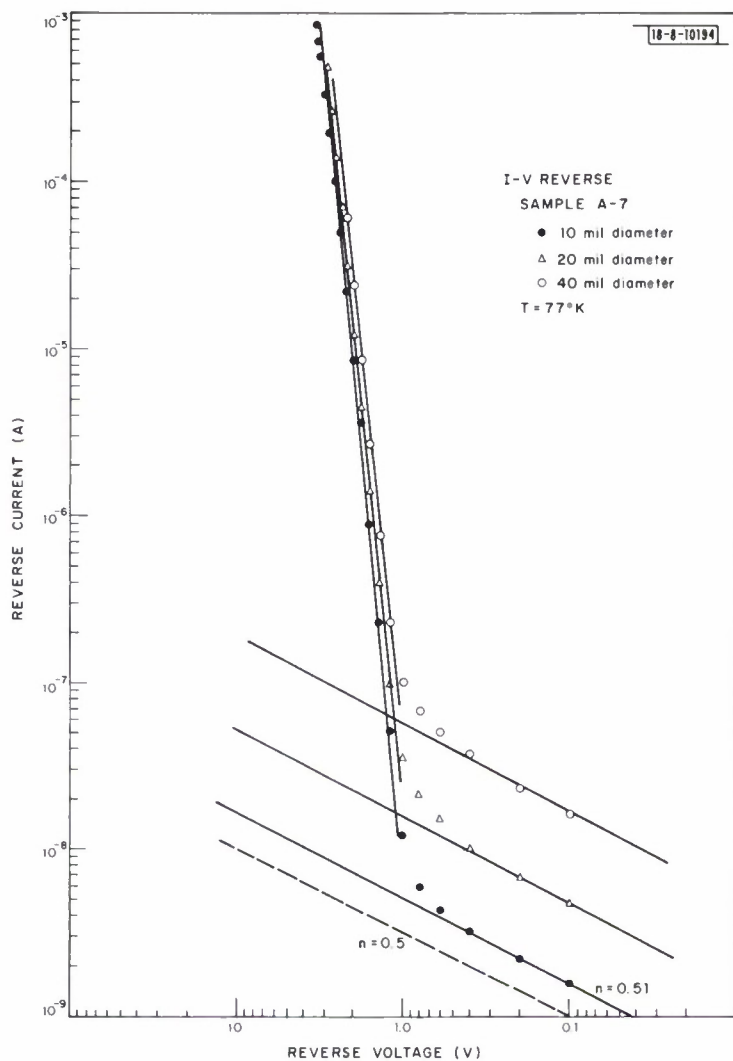


Fig. I-9. Data presented in Fig. I-8 plotted on log-log scales. Below 0.6 V, the reverse current follows $\propto V^{1/2}$ dependence, as indicated by the dotted line. Above 1.2 V, the current-voltage relations show a dependence characteristic of tunneling.

Section I

are equal, and that the energy of the trapping center is equal to the intrinsic Fermi level, the current will be given by

$$I = \frac{1}{2} \frac{qn_i}{\tau_o} WA_J$$

where W is the width of the space charge layer, A_J is the junction area, q is the electron charge and n_i is the intrinsic carrier concentration at 77°K ($2 \times 10^9 \text{ cm}^{-3}$). Assuming a one-sided abrupt junction, comparison of this equation with data for lightly doped substrates yields a lifetime of 2×10^{-8} sec in the p-type substrate.

Using this generation-current model, an attempt was made to correlate the low reverse bias data with substrate concentration. Figure I-10 shows plots of three typical diodes, one on heavily doped material and two on lightly doped material (with and without a hydrogen anneal). At low voltages, the lightly doped unannealed diode could be expected to have current a factor of 4.5 greater than the heavily doped diode because of the difference in depletion width. This is not observed, and may be due to a shorter carrier lifetime in the $4 \times 10^{15} \text{ cm}^{-3}$ material. However, these lifetimes are much smaller than the value of 2×10^{-6} sec which was found in the analysis of the field plate C-V measurements. This discrepancy suggests that the g-r current could be due not to generation in the p-type, but in the n-type region, even though the n-type region is much more heavily doped ($\sim 10^{17} \text{ cm}^{-3}$) than the p-type substrate. This model is consistent with the observation that the g-r current is similar for devices made in the two different substrates.

The power law dependence of current on voltage at high reverse bias, where current scales with perimeter, as shown in Fig. I-9, was characteristic of all diodes measured in this work. It strongly suggests tunneling breakdown.¹³ A comparison with the tunneling current density equation [Eq. (1)]¹⁴ gives further evidence of this phenomena:

$$J_t = \frac{\sqrt{2m^*} q^3 \epsilon V}{4\pi^2 \hbar^2 E_g^{1/2}} \exp\left(-\frac{\pi \sqrt{m^*} E_g^{3/2}}{2\sqrt{2} q \epsilon \hbar}\right) . \quad (1)$$

Here, ϵ is the junction electric field, E_g is the bandgap, V is the applied voltage, m^* is the effective mass, and \hbar is the reduced Planck's constant. Rewriting this equation in terms of the applied voltage V , the diffusion voltage V_D and the carrier concentration N_A , one obtains

$$J_t = \frac{q^{5/2}}{4\pi^2 \hbar^2} \left(\frac{m^* N_A}{\epsilon_s E_g}\right)^{1/2} V(V_D + V)^{1/2} \exp\left[-\frac{\pi}{2\sqrt{2} \hbar q^{3/2}} \left(\frac{2\epsilon_s m^*}{N_A}\right)^{1/2} \frac{E_g^{3/2}}{(V_D + V)^{1/2}}\right] . \quad (2)$$

A plot of $\ln [I/V(V_D + V)^{1/2}]$ vs $(V_D + V)^{-1/2}$ is shown in Fig. I-11 for wafer A-7 for $V > 1.0 \text{ V}$, yielding a linear correspondence as would be expected for tunneling. Similar linear plots were obtained for diodes on all other wafers studied in this work. Assuming $E_g = 0.22 \text{ eV}$, the slope of the line in Fig. I-11 yields an effective mass $m^* = 0.018$, in good agreement with literature values of electron effective mass.¹⁵ A similar calculation for all other lightly doped diodes gave values of $m^* = 0.020 \pm 0.002$. However, calculations for diodes made on the $4 \times 10^{15} \text{ cm}^{-3}$ substrates yielded $m^* = 0.055 \pm 0.005$. The reason for this discrepancy is not known.

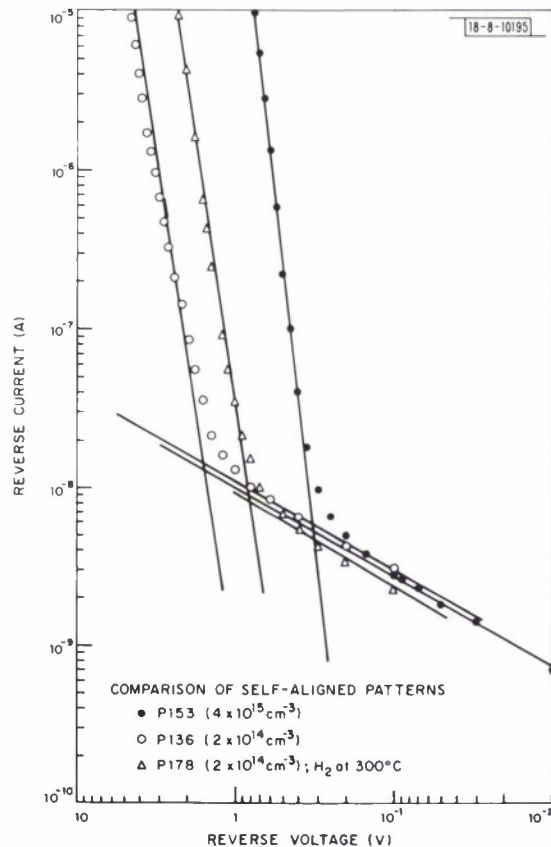


Fig. I-10. Reverse I-V characteristics for typical diodes fabricated on 16-mil-square pattern. P153 is heavily doped, P136 is lightly doped and P178 is lightly doped with a 300°C hydrogen anneal. The generation currents are nearly equal and the hydrogen anneal has lowered the breakdown voltage.

The cause of this tunneling breakdown is presently being investigated. One possible explanation is the formation of a heavily accumulated p-type region under the edge of the field plate where it overlaps the diode (see Fig. I-1). If sufficient bias is applied to the field plate with respect to the substrate to achieve a flat-band condition, the stronger field under the edge of the field plate, due to the reverse bias on the diode, could invert the surface of the n-type region, forming a nearly degenerate p-n junction which could support a tunneling current not unlike that reported in guarded silicon junctions.¹⁶

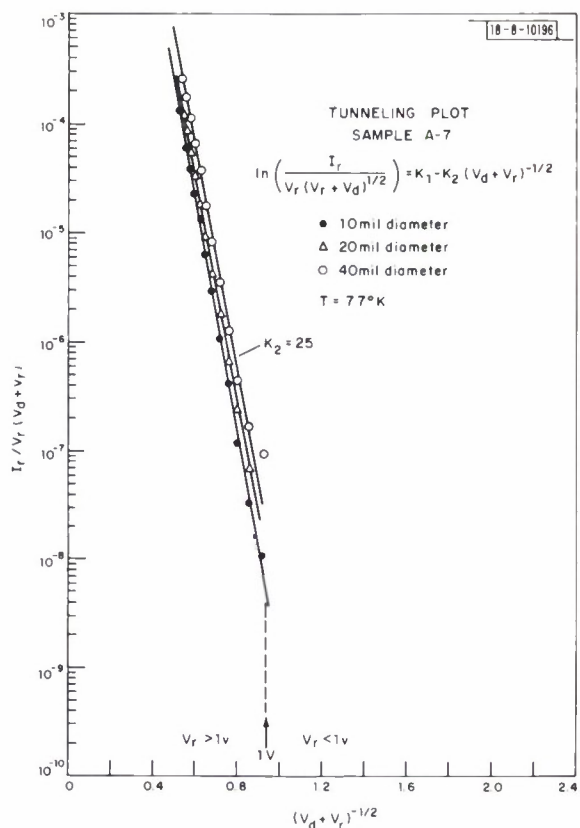


Fig. I-11. Plot of $\ln [I/V(V_D + V)^{1/2}]$ vs $(V_D + V)^{-1/2}$ for data of Figs. I-8 and I-9, for reverse voltages greater than 1 V. The linear correspondence conforms to the tunneling current equation. Similar straight line plots were obtained for all other wafers that were measured.

F. Leonberger J. P. Donnelly
C. E. Hurwitz W. T. Lindley
A. G. Foyt J. N. Walpole

C. HIGH GAIN GaAs SCHOTTKY-BARRIER AVALANCHE PHOTODIODES

Schottky-barrier avalanche photodiodes have been fabricated using lightly doped n-type GaAs epitaxial layers grown on n⁺ GaAs substrates. These devices have shown much higher gain than that observed previously on bulk GaAs with carrier concentrations in the 10¹⁶ range.¹⁷ The

Section I

net carrier concentration of the epitaxial material used was about $2.5 \times 10^{14} \text{ cm}^{-3}$. Schottky barriers were formed in the same device structure used for the previous work¹⁷ by electroplating 5.3-mil-diameter circles of $\sim 100\text{-}\text{\AA}$ -thick semitransparent platinum. Guard rings were formed by proton bombardment with 700-keV protons, which created a high resistivity region $\sim 7\text{ }\mu\text{m}$ deep around the diodes.¹⁸ These guard rings effectively eliminated edge breakdown at the perimeter of the devices and increased the breakdown voltage from ~ 150 to ~ 360 V, although the depletion layer depth at voltages close to reverse breakdown (~ 40 to $50\text{ }\mu\text{m}$) was much larger than the depth of the guard ring. The variation of photocurrent with reverse bias for a particular device is shown in Fig. I-12 for five different primary photocurrents corresponding to incident power levels ranging from 1×10^{-10} to more than 2×10^{-8} W. The wavelength used for these measurements was $0.6328\text{ }\mu\text{m}$, and the zero-bias quantum efficiency at this wavelength was 0.5. For the lowest primary photocurrent of $2.8 \times 10^{-11} \text{ A}$, the maximum average gain or multiplication was 4500 and the observed maximum gain decreased to 295 for a primary photocurrent of $6 \times 10^{-9} \text{ A}$. The large-signal gain saturation observed here is probably due to a decrease in the effective voltage for the carrier multiplication brought about by the presence of the multiplied photocurrent in the depletion region. This decrease can be described in terms of a space-charge layer resistance. The calculated value of this resistance agrees well with the experimental differential resistance of the device in the breakdown region.

G. E. Stillman W. T. Lindley
C. M. Wolfe A. G. Foyt
J. A. Rossi J. L. Ryan

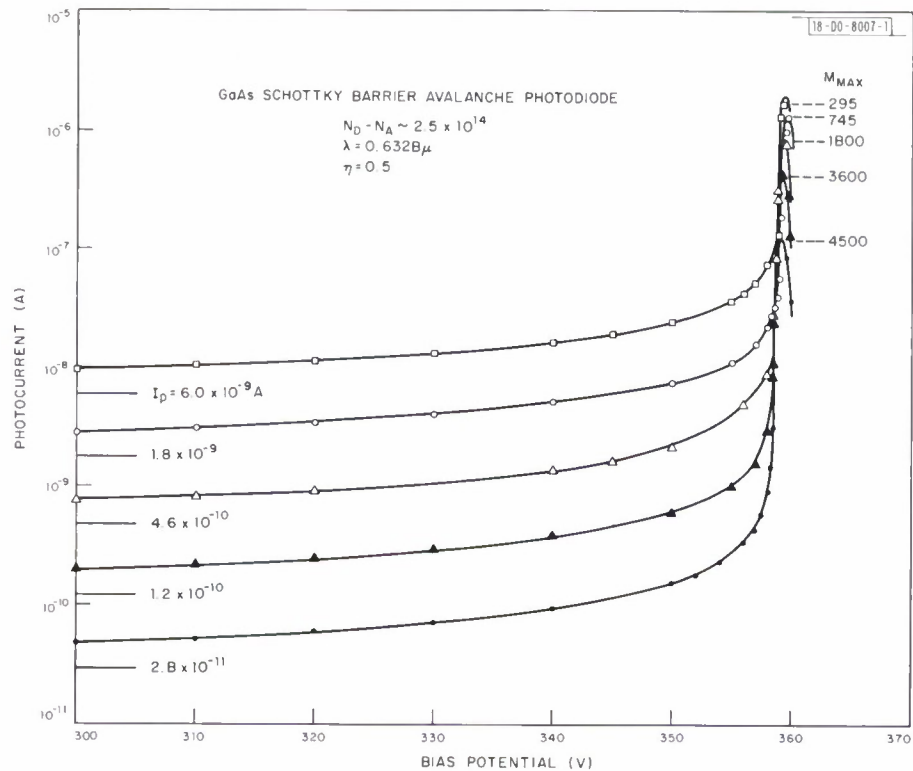


Fig. I-12. Variation of photocurrent with bias potential for five different primary photocurrents. The multiplication at any voltage is the ratio of the photocurrent at that voltage to the primary photocurrent.

D. ZnO/GaAs OVERLAY TRANSDUCERS

Much improved RF coupling to GaAs acoustic surface waves was achieved by sputtering a ZnO film over interdigital transducers. By exploiting the very large electromechanical coupling constant of ZnO films, one expects to be able to efficiently couple into non-piezoelectric and weakly piezoelectric materials. Calculations have shown that the effective surface wave coupling constant in an overlay structure can even exceed that of the overlay material itself.¹⁹

GaAs and ZnO are an excellent mechanical match for the overlay, as they have almost equal mass densities. Since the ZnO Rayleigh-wave velocity in the basal plane (2702 m/sec) is very close to the velocity along the (011) axis for (100) cut GaAs (2864 m/sec), dispersion will be much less significant here than, for example, in the ZnO/Si combination. The unusual character of this propagation mode in GaAs does not introduce any excess loss problems. Our laser probe measurements indicate less than 2.5-dB/ μ sec propagation loss at 741 MHz.

In order to evaluate the overlay film we fabricated 30 finger-pair transducers onto semi-insulating GaAs wafers using 300 \AA of Cr and 1300 \AA of Au. Electrical properties of these transducers have been reported previously.²⁰ A 2.5- μ m layer of ZnO was then RF sputtered in a partial pressure of oxygen onto the entire surface of the wafer.

The presence of the ZnO film increased the transducer capacitance from 2.1 to 3.4 pF. A Smith chart display of transducer radiation impedance is shown in Fig. I-13. The maximum radiation resistance is about 17 ohms, more than a factor-of-4 increase over the plain GaAs transducer. As expected, the center frequency (255.4 MHz) was somewhat less than the 268.8 MHz measured before deposition. The first sidelobes at 266 and 244 MHz are evident in the photograph. The narrow 3.2-percent bandwidth was a consequence of the large number of electrodes in the transducer pattern. If fewer electrodes had been used, an increase in bandwidth of more than a factor-of-2 would have been observed, in addition to the increased radiation resistance.

The increased coupling in these first ZnO/GaAs overlay devices was only about 1/5 that expected from an ideal single crystal film. However, a visual inspection of the overlay revealed numerous pits in the film along the edges of the interdigital electrodes. Improved film quality should yield much better transducer performance in the future.

D. L. Spears

E. X-RAY LITHOGRAPHY: A HIGH RESOLUTION REPLICATION PROCESS

A pattern replication process utilizing soft x-rays has been developed which is capable of sub-micron resolution over areas of several cm^2 . The process is analogous to conventional

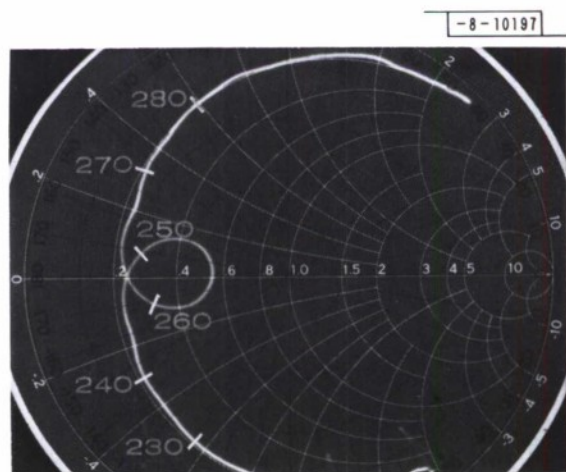


Fig. I-13. Smith chart display of the radiation impedance of a ZnO/GaAs overlay transducer.

Section I

photolithographic contact printing in that a relief pattern is produced in a thin polymer film after exposing it to radiation through a mask. However, by using soft x-rays ($\sim 10 \text{ \AA}$) instead of ultraviolet ($\sim 3000 \text{ \AA}$), the wavelength related diffraction problems which limit the resolution of photolithography are effectively eliminated, and a finite gap between mask and sample is permitted, leading to increased mask life and the elimination of mechanical defects introduced by contact printing.

In this process, an appropriate mask consisting of a semitransparent plate patterned with an x-ray absorbing film is held close to the surface of a polymer-film-coated sample and irradiated by a distant x-ray source, as shown schematically in Fig. I-14. With soft x-rays, diffraction effects are generally negligible, since with a wavelength of 10 \AA , $0.25\text{-}\mu\text{m}$ lines can be resolved over a $60\text{-}\mu\text{m}$ depth of field. A more significant factor affecting resolution is the lateral blurring of the projected image due to the finite size of the x-ray source. As shown in the inset of Fig. I-14, this penumbral distortion δ is directly related to the source diameter d , the distance D between the source and mask, and the spacing s between the mask and sample. Obviously, this effect can be reduced by merely increasing D . However, this would be at a great cost in x-ray intensity which varies as $1/D^2$.

The appropriate wavelength region is dictated by requirements placed on the mask and properties of polymer films. For sub-micron patterns the absorbing film can be no more than about 5000 \AA thick. In order to get over 90 percent x-ray absorption using the most highly absorbing materials (i.e., U, Au, Pt, Ir and Cu), wavelengths greater than 4 \AA must be used.²¹ On the other hand, to obtain more than 25 percent transmission with a flat, rigid substrate using the most transparent solid materials (i.e., Be, Mg, Si, Al and some polymers) λ must be less than 14 \AA . Although the absorption coefficient varies strongly with wavelength ($\sim \lambda^3$), the variation from material to material in the soft x-ray region is not very large. For example, at

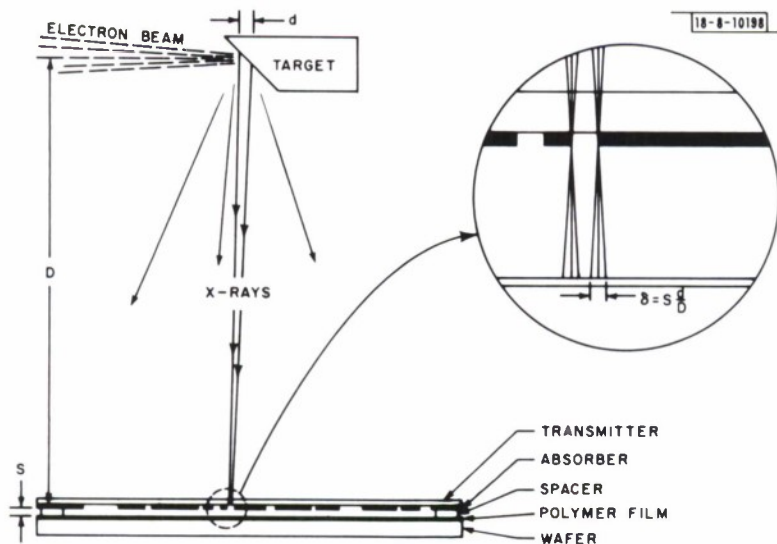


Fig. I-14. Schematic diagram of the x-ray lithographic system. The inset illustrates the penumbral distortion produced by the finite size of the x-ray source.

8.34 \AA uranium and beryllium, the best possible absorber-transmitter combination, differ in absorption coefficient by only a factor of 250, which is in striking contrast to the more than 10^{10} variation available to visible radiation.

Wavelength also enters in when the range of the Auger and photoelectrons produced by the x-rays is considered.²² It is these electrons which produce the radiation damage in the polymer film and "expose" it. The range of electrons in solids is roughly proportional to the square of their energy and inversely proportional to the mass density of the solid. Since polymer films have low densities ($\sim 1 \text{ gm/cm}^3$) λ must be greater than 6 \AA in order to insure a range less than 2000 \AA . The exact choice of wavelength must be made on the basis of tradeoffs among the available x-ray emission lines, pattern resolution, contrast required, exposure time desired and mask-to-sample spacing.

The radiation-sensitive polymer film used in our experiments was polymethylmethacrylate (PMM) having a very narrow molecular weight distribution around 950,000. PMM has been used here and elsewhere as a recording medium for electron-beam pattern generation. Although it is an inefficient absorber of x-rays, it has a number of attractive features: it is resistant to most chemical etchants used in semiconductor processing, it is capable of very high resolution, its solubility characteristics are well established and it is insensitive to visible light. Scission of the polymer chains occurs in PMM upon exposure to high energy radiation, which renders the material soluble in an appropriate mixture of solvent and non-solvent. Films of the unexposed PMM prepared at Lincoln are effectively insoluble in a 40/60 mixture of methyl isobutyl ketone and isopropyl alcohol. This same mixture dissolves away a PMM film at the rate of 50,000 $\text{\AA}/\text{min}$ after it has been exposed to a radiation dose of approximately 1000 J/cm^2 . The rate of dissolution was found to vary strongly with dosage, approximately as the 3rd power.

The exposure time T_c necessary to sufficiently degrade the polymer film with x-rays is given by

$$T_c = [i_e \epsilon \Omega h\nu \tau]^{-1} D_c / \mu , \quad (3)$$

where i_e is the current density of electrons impinging on the target of the x-ray tube, ϵ is the fluorescence efficiency of the target, Ω is the solid angle subtended by the source at the sample, $h\nu$ is the energy of the x-rays, τ is the transmittance of the mask and any other substance between the target and polymer film, μ is the absorption coefficient of the polymer and D_c is the required radiation dose. The low fluorescence efficiency of soft x-rays, typically $< 10^{-4}$ photons/electron/steradian,²³ gives rise to long exposure times.

X-ray lithographic masks using n/n⁺ epitaxial silicon wafers have been made. A high resolution acoustic surface wave transducer pattern was fabricated²⁴ onto the wafer using 300 \AA of chromium and 3000 \AA of gold. The n⁺ silicon substrate material was then electrochemically etched²⁵ away beneath the pattern, leaving the chromium-gold structure supported by a thin ($\sim 3.5 \mu\text{m}$) membrane of epitaxial silicon. A transmission photomicrograph of a portion of one of these masks is shown in Fig. I-15(a). The centers of adjacent transducer fingers are separated by 2.5 μm . Some residual n⁺ silicon substrate material gives rise to the grainy structure above the opaque, gold transducer fingers.

This mask was placed, gold side down, onto a second silicon wafer coated with $\sim 1800 \text{\AA}$ of PMM spun at 2000 rpm. No pressure was applied to the mask. X-ray exposures were carried

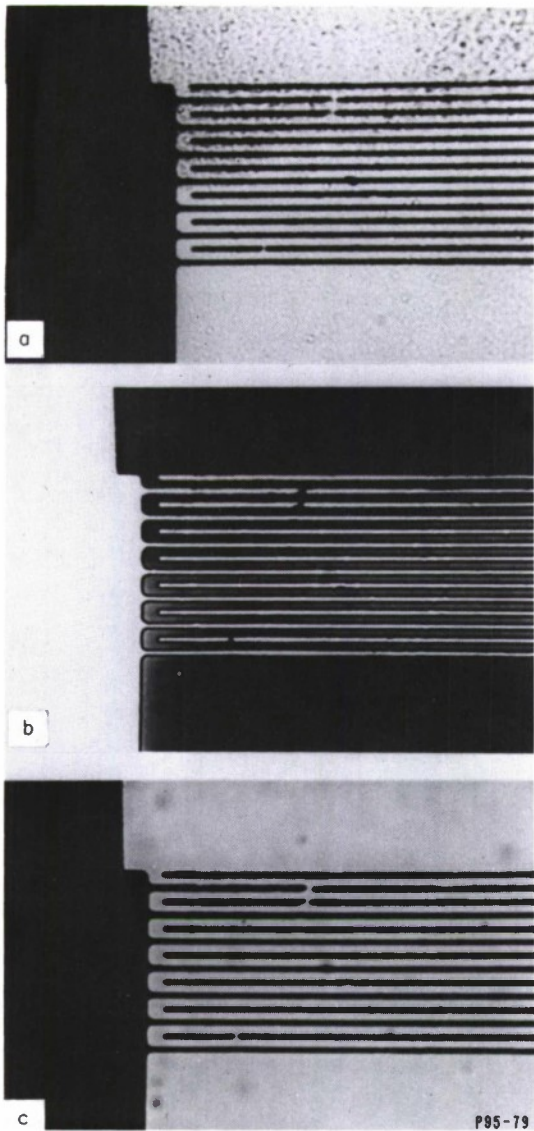


Fig. I-15. Photomicrographs of (a) an x-ray mask for an acoustic surface wave transducer, (b) the pattern reproduced by x-rays in PMM and (c) the pattern reproduced in chromium on silicon. The spacing between the centers of adjacent transducer fingers is $2.5 \mu\text{m}$.

out with a 5-kV tungsten target tube having a 2-mil beryllium window, which had its peak output between 4 and 7 \AA (Ref. 26). After 21 hours of exposure and a developing time of 2 minutes, the relief pattern in the PMM shown in Fig. I-15(b) was obtained. Here, about 1600 \AA of PMM remains on the transducer pads and fingers and $\sim 800 \text{ \AA}$ in the background region. Note the three defective transducer fingers which are faithfully reproduced. Within the detectability limit of the optical microscope, flawless replication was found. The exposure has been repeated a number of times with the same good results; in fact, the $1.25-\mu\text{m}$ lines were resolved with a mask-to-wafer separation as large as $25 \mu\text{m}$. Figure I-15(c) shows the transducer pattern after an additional fabrication step. The film on this sample was irradiated for 51 hours and developed for 45 sec, which removed all the PMM from the exposed areas. A $300-\text{\AA}$ layer of chromium was then electron-beam-evaporated onto the wafer. Acetone was sprayed on the wafer, which dissolved

and washed away the remaining PMM and the chromium covering those parts of the sample. Although what remained on the sample is not a useful transducer (the background was chromium, not the pads and fingers), the capability of the x-ray lithographic process is clearly demonstrated. These results are even more striking when one considers the fact that with the x-ray source used, the pattern mask had a contrast ratio of less than 3:1.

Obviously, if this process is to be practical, the exposure time must be greatly reduced. The tungsten tube is far from the optimum source. According to Eq. (3), exposure times of a few minutes are attainable by using characteristic radiation from an aluminum ($\lambda_{K\alpha} = 8.34 \text{ \AA}$) or copper target ($\lambda_{L\alpha} = 13.3 \text{ \AA}$) and by operating them at maximum allowable power levels. Indeed, PMM has been adequately exposed in 12 minutes with an aluminum target. In addition, the contrast ratio for the above mask will be over 4:1 with the aluminum target and over 50:1 with the copper target. These high-power soft x-ray sources are under construction.

D. L. Spears
H. I. Smith
E. Stern

F. OBSERVATION OF THE FAR FIELD MODE PATTERN OF A PbTe DIODE LASER USING UPCONVERSION IN A ZnS PHOSPHOR

The infrared upconversion properties^{27,28} of ZnS phosphor powder excited with an ultraviolet (UV) light have been used to visually observe and photograph the far field pattern of a 6.5- μm PbTe diode laser. The ZnS powder deposited on sapphire and cooled to $T = 4.2 \text{ }^\circ\text{K}$ was first illuminated for 30 to 40 sec by intense UV light produced by the $\lambda = 4358 \text{ \AA}$ line of a 200-W high pressure mercury arc. Following removal of the UV light, the green ZnS luminescence (afterglow) produced by this source was allowed to decay for 10 to 15 sec before the PbTe diode laser was turned on. Both the PbTe diode and the ZnS phosphor were located in the same liquid helium cold finger dewar. The CW PbTe diode emitting less than 5 μW at 300 mA of current was separated from a 0.5-inch-diameter ZnS screen by 0.6 inch. When the diode current was switched on, a complex mode pattern was clearly observed for a period of ~ 1 sec. While the frequency spectrum of the diode indicated 80 percent of the diode power in a single frequency mode, the far field pattern consisted of numerous vertical stripes (perpendicular to junction plane), each of which consisted of considerable structure. Each of these vertical stripe patterns was similar to the diffraction pattern of a rectangular slit with its length parallel to the junction plane. The single frequency and complex far-field pattern may be consistent with a single mode which is reflected internally by both the cleaved end mirrors and the cleaved sides of the diode. Such a mode might be incident on the output mirror at several different angles and locations. It is estimated that less than $1 \mu\text{W}/\text{cm}^2$ is required to produce a visible mode pattern on the phosphor for the PbTe laser wavelength $\lambda = 6.5 \mu\text{m}$. The upconversion efficiency remains high past $\lambda = 10 \mu\text{m}$, indicating that this technique may have significant applications in the evaluation of Pb salt diode lasers.

K. W. Nill A. R. Calawa
W. J. Scouler T. C. Harman

G. CALIBRATION OF TUNABLE DIODE LASERS USING A CONFOCAL FABRY-PEROT INTERFEROMETER

A confocal Fabry-Perot interferometer (FPI) has been used to calibrate the tuning rate of $\text{PbS}_{1-x}\text{Se}_x$ diode lasers²⁹ operating near $5.2 \mu\text{m}$. The transmission characteristic of the

Section I

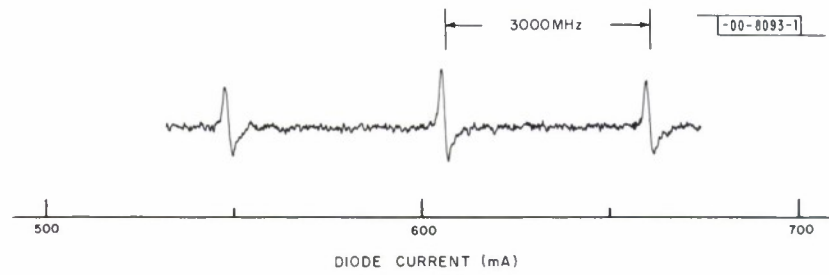


Fig. I-16. Derivative spectrum of the transmission of a FPI with a free spectral range of 3000 MHz and a finesse of ≥ 50 . The frequency of this $\text{PbS}_{0.6}\text{Se}_{0.4}$ diode laser is approximately 1876 cm^{-1} .

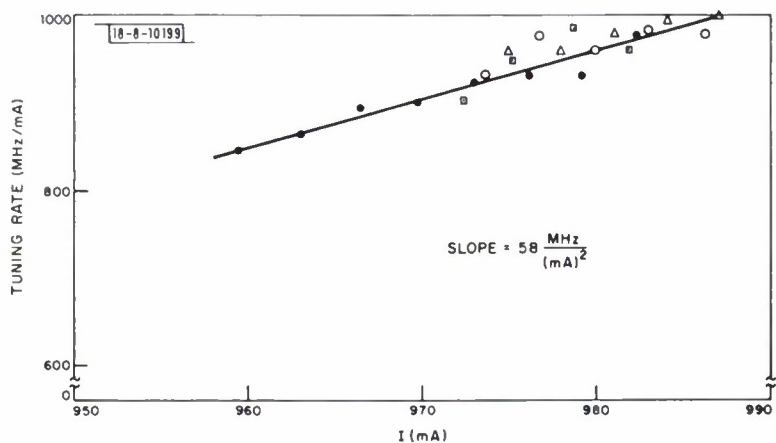


Fig. I-17. Tuning rate vs current for a $\text{PbS}_{0.6}\text{Se}_{0.4}$ laser operating at 1903 cm^{-1} . The points are a composite of several calibration sweeps.

spherical confocal FPI used here³⁰ is a series of windows ~ 30 MHz wide, equally spaced in frequency, with a spacing of $\Delta f = c/4l \approx 3000$ MHz. Here l is the radius of curvature of the highly reflecting side of the mirror, as well as the inter-mirror spacing (spherical confocal) and c is the speed of light in the medium between the mirrors. The CaF_2 mirrors used in these experiments were 1 inch in diameter and had a 25-mm radius of curvature. These mirrors were commercially coated to 98-percent reflectivity with less than 1/2-percent absorption loss over the range 4.5 to 5.5 μm . Use of zinc sulfide and thorium fluoride dielectric films in the coating produced infrared mirrors which were highly transmitting (~ 50 percent) in the visible. Consequently, it was possible to obtain initial alignment of the mirrors using a He:Ne laser operating at 0.6328 μm . A commercially available electronically adjusted instrument was used to obtain alignment of the CaF_2 mirrors. The FPI finesse was found to be between 50 and 100, depending critically on the optical alignment between the semiconductor laser, collecting lens and interferometer axis.

In order to calibrate a laser, the interferometer was placed between a collimating lens and a collecting lens which focused the transmitted radiation on the slits of a grating spectrometer. The spectrometer was used to measure the absolute frequency of the mode being calibrated and isolate it from the other modes of the multimode laser output. Figure I-16 shows a derivative spectrum obtained by frequency modulating the laser and synchronously detecting the modulated transmission of the FPI. The laser is calibrated by measuring the current change necessary to tune its output over the frequency interval of 3000 MHz. This $\text{PbS}_{0.61}\text{Se}_{0.39}$ laser had a mode near 1876 cm^{-1} , whose tuning rate changed from 22 to 55 MHz/mA as the current range was increased from 150 to 650 mA. Over the current range shown in Fig. I-16, the tuning rate changes from about 52 to 55 MHz/mA. Tuning rates for PbSSe lasers have been measured over the range of 22 to 1000 MHz/mA. For some lasers, a small but measurable change in tuning rate has been observed over a period of time, apparently resulting from changes in such factors as the condition of the cold finger dewar.

Figure I-17 shows the measured tuning rate vs current for a $\text{PbS}_{0.6}\text{Se}_{0.4}$ diode operating at 1903 cm^{-1} . The points indicate tuning rates measured over a two-day period. The scatter in the data is ± 2.5 percent due to a number of factors including thermal drifts in the FPI. It is apparent that a significant change in tuning rate (0.7 percent/GHz) occurs over this range of current. Current work is directed toward reducing the thermal drift problem and facilitating the optical alignment procedure. The stable, high finesse FPI should achieve wide use as a convenient and precise technique for calibrating the tuning rate of tunable infrared laser sources.

K. W. Nill A. R. Calawa
F. A. Blum T. C. Harman

H. STRIPE-GEOMETRY - $\text{Pb}_{1-x}\text{Sn}_x\text{Te}$ DIODE LASERS

In order to avoid parasitic modes which occur in conventional rectangular diode laser structures, stripe-lasers similar to the GaAs lasers previously investigated³¹ have been fabricated from vapor-grown $\text{Pb}_{0.88}\text{Sn}_{0.12}\text{Te}$. After electrolytically etching the surfaces, a diffusion mask was formed by pyrolytically depositing a 1500- \AA SiO_2 layer and opening 50- μm -wide stripes on 125- μm centers in the oxide in a direction perpendicular to a (100) crystal plane. A 20- μm -deep n region was diffused into the open regions of the p-type substrates at 450 °C using

Section I

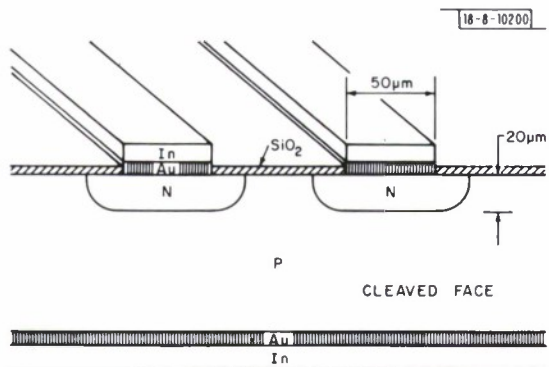


Fig. I-18. End view of $\text{Pb}_{1-x}\text{Sn}_x\text{Te}$ stripe-geometry diode lasers.

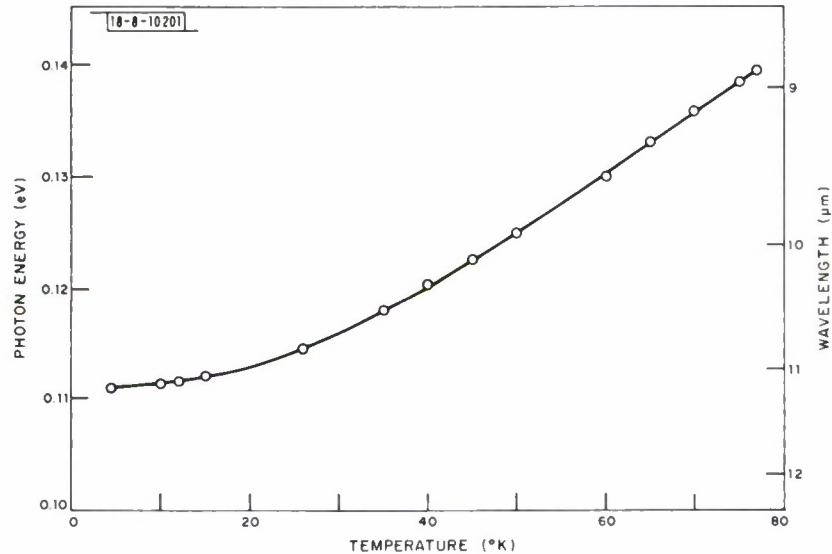


Fig. I-19. Temperature dependence of the photon energy of a $\text{Pb}_{1-x}\text{Sn}_x\text{Te}$ stripe-geometry laser.

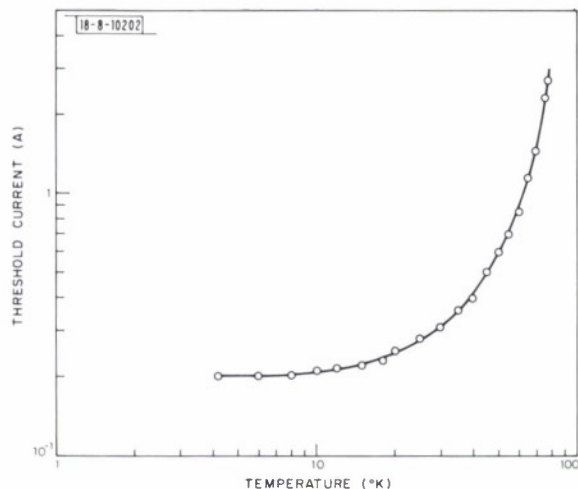


Fig. I-20. Temperature dependence of the laser threshold current for a $\text{Pb}_{1-x}\text{Sn}_x\text{Te}$ stripe-geometry laser.

a metal-rich $\text{Pb}_{0.88}\text{Sn}_{0.12}\text{Te}$ source. Contacts to both n and p regions were formed by plating a layer of gold and a subsequent layer of indium. The cavity, typically $500\text{ }\mu\text{m}$ long, was formed by cleaving along the (100) plane. A cross section of the completed structure is shown in Fig. I-18.

At $4.2\text{ }^\circ\text{K}$, threshold currents of about 100 mA (150 A/cm^2) have been achieved in preliminary devices and CW operation has been possible. The spectra consisted of regularly spaced modes corresponding to the longitudinal cavity. The far-field pattern was a single lobe with beam angles of 20° in the vertical plane (with reference to Fig. I-18) and 8° in the horizontal plane, corresponding to a fundamental spatial mode of an emitting region extending about $30\text{ }\mu\text{m}$ perpendicular to the junction plane and $70\text{ }\mu\text{m}$ along the junction. The $70\text{-}\mu\text{m}$ value is in satisfactory agreement with the actual width of the junction.

The variation of wavelength with temperature shown in Fig. I-19 is similar to the variation observed in $\text{Pb}_{1-x}\text{Sn}_x\text{Se}$ diode lasers.³² The temperature variation of threshold current in Fig. I-20 shows a relatively slow increase at temperatures below $30\text{ }^\circ\text{K}$ and a rapid increase at higher temperatures. At $77\text{ }^\circ\text{K}$ the threshold is 13 times higher than at $4.2\text{ }^\circ\text{K}$.

I. Melngailis
W. T. Lindley
A. R. Calawa

REFERENCES

1. T. C. Harman, Solid State Research Report, Lincoln Laboratory, M. I. T. (1970:3), p. 2, DDC AD-714079.
2. L. J. van der Pauw, Philips Res. Rept. 13, 1 (1958).
3. J. Lindhard, M. Scharff and H. E. Schiott, Mat. Fys. Medd. 33, 1 (1963).
4. A. G. Foyt, W. T. Lindley and J. P. Donnelly, Appl. Phys. Letters 16, 335 (1970), DDC AD-709748.
5. A. S. Grove, B. E. Deal, E. H. Snow and C. T. Sak, Solid-State Electron. 8, 145 (1965).
6. S. M. Sze, Physics of Semiconductors (Wiley & Sons, New York, 1969).
7. L. M. Terman, Solid-State Electron. 5, 285 (1962).
8. T. M. Buck, H. C. Casey, Jr., J. V. Dalton and M. Yamin, Bell System Tech. J. 47, 1827 (1968).
9. R. Y. Hung and E. T. Yon, J. Appl. Phys. 41, 2185 (1970).
10. J. Hilibrand and R. D. Gold, RCA Review 21, 245 (1960).
11. C. T. Sah, R. N. Noyce and W. Shockley, Proc. IRE 45, 1228 (1957).
12. A. S. Grove, Physics and Technology of Semiconductor Devices (Wiley & Sons, New York, 1967).
13. A. R. Riber and D. L. Feucht, Solid State Electron. 9, 1055 (1966).
14. J. L. Moll, Physics of Semiconductors (McGraw-Hill, New York, 1964).
15. M. Neuberger, Indium Antimonide, Hughes/EPIC Data Sheet #121 (1965), p. 25.
16. A. S. Grove and D. J. Fitzgerald, IEEE Trans. Electron Devices 12, 619 (1965).
17. Solid State Research Report, Lincoln Laboratory, M. I. T. (1969:1), p. 1, DDC AD-687100; W. T. Lindley, R. J. Phelan, Jr., C. M. Wolfe and A. G. Foyt, Appl. Phys. Letters 14, 197 (1969), DDC AD-694323.
18. A. G. Foyt, W. T. Lindley, C. M. Wolfe and J. P. Donnelly, Solid-State Electron. 12, 209 (1969), DDC AD-694145.
19. L. P. Solie, Appl. Phys. Letters 18, 111 (1971).
20. Solid State Research Report, Lincoln Laboratory, M. I. T. (1971:2), p. 10, DDC AD-732923.
21. K. F. J. Heinrich in The Electron Microprobe, T. D. McKinley, K. F. J. Heinrich and D. B. Wittry, Eds. (Wiley, New York, 1966).
22. V. E. Cosslett and W. C. Nixon in X-Ray Microscopy (University Press, Cambridge, 1960).
23. M. Green in X-Ray Optics and X-Ray Microanalysis, H. H. Pattee, V. E. Cosslett and A. Engstrom, Eds. (Academic Press, New York, 1963), p. 185.
24. H. I. Smith, F. J. Bachner and N. Efremow, J. Electrochem. Soc. 118, 821 (1971), DDC AD-729609.
25. R. L. Meek, J. Electrochem. Soc. 118, 1240 (1971).
26. X-Ray Microscopy and Microradiography, V. E. Cosslett, A. Engstrom and H. H. Pattee, Eds. (Academic Press, New York, 1957), p. 64.
27. G. Baur, N. Riehl and D. Thoma, Zeit für Physik 206, 229 (1967).
28. W. J. Scouler, D. H. Dickey and T. M. Quist, Proceedings of the 19th National Infrared Information Symposium, Monterey, California, 2-4 June 1971.
29. Solid State Research Report, Lincoln Laboratory, M. I. T. (1971:2), p. 5, DDC AD-732923.
30. M. Hercher, App. Opt. 7, 951 (1968).
31. J. C. Dymant, Appl. Phys. Letters 10, 84 (1967).
32. T. C. Harman, A. R. Calawa, I. Melngailis and J. O. Dimmock, Appl. Phys. Letters 14, 333 (1969), DDC AD-694136.

II. QUANTUM ELECTRONICS

A. OPTICALLY PUMPED ROOM TEMPERATURE $\text{In}_x\text{Ga}_{1-x}\text{As}$ LASERS

Studies have continued on optically pumped lasers fabricated from III-V semiconductor material. By using samples of $\text{In}_x\text{Ga}_{1-x}\text{As}$ and a Q-switched Nd:YAG laser as the excitation source, coherent emission over a temperature range of 150° to 300°K was observed. This corresponds to a variation in laser wavelength from 1.08 to 1.12 μm . The lower limit of this wavelength range is established by the tendency for the samples of this particular alloy composition and doping to become transparent to the pump source (1.06 μm). The upper temperature (or longer wavelength limit) has not yet been established. Efficiency measurements indicate overall efficiencies ~ 0.6 percent at room temperature.

The samples, as obtained,* consist of a vapor epitaxial layer of $\text{In}_x\text{Ga}_{1-x}\text{As}$ grown on a GaAs substrate. The room temperature carrier concentrations are about $5 \times 10^{17} \text{ cm}^{-3}$ for all samples used here,¹ and all the epitaxial layers are n-type. Since the substrates used were conducting, no further electrical characterization was attempted. A reasonable estimate of the alloy composition may be obtained from a knowledge of the sample absorption data (furnished by the supplier) and reference to the data of Coderre and Wooley.² The samples were polished to a final thickness between 12 and 50 μm and subsequently etched in a cold solution of $\text{H}_2\text{SO}_4:\text{H}_2\text{O}_2:\text{H}_2\text{O}$. The samples were then cleaved to the desired cavity lengths and mounted on a TO5 header. A variety of different mounting techniques has been tried (oil, water, alloying, etc.). The resulting sample output is independent of the method used. This occurs simply because the sample thickness is always much greater than the $1/\alpha$ penetration depth (probably $\sim 1 \mu\text{m}$) of the exciting radiation and because experiments were done on a pulsed basis.

To excite the samples, the TEM_{00} mode output of a Q-switched Nd:YAG laser operating at 100 pulses per second (laser operation at pulse rates up to 3500 Hz was achieved) was focused onto the sample by a cylindrical lens, yielding an image roughly $20 \mu\text{m} \times 3 \text{ mm}$. Since typical sample cavity lengths were 150 μm (much less than the 3-mm beamwidth), this arrangement provided a nearly uniform excitation intensity in the form of a line source across the sample face. Sample light from one of the cleaved edges (i.e., perpendicular to the direction of excitation) was focused onto the entrance slit of a 3/4-m, double-grating spectrometer. The dispersed radiation was detected by a cooled S-1 photomultiplier, used in conjunction with a boxcar integrator and appropriate amplifiers. Radiation from the other cleaved face was first filtered to eliminate the scattered 1.06- μm pump light and then focused onto a calibrated silicon photodetector. In this manner, both the sample emission spectrum and the power output could be monitored simultaneously.

Figure II-1 shows the room temperature emission spectra well below and well above threshold from a typical sample of composition $x \approx 0.20$. The spontaneous emission spectrum was taken in the forward transmission geometry (i.e., pump and gathered sample light collinear). As shown

* Samples supplied by Spectronics Incorporated, Dallas, Texas.

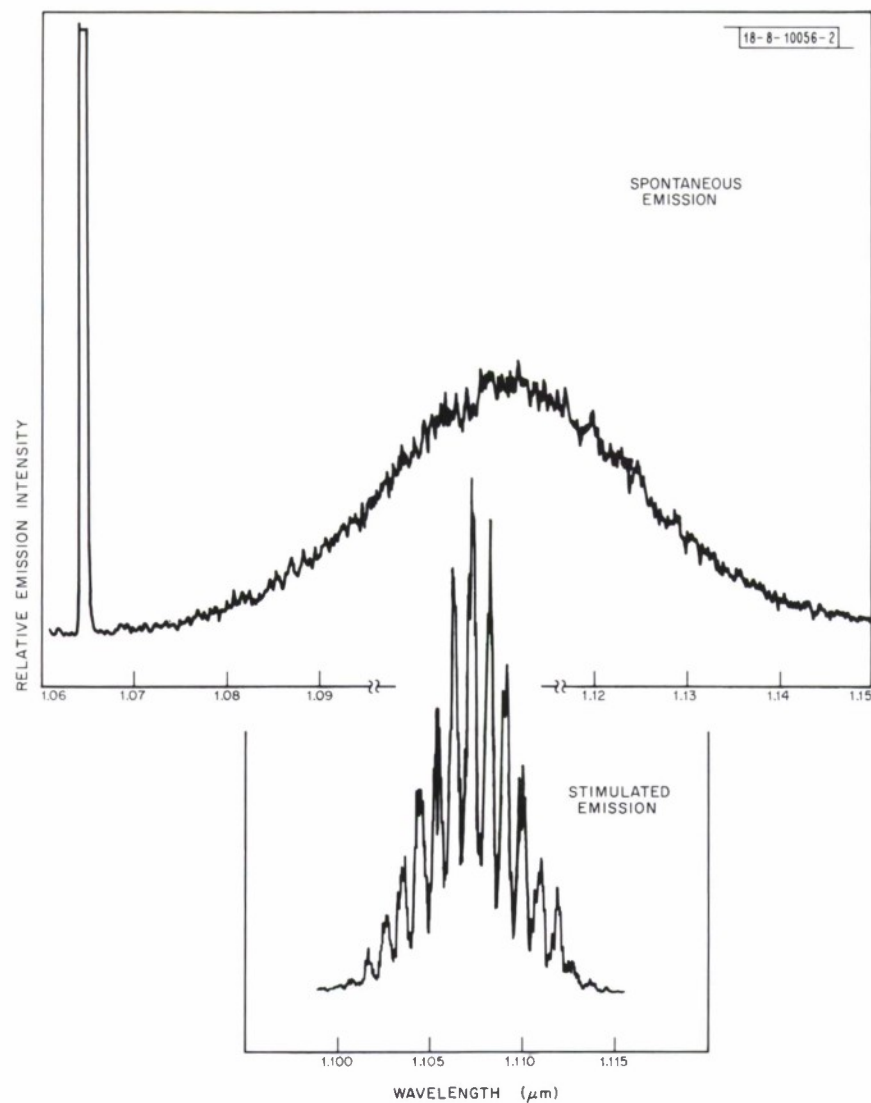


Fig. II-1. Spontaneous and stimulated emission spectra in $\text{In}_{0.2}\text{Ga}_{0.8}\text{As}$ operated at 300°K. Note the difference in wavelength scales.

in the upper portion of Fig. II-1, the spontaneous emission is quite broad and has a long tail extending to higher energy (shorter wavelength) than would normally be expected. However, since some of the graded growth layer still remains on the back of the sample, this is not an unexpected event.

The lower half of Fig. II-1 shows the laser output of a cleaved sample taken well above threshold. The observed longitudinal mode spacing is about 0.9 nm. Although the index of refraction and dispersion are well known for GaAs and InAs, there are little data on the mixed alloy system; hence a rigorous check of experiment and theory is impossible. However, using the standard expression for the mode spacing and numbers appropriate for GaAs, a mode spacing of ~ 0.8 nm was calculated for this sample, which agrees well with the observed value. Similar stimulated emission spectra were also observed in samples having a different alloy composition, in which the peak emission centered near 1.09 μm at room temperature. Thus, room temperature operation has been observed at 1.09 and 1.12 μm and presumably can be achieved anywhere in between. As the temperature is lowered, all the samples continued to lase until the widening gap rendered the 1.06- μm pump useless.

The individual mode widths at 300°K were measured to be 0.4 nm, much larger than the spectrometer resolution of 0.05 nm. This large width may be attributed to the presence of unresolved transverse modes near the longitudinal modes and/or to a wavelength shift caused by a slight, but rapid, change in sample temperature during the pump laser pulse.

For the sample in Fig. II-1, a direct measurement was made of the pump laser power at the focus being transmitted through 158- μm slits, which corresponds to the sample's cavity length. Using calibrated neutral density filters and a calibrated silicon photodiode power meter, a peak power of 3.5 W incident on the sample was measured. Since inserting an additional 50 percent attenuation in the pump beam stopped the sample's stimulated emission, this pump power density of 1×10^5 W/cm² is believed to be within 50 percent of threshold intensity.

In Fig. II-2 the relative laser output from the sample was plotted as a function of the relative input pump intensity. The measurements take into account reflection of the pump excitation at the sample face and radiation emitted from both cleaved edges of the sample. Typical values of the maximum room temperature conversion efficiency of 0.6 percent were measured, with 1 percent being the best observed value. Increasing the incident pump intensity approximately 10 to 25 percent beyond the last point shown in Fig. II-2 results in damage to most samples. This damage is caused by the Nd:YAG pump beam and is not damage to the sample cleaved faces by the sample's own laser signal.

Because of the large variation in band-gap energy of this alloy system, further laser operation may be possible at room temperature over a wider wavelength range by utilizing extensions of the techniques presented here.

J. Rossi
S. Chinn
A. Mooradian

B. DETERMINATION OF THE ν_1 -BAND CENTER OF SO_2 BY TUNABLE LASER SPECTROSCOPY

A new value of the ν_1 -band center of SO_2 has been found by comparing the tunable laser absorption spectrum of this molecule with that of NH_3 in the vicinity of 8.5 μm . These spectra were taken using a diode laser fabricated from $\text{Pb}_{0.93}\text{Sn}_{0.07}\text{Te}$ vapor grown by a closed-tube

Section II

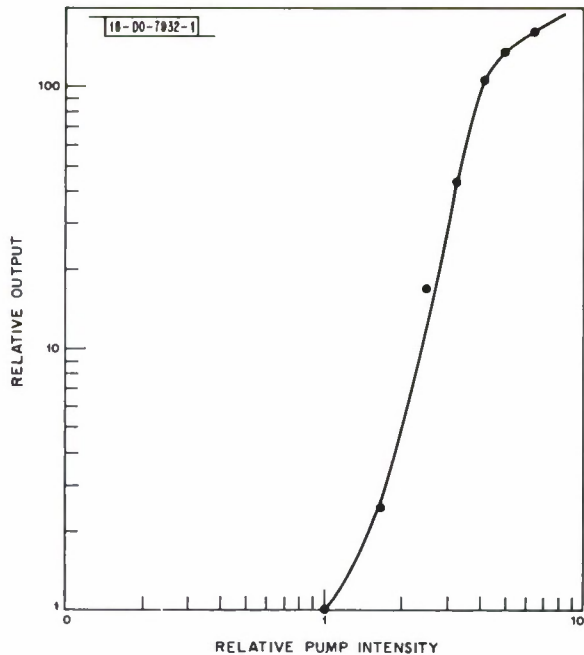


Fig. II-2. Relative sample laser output power vs relative input pump intensity at room temperature. For this particular sample, the total overall efficiency near the top of the curve is ~ 0.6 percent.

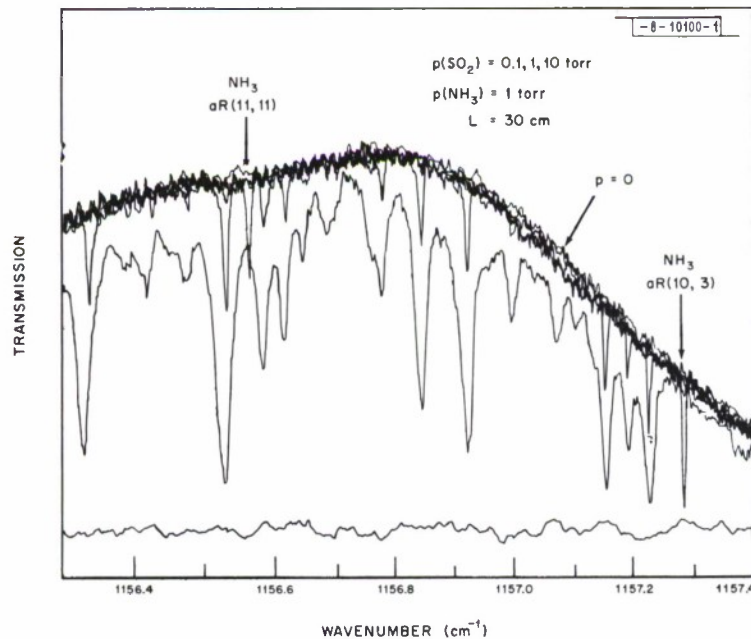


Fig. II-3. Diode laser scans of SO_2 and NH_3 absorption lines. SO_2 scans were taken at 0.1, 1 and 10 torr; NH_3 , at 1 torr. The absorption cell length was 30 cm.

horizontal process. These lasers had threshold current densities on the order of 300 A/cm^2 and output powers of 1 to $10 \mu\text{W}$ per mode. The diodes can be current tuned over a large number of Doppler-limited absorption lines.

A theoretical SO_2 spectrum is calculated³ using accurate microwave values⁴ for the rotational constants of both the ground and first excited state of the ν_1 -mode. The theoretical spectrum is then compared with the experimental spectrum (see Fig. II-3) and the transitions are identified. The SO_2 transitions are unlabeled in the figure. However, as an example, the large peak just to the left of the $\text{aR}(11, 11)\text{NH}_3$ line is the transition $(18, 2, 16) \leftarrow (18, 1, 17)$ where the three quantum numbers are J , K_A and K_C , respectively. The frequency of these SO_2 transitions was determined relative to absorption lines of accurately known NH_3 transitions.⁵ A preliminary value for the frequency of the ν_1 -band center was found to be $1151.71 \pm 0.01 \text{ cm}^{-1}$, which can be compared with the value of 1151.38 cm^{-1} given by Shelton, *et al.*⁶ The uncertainty of $\pm 0.01 \text{ cm}^{-1}$ is due in part to the uncertainty in the ammonia spectra and in part to the intercomparison of the ammonia and SO_2 spectra. A more careful statistical analysis should yield a more accurate value.

A. R. Calawa E. D. Hinkley
S. A. Clough* P. L. Kelley

C. RAMAN SCATTERING IN PARATELLURITE: TELLURIUM DIOXIDE

Tellurium dioxide is known to exist in three crystalline forms – orthorhombic D_{2h}^{15} (known as tellurite), tetragonal D_4^4 (known as paratellurite) and tetragonal D_{4h}^{14} (isomorphous to rutile). Paratellurite is an insulator, transparent from 0.33 to $6.5 \mu\text{m}$; it lacks a center of inversion and is piezoelectric and optically active. It has been synthesized in rather large specimens and has been shown to have interesting acousto-optic⁷ and nonlinear optical⁸ properties.

The unit cell contains four molecular units resulting in 36 phonon branches with Γ -point symmetries $4A_1 + 5A_2 + 5B_1 + 4B_2 + 9E$. Of these, $1A_2 + 1E$ comprise the acoustic modes; the singlet A_2 modes are infrared-active in the extraordinary ray; and the doublet E modes are infrared-active in the ordinary ray. All the optical branches are Raman-active except for the A_2 . Survey Raman spectra of paratellurite taken at 85°K are shown in Fig. II-4. All the Raman modes, except for $1A_1 + 2E$, have been observed and identified by their polarization selection rules. This rich spectrum contains some very strong and sharp peaks compared to similar oxides such as rutile and α -quartz, which indicates relatively large polarizabilities and weak anharmonic forces. This correlates with the unusually strong acousto-optical properties of paratellurite.⁷ Furthermore, the study indicates that paratellurite is a promising candidate for stimulated Raman and polariton scattering and for far-infrared difference frequency generation.

A. S. Pine
G. Dresselhaus

* Optical Physics Laboratory, Air Force Cambridge Research Laboratories.

Section II

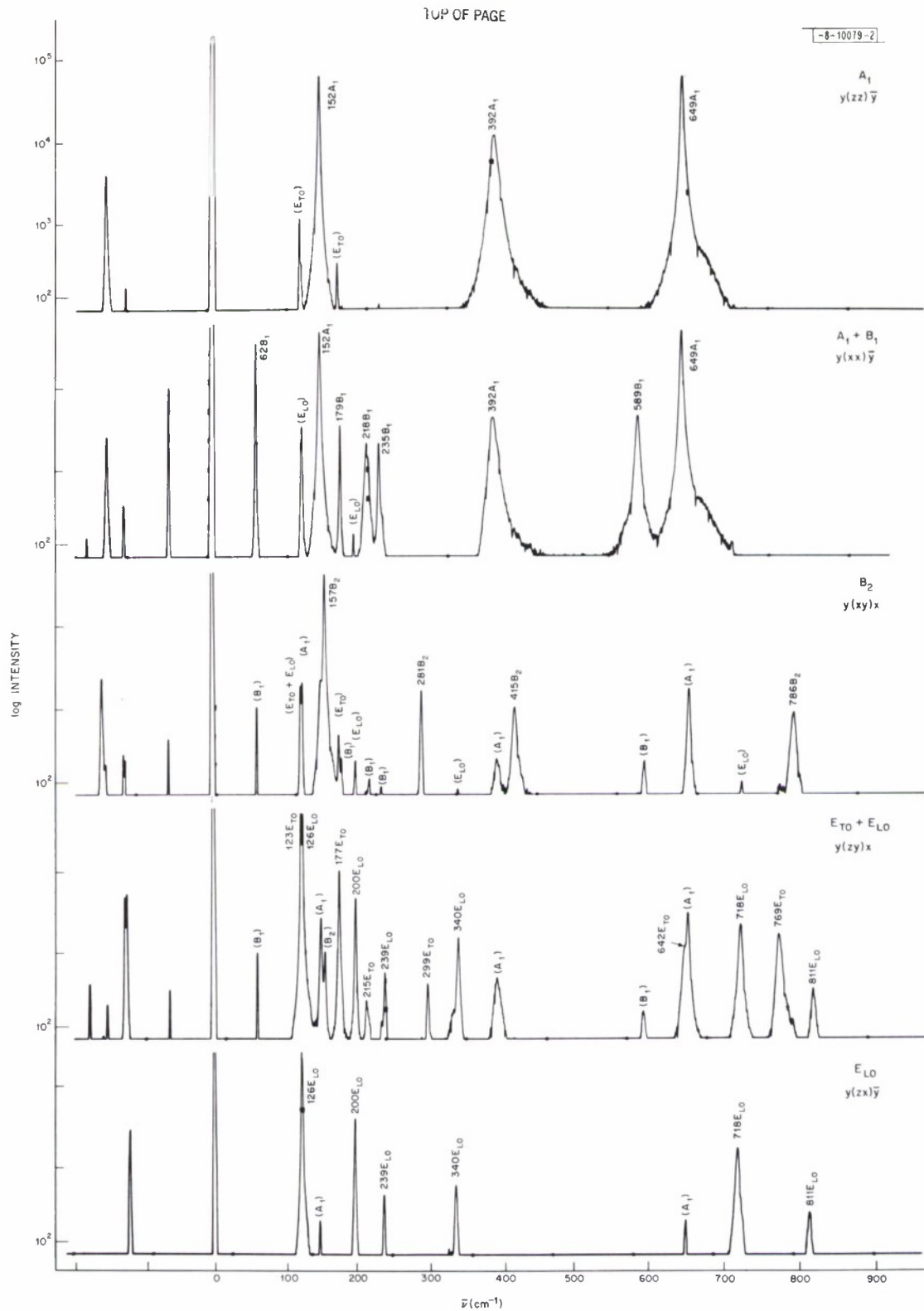


Fig. II-4. Raman spectra of TeO_2 at 85°K .

REFERENCES

1. E. Mehal, Spectronics Inc., private communication.
2. W.M. Coderre and J.C. Wooley, Can. J. Phys. 48, 463 (1969).
3. W.S. Benedict, S.A. Clough, L. Frenkel and T.E. Sullivan, J. Chem. Phys. 53, 2565 (1970).
4. G. Steenbeckeliers, Ann. Soc. Sci. Bruxelles 82, 331 (1968).
5. K.N. Rao, J.B. Curtin and P. Yin (to be published); ammonia transitions identified from J.S. Garing, H.H. Nielsen and K.N. Rao, J. Mol. Spectry. 3, 496 (1959).
6. R.D. Shelton, A.H. Nielsen and W.H. Fletcher, J. Chem. Phys. 21, 2178 (1953).
7. N. Uchida and Y. Ohmachi, Japan. J. Appl. Phys. 9, 155 (1970).
8. W.A. Bonner, S. Singh, L.G. VanUitert and A.W. Warner (to be published).

III. MATERIALS RESEARCH

A. CZOCHRALSKI GROWTH OF FeO SINGLE CRYSTALS

At high temperatures the homogeneity range of wüstite, FeO_x , is $1.05 < x < 1.20$. Whether or not sub-phases exist within this region, as proposed by Vallet and Raccah,¹ is a matter of controversy. To obtain additional evidence concerning this question, Hayakawa and Cohen of Northwestern University are making lattice parameter measurements at high temperatures on single crystals of wüstite grown in our laboratory.

Wüstite crystals have previously been grown by the Czochralski method from an RF-heated melt in a water-cooled copper crucible.² Our crystals were pulled from an arc-melted charge under an argon atmosphere in a tri-arc Czochralski furnace³ that has been used for the growth of such compounds as NbO , VO and Ti_2O_3 . The pulling rate was about 2 cm/hr and the rotation rate about 60 rpm. When growth was initiated by dipping the molybdenum seed rod directly into the melt, several sizable crystals with their growth axis in the $\langle 100 \rangle$ direction were generally obtained. The largest crystal, of centimeter dimensions, was grown from a $\langle 100 \rangle$ -oriented seed cut from one of the spontaneously nucleated crystals. The boule containing this crystal and several smaller ones is shown in Fig. III-1.

-8-10145

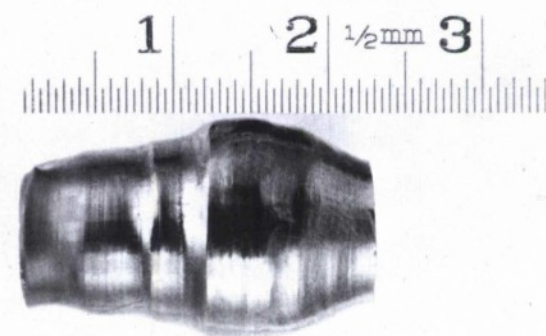


Fig. III-1. Boule of wüstite (FeO_x), consisting of one large crystal and several smaller ones, grown in the tri-arc Czochralski furnace.

The charge, weighing about 30 g, was a mixture of high purity Fe and Fe_2O_3 powders. Its composition was found to be critical for successful growth. Single crystals were rather easily grown with a charge composition of $\text{FeO}_{1.09}$, but polycrystalline boules were obtained for $\text{FeO}_{1.08}$ and $\text{FeO}_{1.12}$. Since the equilibrium partial pressure of oxygen over wüstite at the melting point (1400°C) is only 10^{-10} atm, the melt composition does not change appreciably during the time required for growing a crystal.

The crystal compositions, determined by combustion and wet chemical analysis, were in the range $1.094 < x < 1.104$. The principal impurities were Cu, Si, Sn, V and Zr, totaling about 0.05 weight percent. Although in thermodynamic equilibrium wüstite decomposes to Fe and

TABLE III-1
OXYGEN PARTIAL PRESSURES OF SOME LABORATORY GASES

Gas	Treatment	pO	
		Measured	Calculated or Independently Measured
Argon	As-received	5.5	5.4 ^(c)
	Water-saturated	4.0	7.5 ^(d)
	Ti-gettered	22.1	44.2 ^(e)
	Ti-gettered + (a)	17.0	
	Ti-gettered + (b)	4.1	
Argon + 1% O ₂	As-received	2.1	2.0 ^(f)
Helium	As-received	22.7	
Hydrogen	As-received	28.3	30 ^(g)
	Water-saturated	22.5	22.5 ^(d)
	Ti-gettered	30.5	44.2 ^(e)
	Liquid N ₂ -trapped	29.9	
	Pd-diffused	29.7	

NOTES:

- (a) Passed through 6 m of 0.2-cm-diameter Tygon tubing at 2000 cm³/min
- (b) Same as (a), but rate of 150 cm³/min
- (c) From supplier's analysis of 3.7 ppm O₂
- (d) Calculated from H₂O/H₂ ratio
- (e) Calculated pO over Ti-TiO mixture
- (f) From supplier's analysis of 1% O₂
- (g) From supplier's measured dew point (-120°F)

Fe_3O_4 below 576°C , neither of these phases could be detected by x-ray diffraction, and there was no magnetic hysteresis or saturation at 77° or 293°K . Apparently the rate at which the crystals cooled, after being removed from contact with the melt, was sufficient to prevent decomposition.

T. B. Reed
R. E. Fahey

B. OXIDIZING POTENTIAL OF SOME LABORATORY GASES

In the preparation of many materials, particularly at elevated temperatures, various gases and mixtures of gases are often used to control the effective oxygen pressure. The partial pressure of O_2 in these gases may be conveniently expressed in terms of pO , a quantity defined by $\text{pO} = -\log p_{\text{O}_2}$, where p_{O_2} is the partial pressure in atmospheres. The pO , which is analogous to pH in solution chemistry, plays an equally important role in oxide chemistry.⁴ In preparing oxides it is necessary to measure and control pO in the range $-4 < \text{pO} < 50$, while for the preparation of metals and other compounds it is usually necessary to keep pO above 20 in order to prevent oxidation. Pressures in the range $-2 < \text{pO} < 6$ can be established directly with gaseous oxygen, and those in the range $16 < \text{pO} < 30$ can be obtained with $\text{H}_2\text{-H}_2\text{O}$ or CO-CO_2 gas mixtures.

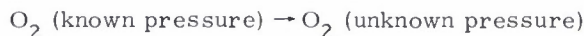
Due to the development of solid state electrolytes, such as yttria-stabilized ZrO_2 or ThO_2 , it is now possible to make direct measurements of the pO of gases by using an electrochemical cell:



The EMF of this cell is related to the pO of the unknown gas by

$$\text{pO} = nFE/2.303 RT + \text{pO (known)} ,$$

where F is the Faraday, E the measured EMF, and n the number of electrons transferred in the reaction



A commercial oxygen meter using stabilized ZrO_2 at 1000°K has been employed to measure the pO of a number of gases subjected to various treatments often encountered in the laboratory. The results are shown in Table III-1. For commercial argon, argon-oxygen and hydrogen, the measured pO values are in good agreement with those calculated from the suppliers' specifications.

Values of pO are given in Table III-1 for commercial argon and hydrogen which had been gettered by passing them over titanium foil or chips heated to about 1000°K in a furnace of the design shown in Fig. III-2. Titanium at this temperature is an effective bulk getter because (a) the maximum partial pressures of O_2 and N_2 in equilibrium with titanium at 1000°K are 10^{-44} and 10^{-24} atm, respectively, and hydrocarbons react to form TiC and hydrogen; (b) oxygen, nitrogen and carbon diffuse rapidly enough through titanium at 1000°K so that the entire mass, rather than just the surface, is available for gettering. The measured pO of gettered argon, 22.1, while not nearly as high as the value of 44 predicted thermodynamically, is satisfactory for most applications. Even to obtain this high a value, it was necessary to use metal tubing between the gettering furnace and the meter, and the tubing had to be flamed or purged for a long time. Significant contamination can occur with plastic tubing, which permits the diffusion of

Section III

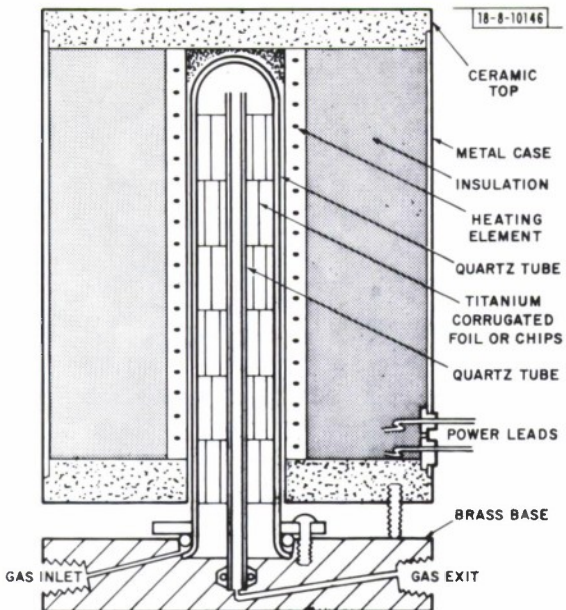


Fig. III-2. Diagram of titanium gettering furnace.

water vapor and oxygen. To measure this effect, the pO of argon was measured after the gettered gas had passed through 6 m of plastic tubing. The values in Table III-1 show that the pO was not greatly reduced at sufficiently high flow rates, but at a flow rate of $150 \text{ cm}^3/\text{min}$ the pO was the same as for argon saturated with water vapor at room temperature.

Hydrogen is extensively used as a reducing agent. Its pO depends on the ratio of water vapor to hydrogen, according to the expression⁵

$$pO = \frac{(119,300 - 27.3T)}{2.303RT} - 2 \log(p_{H_2O}/p_{H_2})$$

The pO value of 22.5, which was measured for hydrogen saturated with water vapor at room temperature, is the same as the value calculated from this expression. By adjusting the ratio of water vapor to hydrogen, it is possible to maintain controlled values of pO over a range much higher than the one which can be obtained with mixtures of oxygen and an inert gas. Since the pO of hydrogen is strongly reduced by even small amounts of moisture, use of titanium gettering or liquid nitrogen trapping to remove the water vapor from commercial hydrogen causes a significant increase in pO . To maintain high pO values, it is necessary to flame the gas lines or purge them for long periods.

The high pO value measured for untreated commercial helium may seem surprising. This might result from the presence of hydrocarbons, such as methane, which are common contaminants of helium and would behave like hydrogen in the zirconia electrolyte of the oxygen meter. Similarly, water vapor in commercial argon would be reduced to hydrogen during titanium gettering, so that the high pO of gettered argon may reflect the presence of hydrogen as well as the absence of oxygen.

T. B. Reed

C. INFLUENCE OF MADELUNG ENERGY AND COVALENCY ON THE STRUCTURE OF $A^+B^{5+}O_3$ COMPOUNDS

Many oxides, fluorides and sulfides of formula ABX_3 , where A and B are cations, crystallize in one of the hexagonal-perovskite polytypes. In the fluoro-perovskites (ABF_3) cation-cation Coulomb repulsive forces are small because the B cations have a relatively small (2^+) charge. Consequently the stability ranges for the polytypes are determined entirely by the ionic radii of the cations.

In the ABO_3 compounds, the stability ranges are not well defined by the ionic radii, since these ranges also depend significantly on the effective charges of the B cations. High-pressure synthesis techniques have been utilized to investigate the factors determining the structures of $A^+B^{5+}O_3$ compounds, for which no hexagonal polytypes have been reported.

The $A^{2+}B^{4+}O_3$ compound $BaTiO_3$ provides a clue to the behavior of the $A^+B^{5+}O_3$ compounds. The Goldschmidt tolerance factor⁶ (t) is 1.06 for $BaTiO_3$. For such a high value of t , because of severe geometric hindrances, the cubic perovskite structure is geometrically less favorable than the hexagonal polytypes. Nevertheless, stoichiometric $BaTiO_3$ is cubic at high temperatures. Unlike the cubic form, the hexagonal structures involve face sharing of BO_6 octahedra, and the cation-cation repulsive forces are strongest across the shared faces. Apparently the effective charge on the Ti^{4+} ions in stoichiometric $BaTiO_3$ is sufficiently high that the loss of Madelung energy due to Ti^{4+} - Ti^{4+} repulsions makes the hexagonal forms less stable than the cubic. For oxygen-deficient $BaTiO_3$, however, the effective charge on the Ti^{4+} ions is reduced, and the hexagonal (6H) form is observed. The hexagonal (9R) polytype is formed by $BaRuO_3$, which has the same tolerance factor as $BaTiO_3$. In this case, the repulsive forces are reduced because Ru^{4+} ions have a much smaller effective charge than Ti^{4+} ions.

In a perovskite whose Goldschmidt factor is much greater than 1.0, there is considerable stretching of the B-O bond. By reducing the elastic restoring forces that would inhibit displacement of the B cation toward one or more near neighbor O ions, this stretching enhances any tendency for ferroelectric distortions. Thus $BaTiO_3$ ($t = 1.06$) is ferroelectric, but $SrTiO_3$ ($t = 0.99$) is not.

Since previous investigations had demonstrated that high pressures tend to stabilize the cubic perovskite phase, the synthesis of some new $A^+B^{5+}O_3$ compounds having large Goldschmidt factors was attempted. $RbNbO_3$ ($t = 1.08$) was synthesized at 65 kbar and 900°C. At atmospheric pressure and room temperature, this compound is an orthorhombic perovskite ($a = 3.9965 \text{ \AA}$, $b = 5.8360 \text{ \AA}$, $c = 5.8698 \text{ \AA}$), isostructural with the ferroelectric orthorhombic form of $BaTiO_3$. Once again ferroelectric distortions are associated with $t > 1$.

The compound $RbTaO_3$ ($t = 1.08$) was synthesized at 90 kbar and 900°C. It forms a cubic perovskite ($a = 4.035 \text{ \AA}$). Apparently the strong octahedral-site preference of the Ta^{5+} ion does not permit a ferroelectric distortion at room temperature, even for such a high value of t .

Synthesis of $RbNbO_3$ and $RbTaO_3$ shows that high-pressure stabilization of B^{5+} perovskites having very high Goldschmidt factors is possible. Heating these compounds, which are metastable at atmospheric pressure, results in their decomposition rather than transformation to a hexagonal structure. Therefore, it is certain that the $A^+B^{5+}O_3$ compounds do not have stable hexagonal polytypes, presumably because the high effective charge on the B^{5+} ions makes the cation-cation repulsion too strong.

Section III

To study the effect of covalency on ABO_3 structures, $\text{A}^+\text{Sb}^{5+}\text{O}_3$ compounds were also investigated, where the B cations have no outer d orbitals and there is strong Sb-O eovalency. Regardless of tolerance factor, no $\text{A}^+\text{Sb}^{5+}\text{O}_3$ perovskite or perovskite polytype has been reported. Several high pressure syntheses were attempted, to see whether a perovskite structure involving $180^\circ \text{Sb}^{5+}-\text{O}-\text{Sb}^{5+}$ bonds could be stabilized.

The compound RbSbO_3 ($t = 1.085$) was synthesized at 20 kbar and 1000°C . It has the $\text{Pn}3$ structure of cubic KSbO_3 ($a = 9.6985 \text{ \AA}$). The compound TlSbO_3 was also synthesized at elevated pressures; it exhibits a distorted form of the $\text{Pn}3$ structure. In this structure, pairs of SbO_6 octahedra share edges, and these pairs are linked at their corners to form a cubic network. The Sb-O-Sb bond angles are 90° and about 130° . Apparently this phase is more stable than the cubic perovskite structure, even though it requires placement of unscreened A^+ ions relatively close to each other within tunnels formed by this network.

It is concluded that $180^\circ \text{Sb}^{5+}-\text{O}-\text{Sb}^{5+}$ bonds are unstable relative to 90° or 120° to $140^\circ \text{Sb}^{5+}-\text{O}-\text{Sb}^{5+}$ bonds. This is presumably due to the stronger eovalency that is possible if the oxygen ions do not use the same p orbital in the formation of two different Sb-O bonds.

J. A. Kafalas

D. STRUCTURE OF $\text{V}_{0.95}\text{Cr}_{0.05}\text{O}_2$

The results of a structure refinement on a compound of nominal composition $\text{V}_{0.95}\text{Cr}_{0.05}\text{O}_2$ were recently reported.⁷ In making this refinement, a face-centered orthorhombic cell⁸ was used to index the diffraction pattern obtained by x-ray intensity measurements on a powdered sample.

An alternative, monoelminic structure for $\text{V}_{0.95}\text{Cr}_{0.05}\text{O}_2$ is suggested by the results of a recent structural investigation of $\text{V}_{0.976}\text{Cr}_{0.024}\text{O}_2$ by Marezio, et al.⁹ On the basis of single crystal diffraction data they identify four crystallographically distinct phases as a function of temperature. The room-temperature modification (designated M2), with unit-cell parameters $a = 9.0664 \text{ \AA}$, $b = 5.7970 \text{ \AA}$, $c = 4.5255 \text{ \AA}$ and $\beta = 91.88^\circ$, is a monoclinic phase whose structure accounts for all the diffraction peaks observed in our powder pattern for $\text{V}_{0.95}\text{Cr}_{0.05}\text{O}_2$.

To study the possibility of deciding between the orthorhombic and monoclinic structures for $\text{V}_{0.95}\text{Cr}_{0.05}\text{O}_2$ by means of powder diffraction experiments, intensity calculations for this composition based on the two structures were compared. The calculated patterns differ significantly only in the character of the peak corresponding to a d-spacing of about 1.33 \AA . For the monoclinic structure, the diffraction envelope in this region is composed of two peaks of approximately equal intensities, the 620 and 023. Their d-spacings of 1.3394 and 1.3376 \AA , respectively, correspond to an angular separation of approximately 0.1° in 2θ for copper radiation. For the orthorhombic structure, there is only a single peak, the 662, whose intensity is approximately equal to the sum of the two monoclinic peaks.

In an attempt to observe the splitting predicted by the monoclinic structure, the powder diffraction of $\text{V}_{0.95}\text{Cr}_{0.05}\text{O}_2$ near 70° was carefully re-measured, using $\text{CuK}\alpha$ radiation and a graphite crystal diffracted-beam monochromator. Figure III-3 reproduces a trace obtained in this region at a diffractometer speed of $1/8^\circ/\text{min}$ and chart speed of $1/2 \text{ inch/min}$. The $\text{K}\alpha_1$ and $\text{K}\alpha_2$ peaks are well resolved. The distance between these peaks, which are separated by about

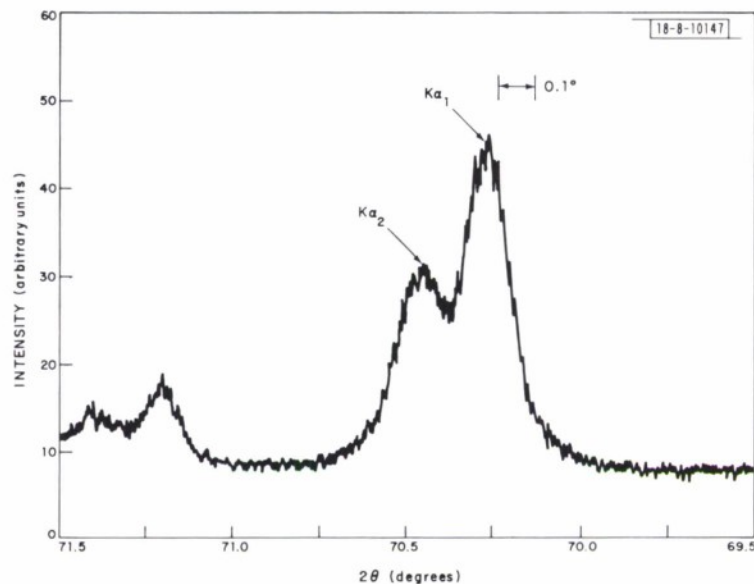


Fig. III-3. Trace of x-ray diffraction pattern near $2\theta = 70^\circ$ for powdered $V_{0.95}Cr_{0.05}O_2$.

0.2° , indicated that it would have been possible to detect a 620-023 splitting of 0.1° , the amount calculated for the monoclinic structure. However, there is no indication of such a splitting, nor is there any apparent anomaly in the shape of the peaks in comparison with others in the pattern. Furthermore Guinier photographs gave no evidence for splitting.

Failure to observe the 620-023 splitting is consistent with the orthorhombic structure proposed for $V_{0.95}Cr_{0.05}O_2$, and is inconsistent with the particular monoclinic structure ($\beta = 91.88^\circ$) established by Marezio, *et al.*, for $V_{0.976}Cr_{0.024}O_2$. However, the magnitude of the splitting approaches zero as β approaches 90° . If this angle were a function of Cr content, it might become small enough at $V_{0.95}Cr_{0.05}O_2$ to be undetectable in powder diffraction experiments. In order to avoid this inherent uncertainty in the powder method, a single crystal study has been undertaken, which should lead to an unambiguous determination of the structure.

J. W. Pierce
J. B. Goodenough

E. EFFECT OF PRESSURE ON THE MAGNETIC BEHAVIOR OF MnP

The ferromagnetic ordering temperature (T_c) of orthorhombic MnP was found to be $291.5^\circ K$ by Huber and Ridgley,¹⁰ who also observed an antiferromagnetic-ferrromagnetic transition at $50^\circ K$ (T_t), below which MnP is metamagnetic. Previous studies^{11,12} on the effect of pressure on the magnetic properties of MnP have been limited to 6 kbar. In the present investigation, measurements have been made on samples subjected to hydrostatic pressures up to 30 kbar and quasi-hydrostatic pressures up to 50 kbar.

Ingots of MnP were prepared by fusion of the elements in a vertical two-zone furnace.¹⁰ To obtain single crystals, the furnace was cooled from the maximum temperature of about $1170^\circ C$ to $1000^\circ C$ at about $2.5^\circ / hr$ and then shut off.

Section III

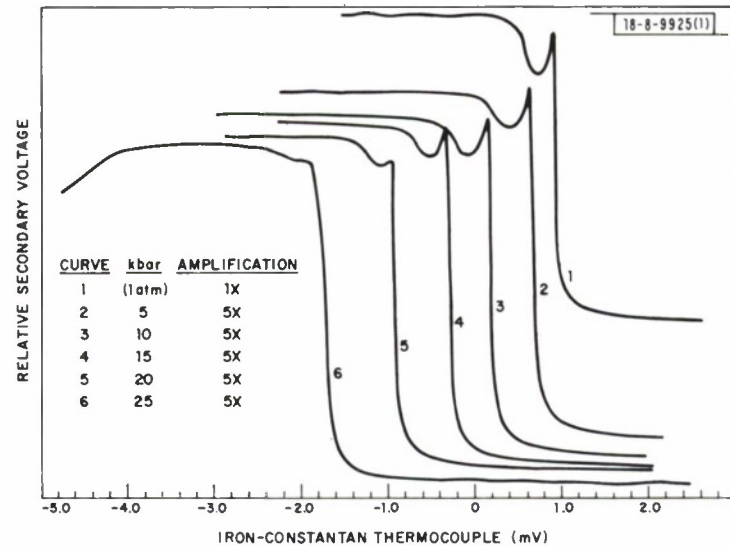


Fig. III-4. Recorder traces of relative secondary voltage vs thermocouple voltage (0°C reference junction) obtained at fixed pressures during cooling of transformer with on unoriented single crystal MnP core.

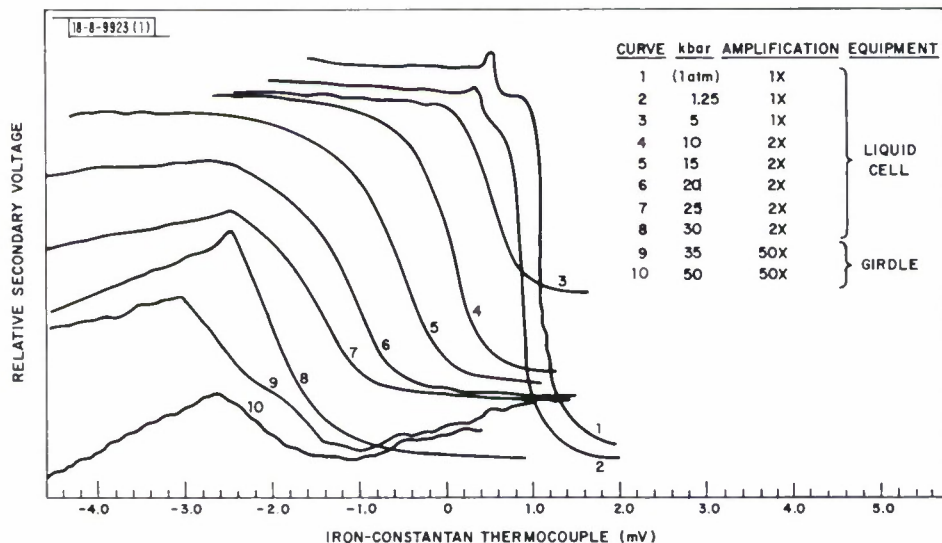


Fig. III-5. Recorder traces of relative secondary voltage vs thermocouple voltage (0°C reference junction) obtained at fixed pressures during cooling of transformer with core cut from powdered MnP-epoxy coating.

An AC method¹³ was used to make the magnetic measurements on washer-shaped specimens, which were bifilar-wound to form the core of a transformer. These specimens were cut either from short rods cast from a mixture of MnP powder dispersed in epoxy cement, from slices of polycrystalline ingot, or from single-crystal ingots. The change with temperature of the initial permeability was observed at a series of fixed pressures by plotting the relative secondary voltage vs thermocouple output on an x-y recorder. Hydrostatic pressure measurements were made in a liquid cell with a mixture of iso-amyl alcohol and pentane. Quasi-hydrostatic pressure measurements were made with a girdle-die¹⁴ using solid AgCl as the pressure transmitting medium. The lowest temperatures which could be attained were in the range 150 to 170°K, not low enough to follow the metamagnetic transition temperature.

Typical recorder plots of relative secondary voltage vs thermocouple voltage for transformers with MnP cores are reproduced in Figs. III-4 and III-5. The data in Fig. III-4 were obtained for a single crystal core in the liquid cell at pressures up to 25 kbar. Those in Fig. III-5 were obtained with a core cut from a powdered MnP-epoxy casting, measured in the liquid cell up to 30 kbar and in the girdle-die at 35 and 50 kbar. For both cores there is a strong increase in secondary voltage when the sample is cooled through T_c , although the slope at the transition becomes considerably less steep for the powder-epoxy core with increasing pressure. The small peaks in the curves for the powder-epoxy core observed just below T_c at the lowest pressures are due to the magnetic anisotropy of MnP. These peaks show that some preferred orientation of the MnP powder particles must have occurred during their dispersion and casting in epoxy cement at room temperature.

The T_c values determined from the secondary voltage curves are plotted against pressure in Fig. III-6. For the powder-epoxy cores, the temperature at the midpoint of the change in secondary voltage was taken as T_c . For the single crystal cores, the temperature of the sharp peak was taken as T_c . Up to 20 to 25 kbar, the T_c values for the two types of samples and for measurements in the liquid cell and in the girdle-die are in excellent agreement.

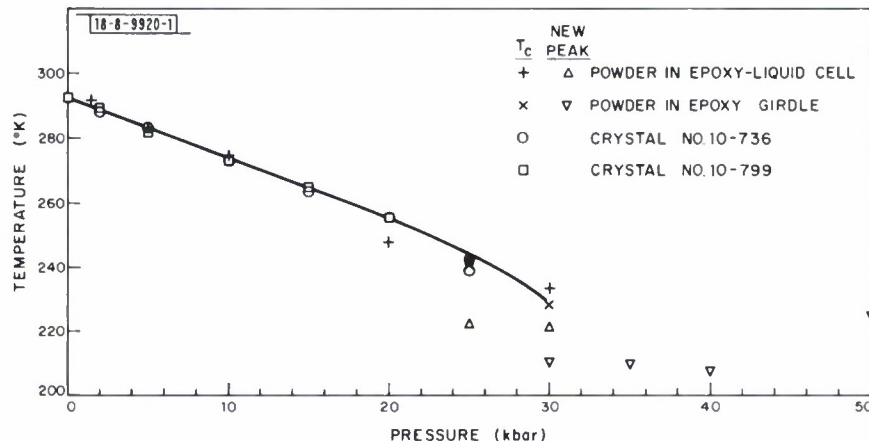


Fig. III-6. Magnetic ordering temperature (T_c) of MnP as a function of pressure. For 25 and 30 kbar, the temperature at the peak of the secondary voltage vs thermocouple voltage curve is plotted as well as T_c . At higher pressures, only the peak temperature is shown.

Section III

Up to about 20 kbar, T_c decreases linearly with increasing pressure, at the rate of $-1.85^\circ\text{K}/\text{kbar}$. Kamigaichi, *et al.*,¹² obtained $\Delta T_c/\Delta P = -1.5^\circ\text{K}/\text{kbar}$ by means of electrical resistivity measurements extending only to 6 kbar. Between 20 and 30 kbar, T_c decreases somewhat more rapidly with increasing pressure. However, the significance of the T_e values in this region is uncertain, since the shape of the secondary voltage curves (Fig. III-5) changes markedly, with the secondary voltage reaching a maximum and then decreasing as the sample is cooled. For 25 and 30 kbar, both T_e and the temperature at the peak of the curve are plotted in Fig. III-6. Only the peak temperature is plotted for higher pressures, since the temperature at the midpoint of the secondary voltage rise is clearly no longer meaningful. The peak temperature is essentially constant between 30 and 40 kbar, but increases significantly at 50 kbar. (The apparent decrease in peak temperature between 25 and 35 kbar in Fig. III-6 results because the peak temperatures measured with the liquid cell were about 10°K higher than those measured with the girdle-die unit at the same pressure.)

The change in the character of the secondary voltage curves and in the pressure dependence of the transition temperature between 25 and 35 kbar strongly suggests that a ferromagnetic to antiferromagnetic transition occurs in this pressure region. This transition might conceivably be due to the pressure stabilization of the low-temperature metamagnetic phase of MnP relative to the ferromagnetic phase. However, this explanation seems unacceptable because Kamigaichi, *et al.*,¹² found that the transition temperature T_t decreased by 6°K between 1 atm and 5 kbar, and because Menyuk¹⁵ failed to observe a transition to the antiferromagnetic phase down to 57°K at 9 kbar.

Goodenough¹⁶ has argued that at lowest temperatures a compound having a partially filled narrowband may undergo transformation, with increasing bandwidth, from spontaneous ferromagnetism to a ferromagnetic-spiral to an antiferromagnetic spin-density wave to Pauli paramagnetism. In MnP and MnAs, the orthorhombic structure is associated with low-spin manganese ions, and the spontaneous ferromagnetism appears to be itinerant-electron, rather than localized-electron, ferromagnetism. Furthermore, the fact that FeP has an antiferromagnetic spin-density wave suggests that transformation from a ferromagnetic to an antiferromagnetic state may be induced in MnP with a relatively small increase in bandwidth. Since the widths of the occupied 3d bands of MnP are sensitive to the Mn-Mn interactions (not the Mn-P-Mn interactions), the relevant bandwidths may increase sensitively with hydrostatic pressure. Therefore, a ferromagnetic-to-antiferromagnetic transition due to increasing bandwidth, as discussed by Goodenough¹⁷ for the system $\text{CoS}_{2-x}\text{Se}_x$, seems to be a satisfactory explanation for the changes that have been observed in the magnetic behavior of MnP between 25 and 35 kbar.

M. D. Banus

REFERENCES

1. P. Vallet and P. Raccah, Compt. Rend. 258, 3679 (1964).
2. J. Burmeister, Mat. Res. Bull. 1, 17 (1966).
3. T. B. Reed and E. R. Pollard, J. Cryst. Growth 2, 243 (1968), DDC AD-681586.
4. T. B. Reed in The Chemistry of Extended Defects in Non-metallic Solids (North-Holland, Amsterdam, 1970), p. 21.
5. T. B. Reed, Free Energy of Formation of Binary Compounds (M. I. T. Press, Cambridge, 1971).
6. V. M. Goldschmidt, Akad. Oslo 1. Mat.-Natur. 2, 7 (1926).
7. Solid State Research Report, Lincoln Laboratory, M. I. T. (1971:2), p. 19, DDC AD-732923.
8. B. Chamberland, personal communication.
9. M. Marezio, D. B. McWhan, J. P. Remeika and P. D. Dernier, Europhysics Conference on "Metal Insulator Transition and the Development of Narrow Energy Bands," Aussois, Savoie, France, 6-10 September 1971.
10. E. E. Huber, Jr. and D. H. Ridgley, Phys. Rev. 135A, 1033 (1964).
11. E. Hirahara, T. Suzuki and Y. Matsumura, J. Appl. Phys. 39, 713 (1968).
12. T. Kamigaichi, T. Okamoto, N. Iwata and E. Tatsumoto, J. Phys. Soc. Japan 24, 649 (1968).
13. D. B. McWhan and A. L. Stevens, Phys. Rev. 139A, 682 (1965).
14. H. D. Stromberg and D. R. Stevens, J. Phys. Chem. Solids 25, 1015 (1964).
15. N. Menyuk, personal communication.
16. J. B. Goodenough in Progress in Solid State Chemistry, H. Reiss, Ed. (Pergamon Press, Oxford, 1971), Chap. 4.
17. J. B. Goodenough, J. Solid State Chem. 3, 26 (1971), DDC AD-728185.

IV. PHYSICS OF SOLIDS

A. SECONDARY ELECTRON EMISSION

A study of secondary-electron emission in solids has been initiated. The approach taken involves a systematic correlation of the secondary-electron emission with the electron band structure. Initial studies are aimed at classes of materials with high secondary yields[†] at low primary electron energies. One of the motivations for this program is the need for a more efficient cold cathode for use in a low-input-power, S-band, crossed-field amplifier tube (CFA).

In order for a material to be a good secondary-electron emitter, the hot electrons created by the incident electron must be able to reach the surface with sufficient energy to overcome the vacuum barrier. Since electron-electron scattering is a strong loss mechanism for the hot electrons, there should be as few conduction electrons in the material as possible. On the other hand, if the material were a very good insulator, its surface would charge up under electron bombardment, making it useless for a cold cathode. Therefore, classes of materials that are fairly good insulators and that have sufficient conductivity to eliminate surface charging are under investigation.

Two parameters that are important for yields are the energy gap E_g and the electron affinity χ . Hot electrons can lose energy even in insulators by creating electron-hole pairs. This mechanism is no longer effective after the hot electrons have dropped to within about E_g of the bottom of the conduction band. Below this energy they can interact only with excitations such as phonons. Once the electrons reach the surface, they must overcome the surface barrier (electron affinity). Thus, roughly, χ/E_g must be less than unity for escape.

One of the materials under investigation is dense arc-melted NiO doped with lithium. The lithium goes in substitutionally, creating Li^+ acceptor states 0.4 eV above the filled $3d^8$ manifold of the Ni^{2+} ions, as shown in Fig. IV-1. These levels give rise to p-type conductivity, which can be varied by altering the lithium doping. The secondary emission yield has been measured as a function of primary-electron energy for a sample with nominally one percent lithium doping. The results are shown in Fig. IV-2, along with a published yield curve for platinum,² the material currently used in most CFA tubes. Due to the inhomogeneity of the sample, the exact doping is not known; different areas of the sample give slightly different yield curves. Some conclusions can still be drawn, however. The energy

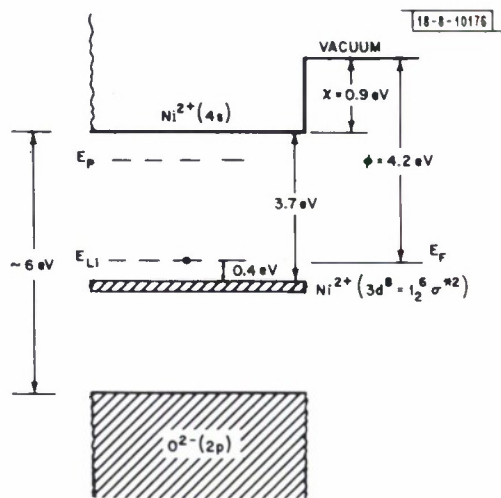


Fig. IV-1. Energy band structure of NiO.
The diagram shows the electronic structure of NiO in a vacuum environment. At the top, the vacuum level is indicated with a value of 0. The Fermi level (E_F) is shown as a horizontal line. The conduction band ($3d^8 - 1s^2$) is at an energy of 3.7 eV above the Fermi level. The valence band ($\text{Ni}^{2+}(4s)$) is at an energy of 4.2 eV above the Fermi level. The electron affinity (χ) is 0.9 eV. The energy gap (E_g) is approximately 6 eV. The primary electron energy (E_p) is indicated as ~6 eV. The lithium acceptor level (E_{Li}) is shown as a horizontal line at an energy of 0.4 eV above the valence band. The diagram is labeled with the code 18-8-10176 in the top right corner.

[†]The yield is defined as the number of secondary electrons emitted per incident electron. For further secondary-electron emission terminology see Ref.1.

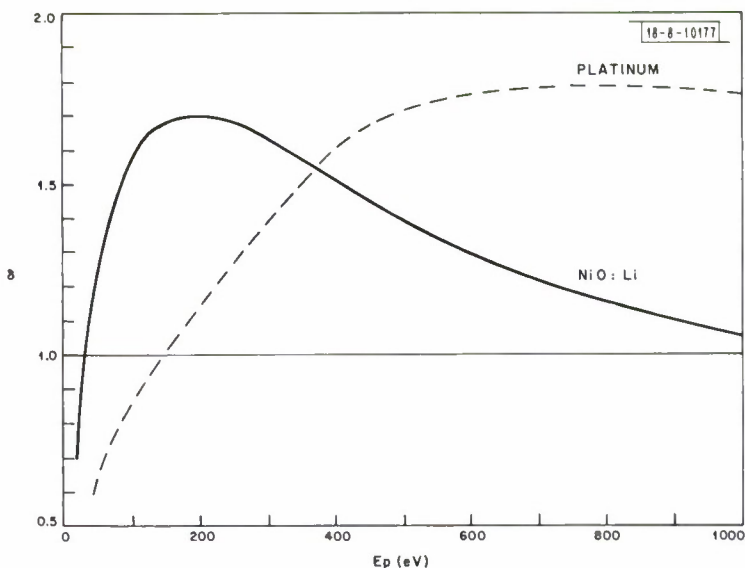


Fig. IV-2. Yield vs incident electron energy for NiO:Li^+ (solid line) and platinum (dashed line).

at which the yield equals one, known as the crossover point, is several times lower than that for platinum. Thus the NiO:Li^+ system has met one of the requirements for low-power CFA use; other relevant properties are now being examined.

The work function of the sample has also been measured by the Kelvin method. A value of 4.2 eV was obtained. Taking the energies as shown in Fig. IV-1 and assuming that the Fermi level is pinned near the Li^+ acceptors gives an electron affinity of about 0.9 eV. Thus, χ/E_g is 0.24, easily satisfying the escape criterion mentioned above.

V. E. Henrich J. G. Mavroides J. A. Kafalas	T. B. Reed J. B. Goodenough
---	--------------------------------

B. PHOSPHOR UPCONVERSION

1. Rare Earth Phosphors for Near-Infrared to Visible Upconversion

A fluorescence spectrometer has been constructed in order to study the conversion of radiation from the near-infrared ($\sim 0.98 \mu\text{m}$) to the visible ($\sim 0.54 \mu\text{m}$) spectrum by rare earths in hosts having the gagarinite structure. The samples were prepared by weighing commercially available rare-earth and sodium fluorides to give a nominal composition with a cation-to-anion ratio approaching that of the natural gagarinite $(\text{Na, Ca, Y})_{2.8}\text{F}_6$. The samples were then fired for 16 to 24 hours at 1000°C under flowing, scrubbed argon gas and cooled at the natural rate of the furnace.

Initial investigations have concentrated on the composition $\text{Na}_{1.44}\text{Y}_{1.30}\text{Yb}_{0.28}\text{Er}_{0.02}\text{F}_{6.4}$ prepared in the above manner. Before attempting to optimize the ytterbium and erbium content, it is necessary to achieve consistent relative efficiency results with a single composition. This requirement has not yet been met. However, samples with relatively low efficiency have been found by x-ray analysis to contain rare-earth oxyfluoride. Efforts are therefore under way to further exclude oxygen from the system in use. In addition, high purity (99.999 percent)

rare-earth oxides are now being used as starting material for the preparation of the rare-earth fluorides in an effort to eliminate detrimental effects due to impurities other than oxygen.

The most efficient sample tested for conversion from infrared to green radiation has an efficiency comparable with that of YF_3 :Yb, Er, which is the most efficient infrared-to-green up-converter listed in the literature.³ Since, as noted above, neither the ytterbium nor erbium content has been optimized in the gagarinite system, it is believed to be potentially the most efficient phosphor to date for near-infrared-to-green upconversion.

J. W. Pierce
N. Menyuk
K. Dwight

2. Infrared Stimulation of Visible Luminescence in ZnS Phosphors

A useful phenomenon in the field of infrared detection is the infrared stimulability of visible luminescence in certain ZnS phosphors, such as ZnS:Cu, Al. The phosphor must first be excited with ultraviolet light, which causes visible luminescence. The further application of infrared of about 2 to 20 μm induces additional visible luminescence if the sample is at a sufficiently low temperature, perhaps less than 20° K. This is the first report on a program to study this phenomenon. The intent of the program is to achieve a sufficient degree of understanding to allow some optimization of the infrared stimulability of such phosphors.

Because the infrared stimulated visible luminescence has very nearly the same spectral character as the ultraviolet induced luminescence, an understanding of the stimulation phenomena divides naturally into two parts; (a) the luminescence mechanism and (b) the stimulation mechanism. Luminescence in ZnS occurs because of the intentional or accidental presence of impurities in the crystal. The characteristics of the luminescence depend greatly on what the impurities are. In the case of ZnS:Cu, Al, which will be discussed here and is one of the infrared stimulable phosphors, there is considerable evidence⁴ that the luminescence occurs from direct transitions of electrons trapped on shallow hydrogen-like Al donor levels, to deep Cu acceptor states with trapped holes. The transition probability for this process depends on the donor-acceptor pair separation r approximately as $W(r) = W_0 \exp(-r/a_0)$, where a_0 is half the hydrogenic radius of the aluminum donor ground state. The energy E of the emitted photon is given by the difference in energies of the donor and acceptor levels in the ZnS gap plus an interaction term $e^2/\epsilon r$, where ϵ is the dielectric constant. This type of luminescence is characterized by long decay times (after cessation of ultraviolet pumping) at low temperatures, due to trapped hole-electron pairs with large r and small W ; a red shift during decay because the small r , large W , large E pairs decay first; and a blue shift with increased steady ultraviolet pump intensity, because the large r , small W , small E pairs are easily saturated.

Several experiments on the infrared stimulation effect in a ZnS:Cu, Al crystal have been carried out under conditions of steady ultraviolet pumping, in contrast to experiments of other workers⁵ which have been made during the long decay period after cessation of ultraviolet pumping. For reasons to be given below, it is significant that the time response to infrared stimulation with steady ultraviolet pumping is similar to that during decay; namely, that when the infrared is abruptly turned on there is a transient burst of additional visible luminescence and rapid decay back to the no-infrared level, even though the infrared is kept on. It is also found that the burst of luminescence is slightly blue-shifted relative to that induced by the steady

Section IV

ultraviolet pumping. The experimental arrangement used is superior in some respects to previous ones through the use of a Group 85 produced laser diode as the infrared stimulation source, rather than a globar and spectrometer. Both the diode and the sample are enclosed in a copper can having a window that blocks infrared and passes ultraviolet and visible. The can is immersed in liquid helium. Thereby the sample is completely protected from being stimulated by unwanted thermal infrared radiation. The fast time response of the diode allows great freedom in studying the time response of the stimulation effect to various infrared pulse forms. The principal disadvantage is that experiments must be conducted at a single stimulation wavelength, presently 9 μm , although the use of other wavelength diodes is planned.

Other workers,⁵ in suggesting stimulation mechanisms, have considered that the only role the conduction band might play is as an initial state for the luminescence, and since the luminescence has the properties of donor-acceptor pair emission, the conduction band has been assumed to play no role. Rather it has been presumed that the infrared somehow affects $W(r)$, and that the transient nature of the response to stimulation during decay represents the depletion of the trapped electrons affected by the infrared. However, such a model is inconsistent with the observed transient response during steady ultraviolet pumping, since there the traps are constantly being replenished. This leads to a search for a model in which there is no additional infrared induced luminescence under conditions of steady ultraviolet and infrared excitation. Such a model is as follows: the ultraviolet lifts electrons off the Cu acceptors, putting them into the conduction band, and leaving trapped holes behind; the conduction electrons fall into aluminum traps and subsequently recombine radiatively with the trapped holes. With steady-state ultraviolet pumping, and no infrared, the distribution of trap occupation will be such that traps close to Cu acceptors (small r) decay immediately and are almost always empty, while traps far from a Cu acceptor (large r) decay very slowly and are almost always occupied. The infrared lifts electrons from the occupied (large r) traps into the conduction band, from which they fall preferentially into unoccupied (small r) traps, causing an increase in luminescence and a blue shift. But the increase must be transient, since all the energy supplied by the infrared is presumed to be dissipated again in the retrapping process. It should be pointed out that the assumption that the infrared lifts electrons into the conduction band is consistent with the known depth of the aluminum donor level.

The preceding model, illustrated in Fig. IV-3, is readily formulated in terms of the coupled rate equations

$$\frac{dM(t)}{dt} = I_{uv} A + BI_{ir} n_D \int dr \rho(r) Q(r, t) - TM(t) n_D \int dr \rho(r) [1 - Q(r, t)]$$

$$\frac{d}{dt} [n_D \rho(r) Q(r, t)] = Tn_D \rho(r) [1 - Q(r, t)] M(t) - BI_{ir} n_D \rho(r) Q(r, t) - n_D \rho(r) W(r) Q(r, t)$$

where n_D is the total number of donors, $\rho(r)$ is the probability that the nearest acceptor to a donor is a distance r away, $Q(r, t)$ is the probability that a donor of type r is occupied at time t , M is the conduction band population, I_{uv} is the ultraviolet pump intensity, I_{ir} is the infrared

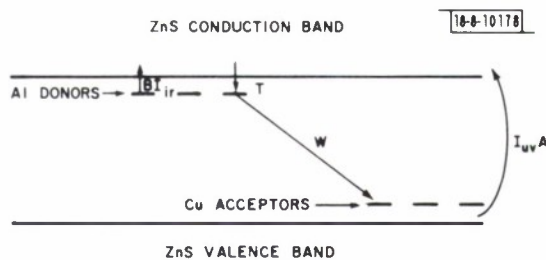


Fig. IV-3. Illustration of model for infrared stimulation of visible luminescence in ZnS:Cu, Al.

stimulation intensity, and A, B, and T characterize the response to ultraviolet, the response to infrared and the donor trapping probability, respectively. It is easily shown that at steady state (denoted by an over bar) the total luminescence output, $\bar{n}_D \int dr \rho(r) W(r) \bar{Q}(r)$ equals $\bar{I}_{uv} A$, as anticipated. These equations are quite susceptible to computer solution and this work is presently being done. The results will be compared with the experiments described above.

A second phase of the program is the preparation and testing for infrared stimulability of other phosphors. To date, the following stimulable phosphors have been made: ZnS:Na, Cl; ZnS:Cu, Cl; ZnS:Cu, Ga; ZnS:Al and ZnS:Cl. In addition, a number of phosphors that are not stimulable have been prepared. As this part of the program proceeds further, the results will be correlated with the above model and detailed measurements will be made on promising phosphors.

J. W. Allen
G. W. Iseler

C. METAL-INSULATOR TRANSITIONS

A preliminary study is under way, of possible device applications making use of electronic switching of materials with metal-insulator transitions. Since applications will require thin films of these materials, a program to grow films has been initiated. A theoretical model of electronic switching near the metal-insulator transition has been formulated.

1. Material Preparation and Characterization

The electrical and optical properties of the oxides of vanadium are extremely sensitive to the vanadium oxygen ratio (x in VO_x). Figure IV-4 shows the equilibrium oxygen and vanadium pressure over a number of vanadium compounds calculated from the thermodynamic data on the vanadium oxides.⁶ The oxygen pressure determines both the structural compound that is formed and the deviation from the ideal composition within that structure, and can be used to control the properties of the films by annealing in appropriate atmospheres.

Films of titanium and vanadium oxides 2500 to 20,000 Å thick have been made by evaporation of Ti_3O_5 and V_2O_3 single crystals onto glass substrates. The exact composition of the films has not yet been determined. However, they show excellent adhesion and resistivities between 10^3 and 10^6 ohms/sq. (The congruently subliming titanium oxide is reported to be Ti_3O_5 , while V_2O_3 was calculated as the congruently subliming composition for the vanadium oxides.) The resulting films have been examined by electron diffraction and are amorphous as deposited, but become crystalline on annealing at 500° C for four hours. Optical and electrical characterization of the films is under way.

T. B. Reed

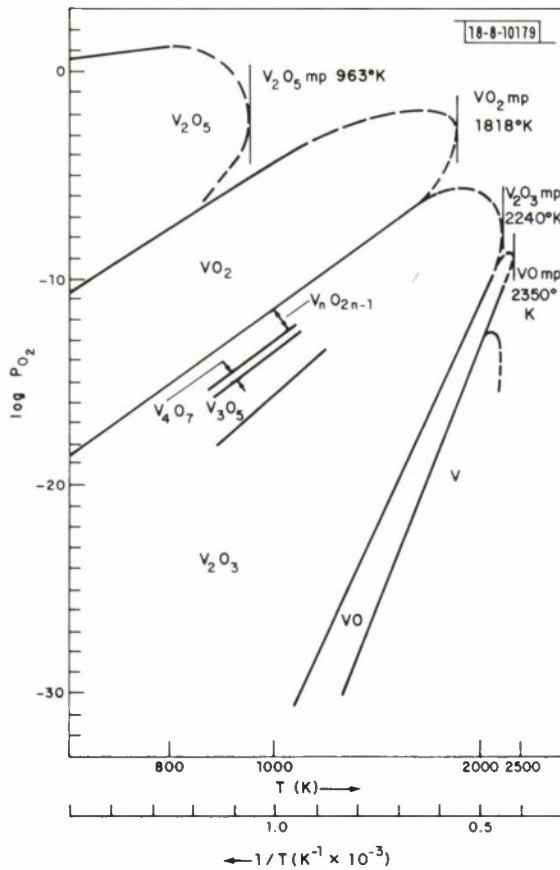


Fig. IV-4. Temperature-pressure phase diagram of the vanadium-oxygen system. Solid lines calculated from thermodynamic data; dashed lines schematic.

2. Model of Electronic Switching

A theoretical model of electronic switching near the metal-insulator transition has been formulated. The model thus far is an extension of an earlier equilibrium thermodynamic one, which was applied to Ti_2O_3 (see Ref. 7). In the equilibrium Hartree-Fock model, the Helmholtz free energy of the system is

$$\mathcal{F}(\delta, r, \tau) = \frac{1}{2\kappa} \delta^2 + \frac{ur^2}{2} - \frac{\tau}{2N} \left\{ \int \rho_2(\epsilon) \ln[1 + e^{(\mu' - \epsilon)/\tau}] d\epsilon + \int \rho_1(\epsilon) \ln[1 + e^{(-\mu' - \epsilon - \Delta)/\tau}] d\epsilon \right\} . \quad (1)$$

In Eq. (1), $\rho_2(\epsilon)$ and $\rho_1(\epsilon)$ are the densities of electron states in an upper band 2 and lower band 1. τ , ϵ and μ' are respectively, temperature, energy and Fermi energy, all normalized to a gap at absolute zero. δ is a normalized number of electrons in band 2 and r is a normalized lattice displacement parameter. The normalized energy gap Δ is given by $\Delta = vr^2 - er + 1 - \delta$; κ , u , v and e are parameters of the model; and N is the number of unit cells in the system. The equilibrium values of μ' , δ and r are determined by the conditions

$$\frac{\partial \mathcal{F}}{\partial r} = 0 , \quad (2)$$

subject to the constraints

$$\delta = \frac{\kappa}{2N} \int \rho_2(\epsilon) [1 + e^{-(\mu' - \epsilon)/\tau}]^{-1} d\epsilon \quad , \quad (3)$$

$$\int \rho_2(\epsilon) [1 + e^{-(\mu' - \epsilon)/\tau}]^{-1} d\epsilon = \int \rho_1(\epsilon) [1 + e^{(\mu' + \epsilon + \Delta)/\tau}]^{-1} d\epsilon \quad . \quad (4)$$

Equations (3) and (4) are respectively the requirement of Fermi-Dirac statistics and conservation of number of electrons. With the appropriate choice of parameters, this model can describe either a "soft" transition with increasing temperature of the kind observed in Ti_2O_3 , or a first order transition with increasing temperature.

This model has been extended to the description of electronic switching by carrier injection (either with a current pulse or a light pulse). If the parameters and the temperature are chosen so that the system is just below the temperature for a first order transition, the effect of an increase in the number of electrons in band 2 may be examined, assuming the temperature is held fixed. This effect can be introduced into the model by imagining μ' disturbed from its equilibrium value, with separate quasi-Fermi levels for bands 1 and 2, μ'_1 and μ'_2 . For a given choice of μ'_2 , the Eqs. (2), (3) and (4), (appropriately modified by the introduction of μ'_1 and μ'_2) can be solved for new values of μ'_2 , δ and r . Such a calculation is now being programmed.

Since the transition in Ti_2O_3 is insulator \rightarrow metal with increasing temperature, while the high temperature transition in V_2O_3 is metal \rightarrow insulator with increasing temperature, the theory will not be applicable to the latter case. A further modification of the basic model to apply to V_2O_3 is under way.

H. J. Zeiger

D. HIGH RESOLUTION LASER SPECTROSCOPY

1. Pressure-Induced Line Shift and Broadening in the Vibration-Rotation Spectrum of CO

Previous high resolution studies^{8,9} of the carbon monoxide fundamental vibration-rotation absorption band were made at low gas pressures (< 1 torr). Now some preliminary measurements have been made at high pressures (> 100 torr) in order to obtain the pressure-induced shift in the center and broadening of the P(9) absorption line of CO. A $PbS_{0.82}Se_{0.18}$ semiconductor diode laser was mounted on the cold finger of a liquid helium dewar and current tuned through the P(9) line at 2107.4 cm^{-1} . A derivative spectrum was obtained by modulating the diode current at 300 Hz and synchronously detecting the transmission through a gas cell. The zero crossing of the derivative signal gives the line center position. The low pressure line center position was obtained by measuring the derivative of the transmission through a cell of 10 cm length filled with 0.05-torr CO. The high pressure line center was obtained using a cell of 0.5 mm length and CO pressures of 100 and 200 torr. The laser tuning rate of 66 MHz/mA was obtained by matching the observed and calculated Doppler widths of the absorption line of the low pressure gas. The line shifts were small, but systematic. Averaging over several experimental runs, the shift was found to be $\lesssim -0.25\text{ MHz/torr}$. Simultaneously, the full width at half intensity of P(9) at 100 torr was found to be 550 MHz, indicating that the pressure (collision) broadening is about 5 MHz/torr.

Section IV

These Lincoln measurements are the first on self-induced pressure shifts and broadening in the fundamental band of CO and are of interest in the design of high pressure, high power CO lasers. Previous studies of pressure-induced line shifts in CO have been restricted to the observation of shifts due to foreign gases such as argon.¹⁰ Self-induced pressure broadening has only been measured¹¹ in the first overtone ($v = 0 \rightarrow v = 2$) band of CO. The pressure broadening observed by Hunt, *et al.*,¹¹ for the P(9) line of the first overtone was 5.1 MHz/torr.

A more detailed study, including measurements of the J -dependence of the pressure shift, is planned.

2. Observation of Zeeman Splitting and Lambda Doubling in NO

The high resolution infrared study⁹ of the absorption spectrum of nitric oxide (NO) has been extended to include a quantitative measurement of Zeeman splitting and Lambda doubling of the R(15/2)_{1/2, 3/2} absorption lines. A CW tunable Pb_{0.62}SSe_{0.38} diode laser⁸ emitted 20 μ W in a laser mode at 1903 cm^{-1} which was current (temperature) tuned through the absorption lines. This narrow line (~ 1 MHz) tunable source provides a resolution of $\sim 5 \times 10^7$ and yields absorption spectra which are fully resolved, limited only by the Doppler width of the low pressure gas. Calibration of the laser tuning rate was performed using a confocal Fabry-Perot interferometer described elsewhere. (See Sec. I-G.) The mode being used for these experiments tuned with diode current at a rate of approximately 900 MHz/mA.

Figure IV-5(a) shows the Λ -doublet absorption profile of the $R(15/2)_{1/2}$ line obtained by measuring the transmission through a 10-cm gas cell with 0.2 torr of NO at 300°K. Note the full resolution of the Doppler absorption profiles and the line splitting due to Λ -doubling. The center of this doublet is known¹² to lie at $1903.131 \pm 0.004 \text{ cm}^{-1}$. At this pressure the additional broadening due to collisions is less than 1 MHz and the absorption coefficient has the Gaussian-Doppler profile.¹³ Hence, the full width at half absorption coefficient of the Doppler broadened line DW, the line intensity S and the frequency splitting due to Λ -doubling E_{Λ} can be measured independently. For this $R(15/2)_{1/2}$ line, $DW = 128 \text{ MHz}$ and $E_{\Lambda} = 318 \text{ MHz}$. The line center absorption coefficient is $\alpha_0 = 0.37 \text{ cm}^{-1}/\text{torr}$, giving $S = 128 \text{ cm}^{-2}/\text{atm}$. The calculated width is $DW = 129 \text{ MHz}$. The line intensity measured at high pressures by Abels and Shaw¹³ is $S = 147 \text{ cm}^{-2}/\text{atm}$. Using the Λ -doubling parameters measured by Gallagher and Johnson¹⁴ in the microwave range and the expressions¹² for the J-dependence of E_{Λ} , $E_{\Lambda} = 324 \text{ MHz}$ is calculated for $R(15/2)_{1/2}$. The difference between the measured and calculated values of E_{Λ} is within experimental error, indicating there is no significant vibrational dependence of the Λ -doubling parameters and no unexpected J-dependence. Note that J is the total angular momentum of the molecule, excluding nuclear spin.

Figure IV-5(b) shows the absorption profile of the $R(15/2)_{3/2}$ line in the $^2\Pi_{3/2}$ sub-band. The calculated Λ -doubling is an order of magnitude smaller, $E_\Lambda = 29$ MHz, and is not resolved due to the 129-MHz Doppler width. This 29-MHz splitting increases the calculated line width to 136 MHz, as compared with the measured width of 140 MHz. The line center absorption

[†] Air Force Cambridge Research Laboratories, Bedford, Mass.

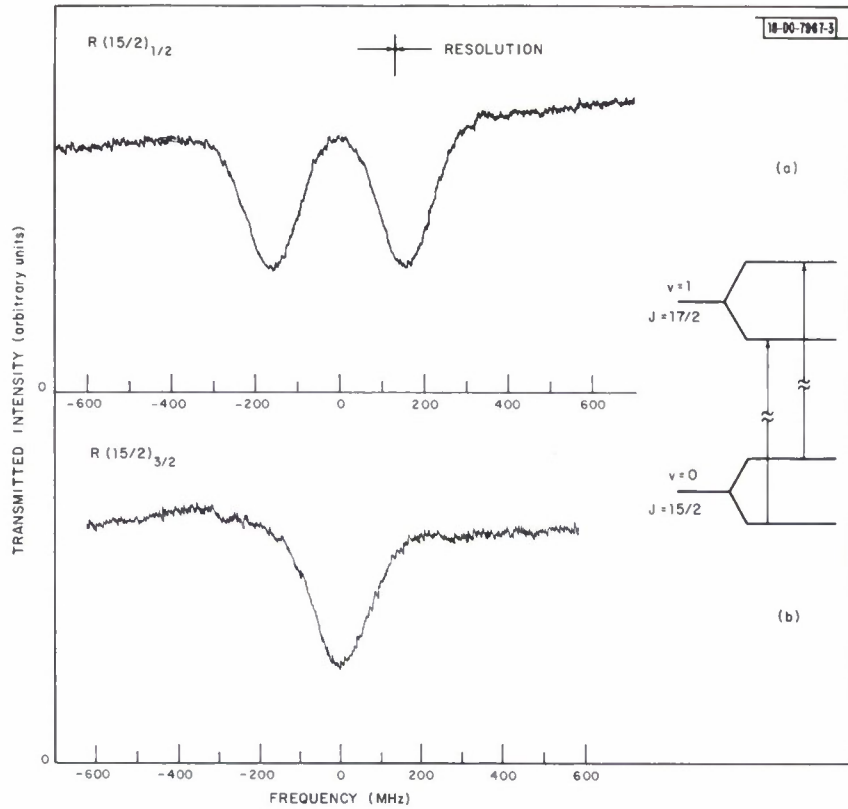


Fig. IV-5. Transmission vs frequency through a 10-cm cell of NO at 0.2 torr for (a) the R(15/2)_{1/2} line and (b) the R(15/2)_{3/2} line. The energy level diagram at the right shows schematically the Δ -type doubling and the transitions involved.

coefficient is $\alpha_0 = 0.42 \text{ cm}^{-1}/\text{torr}$, giving a measured line intensity of $S = 1.47 \text{ cm}^{-2}/\text{atm}$. Abels and Shaw¹³ found $S = 1.61 \text{ cm}^{-2}/\text{atm}$. The R(15/2)_{3/2} line is known¹² to lie at $1903.642 \pm 0.004 \text{ cm}^{-1}$. The data of Figs. IV-5(a) and (b) were taken with the same laser mode and the R(15/2)_{3/2} line was found to lie 0.53 cm^{-1} above the R(15/2)_{1/2} line. This compares well with the separation of 0.51 cm^{-1} given by Keck and Hause.¹²

NO is a strongly paramagnetic gas in both the $^2\Pi_{1/2}$ and $^2\Pi_{3/2}$ states. For weak magnetic fields, the Zeeman splitting of the NO rotational energy levels is given by

$$W = g_J \beta B M_J \quad , \quad (5)$$

where β is the Bohr magneton, M_J is the component of \vec{J} along the magnetic field \vec{B} , and g_J is the g-factor calculated by Dousmanis, *et al.*¹⁵ This splitting of the rotational levels produces a complex Zeeman profile in the R(15)_{1/2, 3/2} absorption lines.

An actual Zeeman derivative trace for R(15/2)_{1/2} is shown in Fig. IV-6(b) for a magnetic field of 31.4 kG applied to the gas. The data were taken with the radiation propagating along \vec{B} , passing through a 4-cm absorption cell. The derivative spectrum was produced by frequency modulating the diode at 300 Hz and synchronously detecting the modulated transmission of the gas cell. Note that each component of the Δ -doublet has split into two Zeeman components. This is as expected, since the electric dipole selection rule $\Delta M_J = \pm 1$ for radiation polarized

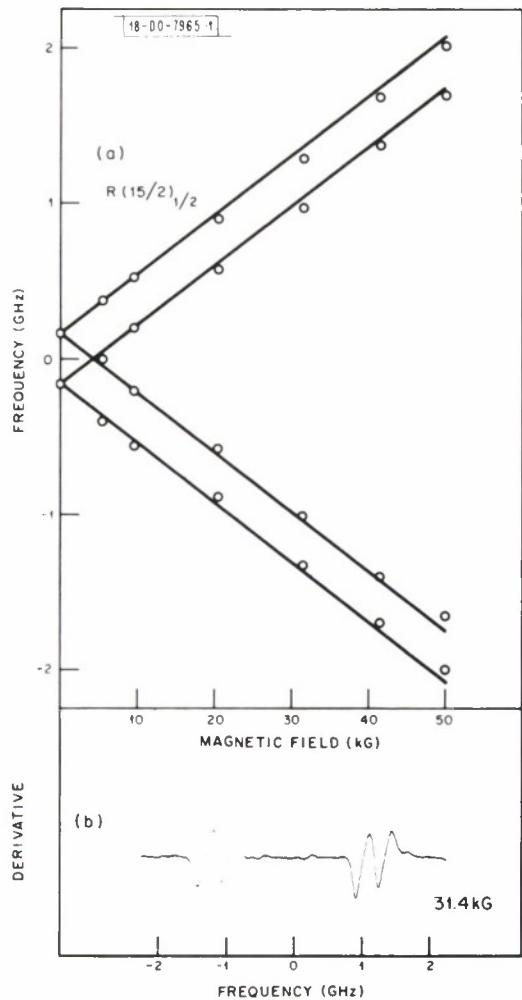


Fig. IV-6. Far $R(15/2)_{1/2}$: (a) Zeeman line frequencies vs magnetic field given by experiment (open circles) and linear Zeeman theory (solid lines); (b) recorder trace of a Zeeman derivative spectrum at 31.4 kG. Data taken with a 4-cm cell containing 1.5-tarr NO at 300°K.

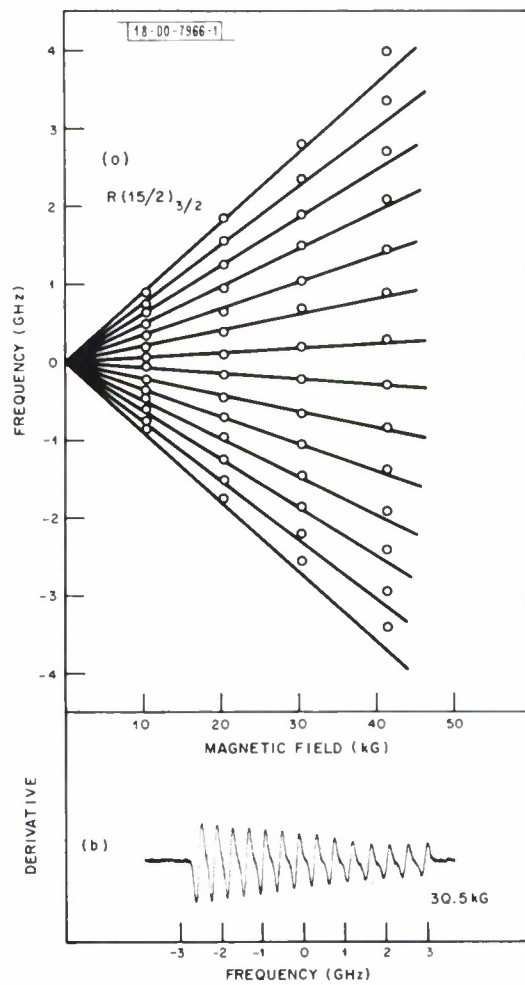


Fig. IV-7. Far $R(15/2)_{3/2}$: (a) Zeeman line frequencies vs magnetic field given by experiment (open circles) and linear Zeeman theory (solid lines); (b) recorder trace of a Zeeman derivative spectrum at 30.5 kG. Data taken with a 4-cm cell containing 1.5-tarr NO at 300°K.

perpendicular to \vec{B} and g_J is nearly independent of J (for $J > 3/2$) for the $^2\Pi_{1/2}$ electronic levels. As a result, the Zeeman splitting of the initial and final states of the $R(15/2)_{1/2}$ absorption line are nearly equal and the $\Delta M = +1$ (or -1) transitions between the different Zeeman components of $J = 15/2$, $v = 0$ and $J = 15/2$, $v = 1$ have approximately the same frequency. The actual dependence of g_J on J produces a spread of about 40 MHz in the strong components for a field of 30 kG. A plot (open circles) of the absorption line centers (derivative zeroes) as a function of magnetic fields is shown in Fig. IV-6(a). These data have been corrected for small shifts in the center frequency of the laser, which occur from run to run as the result of drifts in the thermal circuitry of the laser mount. The data of Fig. IV-6(b) agree very well with the calculated line center positions given by the solid lines. These positions were calculated using the theoretical g_J (≈ 0.028), the Doppler lineshape and the relative Zeeman intensities for a symmetric top molecule.¹⁵ Again, no significant vibrational effect is observed.

A derivative Zeeman spectrum for the $R(15/2)_{3/2}$ line is shown in Fig. IV-7(b) for a magnetic field of 30.5 kG. Although this line appeared single for zero magnetic field, it now has fourteen major components. This high multiplicity stems from the strong dependence of g_J on J for $^2\Pi_{3/2}$ rotation levels ($g_{15/2} = 0.019$, while $g_{17/2} = 0.0095$). This splits the degeneracy of the various components of the $\Delta M = +1$ (or -1) transitions. There are, in principle, $2(2J + 1) = 32$ possible Zeeman lines. Twenty-eight of these lines form nearly degenerate pairs, split by an amount small compared to the Doppler width. The remaining four lines are about one hundred times weaker and are not detected in the trace of Fig. IV-7(b). The measured line positions of the fourteen strong lines are shown (open circles) as a function of magnetic field in Fig. IV-7(a). Again, the solid lines give the calculated positions based on the linear Zeeman effect. The data show good agreement with the calculated lines for small magnetic fields and a small but systematic deviation at the highest field. This deviation may arise from second order (H^2) Zeeman effects.

In addition to the Zeeman spectra of Fig. IV-6 and Fig. IV-7 (see Sec. IV-D-3), a high resolution study has been made of the magnetic rotation spectra of $R(15/2)$. Preliminary measurements have also been made of Lambda doubling and Zeeman splitting of lines in the Q branch of NO. This work is continuing.

K. W. Nill A. R. Calawa
F. A. Blum T. C. Harman

3. Infrared Magnetic Rotation in NO

The resolution of observed magnetic rotation spectra¹⁷ in gases, including nitric oxide,¹⁸⁻²¹ has been instrument-limited in the past. Using a CW, current tunable $PbS_{0.62}Se_{0.38}$ semi-conductor diode laser, the magnetic rotation spectrum of the $R(15/2)_{1/2}$ absorption line in the fundamental ($v = 0 \rightarrow v = 1$) vibration-rotation band of NO has been fully resolved. The magnetic rotation spectrum is a plot of the frequency dependence of the transmission of the laser radiation through a gas cell which is placed between crossed (90°) linear polarizers. Since the polarizers are crossed, no signal is detected unless the gas is optically active. The NO is rendered optically active by placing the cell in a magnetic field which is parallel to the direction of propagation of the radiation.

Figure IV-8 shows a comparison of the absorption profile (a) and the magnetic rotation transmission (b) of the $R(15/2)_{1/2}$ line of NO for a magnetic field of 30 kG and a pressure of 3 torr.

Section IV

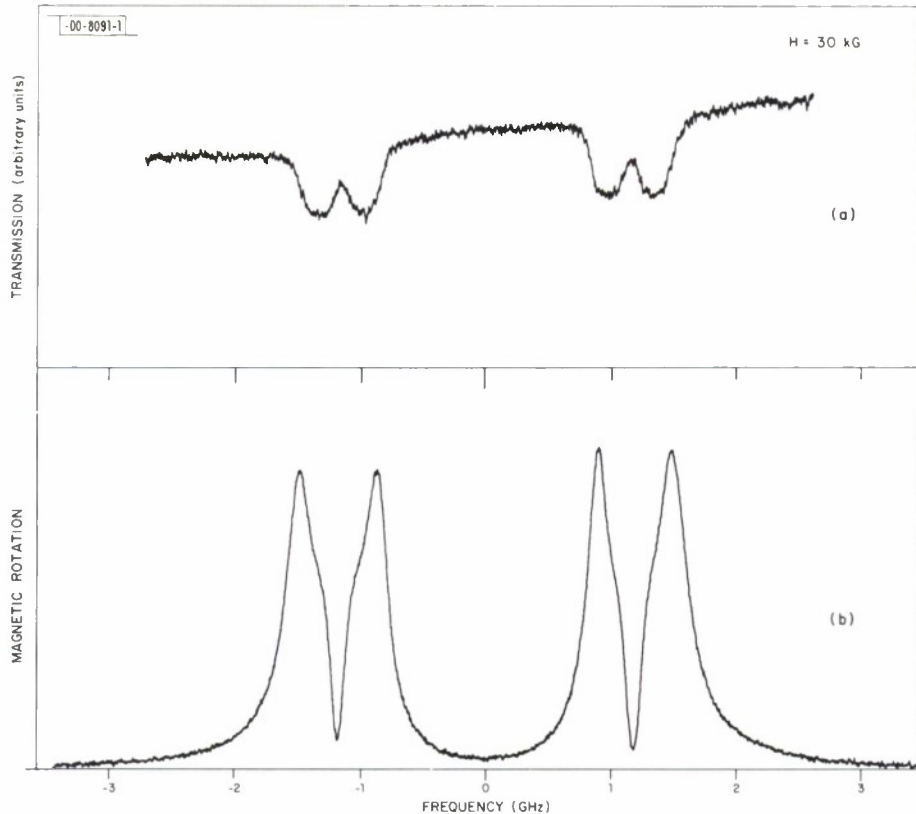


Fig. IV-8. For the $R(15/2)_{1/2}$ line of NO: (a) transmission through 4 cm of NO at 3 torr in a longitudinal magnetic field of 30 kG; (b) magnetic rotation spectrum under the same conditions.

There are four Zeeman components because the zero field line is Λ -doubled with a splitting of 324 MHz (see Sec. IV-D-2). The center of this spectrum lies near 1903.1 cm^{-1} . The observed lineshapes are fully resolved, since the laser linewidth is estimated to be $< 1 \text{ MHz}$, which is small compared with the Doppler linewidth of 129 MHz. The data were taken with a gas cell of 4 cm length placed in the bore of a 100-kG superconducting magnet. The magnetic field was homogeneous over the cell volume within ± 1.5 percent. Note the unusual asymmetry in the individual components of the magnetic rotation spectrum and the resolved Zeeman components. In previous studies¹⁷⁻²¹ of magnetic rotation in gases, the individual Zeeman components and their specific lineshape have not been resolved. The observed lineshape derives from two contributions to the magnetic rotation signal which are due to (1) magnetic circular birefringence (Faraday rotation) and (2) magnetic circular dichroism. A calculation of the predicted magnetic rotation spectrum, based on the observed absorption spectrum, is under way.

F. A. Blum A. R. Calawa
K. W. Nill T. C. Harman

4. Laser Light Scattering in Antiferromagnets

To understand the temperature dependence of light scattering which has been observed in antiferromagnets, the Dyson-Maleev graphical perturbation theory has been applied to simple

antiferromagnetic systems. In the problem of two-magnon Raman scattering, previous calculations^{22,23} have been extended to include the simplest class of diagrams which result from using the complete Raman transition operator M in place of the lowest order approximation for M considered previously. Results yield an amplitude renormalization for the Raman cross section which scales as α^2 , where α is the energy renormalization factor of the Hartree-Fock theory. Using a different graphical method, Sólyom^{24,25} had previously obtained an amplitude renormalization factor of $\langle S_a^z \rangle^2$, where $\langle S_a^z \rangle$ is the sublattice magnetization (per spin). Sólyom's result, which predicts a vanishing Raman intensity at the ordering temperature $T_{N'}$, has been proved a consequence of including only the transverse (S^x, S^y) interactions in M . The addition of the longitudinal (S^z) interactions in M leads to the result α^2 , which remains quite finite as $T \rightarrow T_{N'}$.

Also, in an effort to correlate the Raman theory with other magnetic properties, calculations have been made of χ^{zz} , χ_{st}^{zz} and χ_{\perp} , which are the parallel susceptibility, the staggered parallel susceptibility and the perpendicular susceptibility, respectively. The most interesting area of investigation here concerns application to two-dimensional magnetic systems, e.g., K_2NiF_4 , where χ^{zz} exhibits a broad maximum extending well above $T_{N'}$, and where χ_{st}^{zz} is expected to have a Stanley-Kaplan²⁶ singularity even in the absence of anisotropy. Investigations of this singularity appear to be unique in that they are based on spin wave theory, as contrasted to the high temperature expansion methods of Stanley and Kaplan. Details of these calculations will be presented in a later report.

R. W. Davies
S. R. Chinn
H. J. Zeiger

E. ELECTRONIC BAND STRUCTURE

1. Infrared Laser Determination of Effective Mass in GaAs-InAs Alloys

Previous estimates²⁷ of the effective mass of conduction electrons in $Ga_{1-x}In_xAs$ alloys have been made on the basis of near-infrared reflectivity measurements. The first determination of the bottom of the band effective mass, m^* , via cyclotron resonance in thin epitaxial films is reported. Carrier concentrations in the single crystal samples ranged from 2.3×10^{14} to 2.5×10^{15} e/cm³ as x was varied from 0 to 15.7 percent. The measurements, made in both photoconductivity and transmission at 4.2° K using the 119-μm H_2O laser, are corrected for non-parabolic effects and plotted in Fig. IV-9. Evidence indicates that the electrons in the conduction band at these temperatures arise from the photoionization of shallow donors.

Although theory²⁸ predicts that m^* should have a dependence similar to the energy gap E_g , an almost linear variation with alloy concentration was observed. Recent experiments²⁹ and calculations³⁰ have indicated a nonlinear behavior of E_g . Further experiments at longer wavelengths (337 and 311 μm) are in progress to investigate this relationship.

In the course of these experiments, the cyclotron resonance at 119 μm in pure GaAs was observed with extremely high resolution. It was found to consist of a double absorption line split by 157 G, as shown in Fig. IV-10. This is attributed to the effects of non-parabolicity on the spin-split Landau levels and should yield a value for the effective g-factor in GaAs.

H. R. Fetterman P. E. Tannenwald
J. Waldman C. M. Wolfe

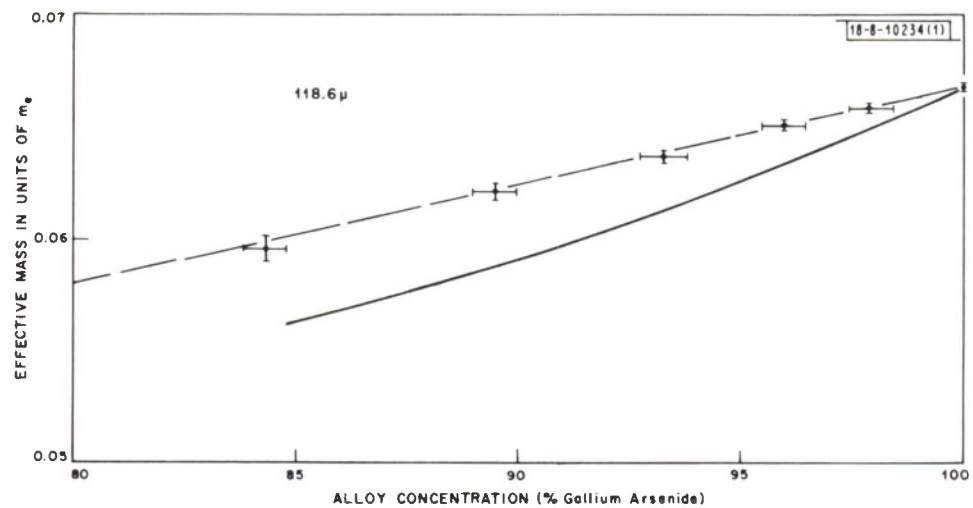


Fig. IV-9. Effective masses of $\text{Ga}_{1-x}\text{In}_x\text{As}$ corrected for nonparabolic effects. Dashed curve indicates linear variation between pure GaAs and InAs. Solid line indicates predicted behavior using experimentally determined values for the energy gap.

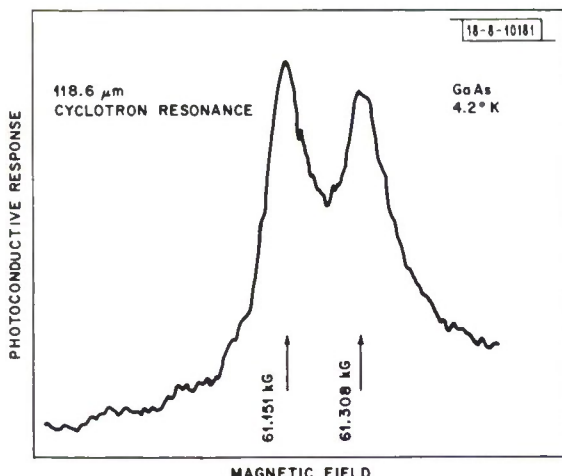


Fig. IV-10. Cyclotron resonance of pure GaAs ($n = 1.29 \times 10^{14} \text{ e/cm}^3$) taken at 4.2°K with $118.59\text{-}\mu\text{m}$ radiation. Bias = 70 nA.

2. Resistivity of $Pb_{1-x}Sn_xSe$ Under Hydrostatic Pressure

The resistivity of $Pb_{1-x}Sn_xSe$ alloys as a function of pressure is expected to pass through a minimum where the energy gap goes through zero and the bands invert. This effect has been studied at 4.2°, 77° and 195° K in n- and p-type samples with compositions $x = 0.17$ and 0.20 and carrier concentrations from 2×10^{17} to $2 \times 10^{18} \text{ cm}^{-3}$. The results, Fig. IV-11, show a surprising feature: the pressure at which a minimum in resistivity is reached depends on carrier density and appears to have the opposite dependence for n- and p-type samples; i.e., increasing hole concentration shifts the minimum to higher pressure, while increasing electron concentration shifts the minimum to lower pressure. Furthermore, at 4.2° K the samples with $x = 0.17$ and 0.20 are believed to be beyond the band crossing point,³¹ so that the application of pressure would increase the band gap. Still, high concentration p-type samples show a minimum. For low concentration p-type and for all n-type samples, the resistivity increases with pressure, as expected.

At 4.2° and 77° K the variation in resistivity, $\rho (= 1/ne\mu = m^*/ne^2\tau)$, is due to the variation of mobility μ with pressure. Hall constant and Shubnikov-de Haas measurements indicate that the carrier concentration n is independent of pressure.[†] These shifts in the resistivity minima are thought to involve the higher-band interactions.

J. Melngailis J. A. Kafalas
T. C. Harman W. C. Kernan

[†] At 195°K the Hall constant changes with pressure. For sample 4-17c the resistivity at the minimum, at 6 kbars, falls to about 40 percent of the atmospheric pressure value, while the Hall constant falls to about 80 percent of its atmospheric pressure value.

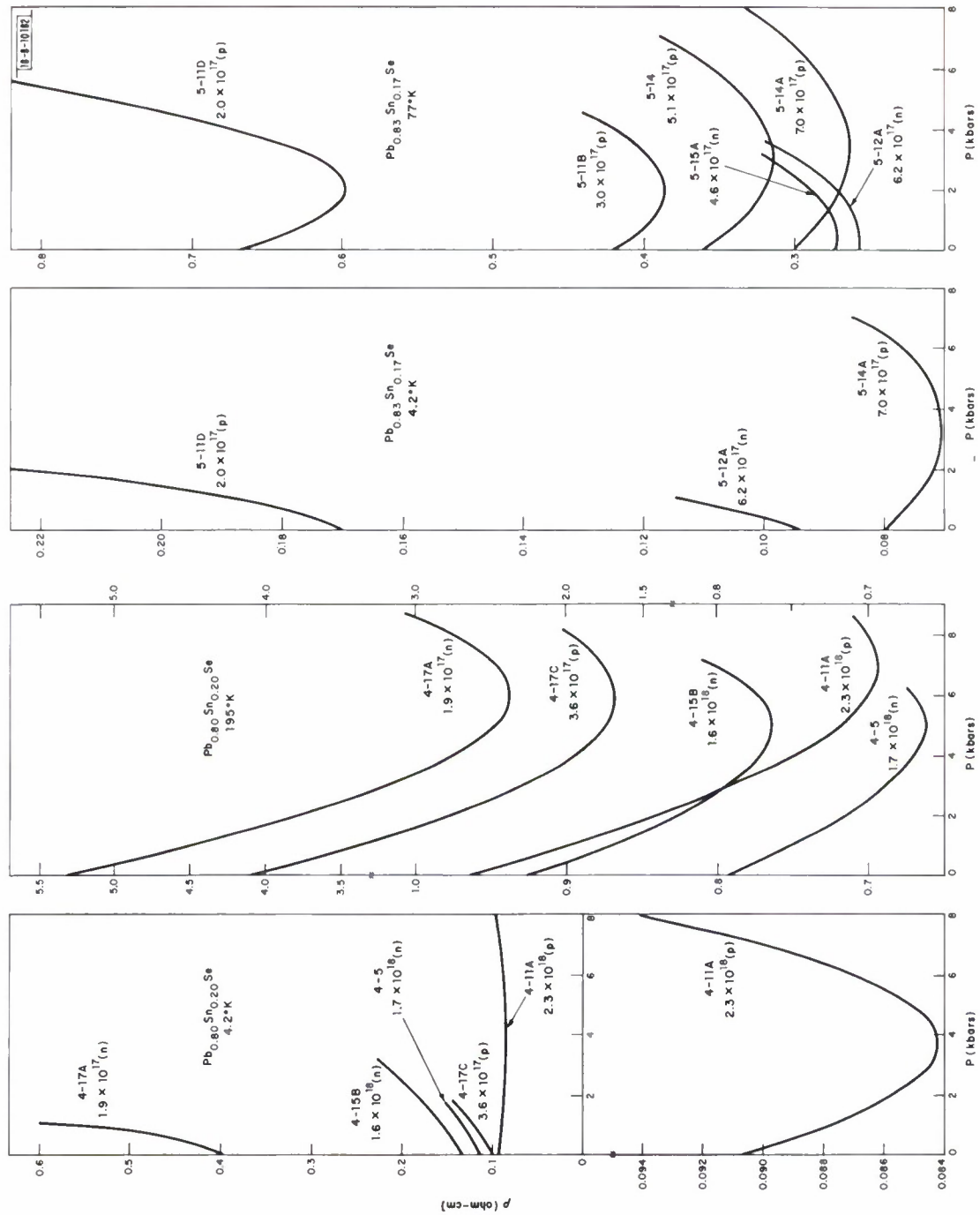


Fig. IV-11. Resistivity (in mohm-cm) of $\text{Pb}_{1-x}\text{Sn}_x\text{Se}$ samples as a function of pressure. Each curve is labeled by sample number, carrier concentration (cm^{-3}) and type. The 77°K results for the $\text{Pb}_{0.80}\text{Sn}_{0.20}\text{Se}$ samples (not shown) are qualitatively the same as the 4.2°K results; i.e., only the high concentration p-type sample has a minimum.

REFERENCES

1. A. J. Dekker in Solid State Physics, Vol. 6, F. Seitz and D. Turnbull, Eds. (Academic Press, New York, 1958), p. 251.
2. H. Bruining in Physics and Applications of Secondary Electron Emission (Pergamon Press, New York, 1954), p. 35.
3. J. E. Geusic, F. W. Ostermayer, H. M. Marcos, L. G. Van Uitert and J. P. van der Ziel, J. Appl. Phys. 42, 1958 (1971).
4. S. Shionoya in Proceedings of the 1969 International Conference on Luminescence, F. Williams, Ed. (North-Holland, Amsterdam, 1970), p. 17.
5. N. Riehl in Proceedings of the 1969 International Conference on Luminescence, F. Williams, Ed. (North-Holland, Amsterdam, 1970), p. 1.
6. T. B. Reed, Free Energy of Binary Compounds (M. I. T. Press, 1971).
7. H. J. Zeiger, T. A. Kaplan and P. M. Raccah, Phys. Rev. Letters 26, 1328 (1971), DDC AD-729576.
8. Solid State Research Report, Lincoln Laboratory, M. I. T. (1971:2), p. 5, DDC AD-732923; K. W. Nill, F. A. Blum, A. R. Calawa and T. C. Harman, Appl. Phys. Letters 19, 79 (1971).
9. Solid State Research Report, Lincoln Laboratory, M. I. T. (1971:3), p. 7, DDC AD-731547.
10. D. H. Rank, D. P. Eastman, B. S. Rao and T. A. Wiggins, J. Mol. Spectry. 10, 34 (1963).
11. R. H. Hunt, R. A. Toth and E. K. Plyler, J. Chem. Phys. 49, 3909 (1968).
12. D. B. Keck and C. D. Hause, J. Mol. Spec. 26, 163 (1968).
13. L. L. Abels and J. H. Shaw, J. Mol. Spec. 20, 11 (1966).
14. J. J. Gallagher and C. M. Johnson, Phys. Rev. 103, 1727 (1956); J. J. Gallagher, F. D. Bedard and C. M. Johnson, Phys. Rev. 93, 729 (1954).
15. G. C. Dousmanis, T. M. Sanders and C. H. Townes, Phys. Rev. 100, 1735 (1955).
16. C. H. Townes and A. L. Schawlow, Microwave Spectroscopy (McGraw-Hill, New York, 1955), p. 256.
17. A. D. Buckingham and P. J. Stephens, Ann. Rev. Phys. Chem. 17, 399 (1966) and references therein.
18. G. A. Mann and C. D. Hause, J. Chem. Phys. 33, 1117 (1960).
19. J. L. Aubel and C. D. Hause, J. Chem. Phys. 44, 2659 (1966).
20. D. W. Robinson, J. Chem. Phys. 46, 4525 (1967); 50, 5018 (1969).
21. D. B. Keck and C. D. Hause, J. Chem. Phys. 49, 3458 (1968).
22. R. W. Davies, S. R. Chinn and H. J. Zeiger, Phys. Rev. B 4, 992 (1971), DDC AD-731947
23. S. R. Chinn, R. W. Davies and H. J. Zeiger, Phys. Rev. B 4, 4017 (1971).
24. J. Sólyom, Zeits für Phys. 243, 382 (1971).
25. _____, Proc. Int'l. Conf. Light Scattering Spectra of Solids, Paris, 1971 (to be published).
26. H. E. Stanley and T. A. Kaplan, Phys. Rev. Letters 17, 913 (1966), DDC AD-646485; J. Appl. Phys. 38, 975 (1967), DDC AD-655326.
27. E. F. Hockings, I. Kudman, T. E. Seidel, C. M. Schmelz and E. F. Steigmeier, J. Appl. Phys. 37, 2879 (1966).
28. J. C. Woolley and A. G. Thomson, Can. J. Phys. 42, 2030 (1964).
29. William M. Coderre and J. C. Woolley, Can. J. Phys. 48, 463 (1970).
30. D. Jones and A. H. Lettington, Solid State Commun. 7, 1319 (1969).
31. A. R. Calawa, J. O. Dimmock, T. C. Harman and I. Melngailis, Phys. Rev. Letters 23, 7 (1969), DDC AD-694137.

V. MICROELECTRONICS

A. ALUMINUM INTERCONNECTIONS AND BEAM LEADS ON POLYIMIDE-COATED, THIN, COPPER SUBSTRATES

The technology for fabricating beam-leaded substrates utilizing polyimide-coated copper has been extended to include multilevel aluminum interconnections. The polyimide, applied as a negative photoresist which is imidized after exposure and development by heating at 250° C for 20 minutes in N₂, is used to isolate all the interconnections from the copper substrate and to isolate the different levels of aluminum from one another.

The processing sequence, as reported in the previous issue of this report,* is amended as follows for two-level metalization.

- (1) Coat the substrate with 9000 Å of polyimide, photolithographically patterning the coating to include the appropriate chip apertures.
- (2) Evaporate 20,000 Å of aluminum over the substrate and photolithographically form the crossunder metalization.
- (3) Coat the substrate with 9000 Å of polyimide, photolithographically patterning the coating to include both the chip apertures described in Step 1 and the vias for interconnecting the crossunder metalization and the basic interconnecting metalization.
- (4) Evaporate 125,000 to 150,000 Å of aluminum onto the substrate and photolithographically form the interconnections and beam leads.
- (5) Etch the chip apertures in the copper substrate.
- (6) Sinter the aluminum-to-aluminum contacts by heating the substrate at 250° C in N₂ for 10 minutes.

F. J. Bachner

B. SEMICONDUCTOR PROGRAM

Electron-Beam-Irradiated Diodes (E-Birds):- The fabrication of n-diffused p-type diodes has been emphasized recently and, because of the high resistivity required, there is considerable susceptibility to inversion during normal oxidation. C-V plots of the initial oxidation show an inversion layer formed on the high resistivity p-type silicon. As expected, the same procedure applied to high resistivity n-type silicon shows no inversion and also very low surface state density – on the order of high 10¹⁰ to low 10¹¹ Q_{SS}. Thus, clean processing alone does not solve the surface inversion problem with high resistivity p-type silicon. Inversion is due primarily to the low concentration of the p-type surface being converted to n-type by removal of p-type dopant atoms by the advancing SiO₂ front. Three methods to reduce this effect were pursued.

- (1) Sputtered oxide was used in place of thermal oxide and, although the device had no apparent channels, the breakdown voltage was reduced to 110 to 120 V from the theoretical value of 250 V. The reduction in voltage appears to be caused by small amounts of contamination involved in the cleaning, etching and sputtering processes, since the device junctions are exposed prior to sputtering. A modification of this technique was then tried by

* Solid State Research, Lincoln Laboratory, M.I.T. (1971:3), p. 48, DDC AD-731547.

sputtering SiO_2 for the initial oxidation, thereby preventing the junctions from being exposed during the process. The channels were again eliminated and the breakdown voltage increased to 140 to 160 V, but was still less than the theoretical 250 V, presumably due to slight contamination of the surface before and/or during sputtering. A further modification was tried in which a thin layer (50 Å) of thermal SiO_2 was grown before the sputtered oxide was deposited. No channels occurred, but again reduced breakdown voltage (140 to 160 V) resulted.

- (2) A second approach employed a thin layer of boron deposited over the entire wafer before the initial oxidation. It was hoped that by supplying additional boron a compensation for the subsequent loss of boron during oxidation would be sufficient to prevent inversion. Of course, the danger here is that if too much boron is added the breakdown voltage will decrease due to the increase in surface concentration. Results on the finished devices were excellent in that the channels were eliminated and the theoretical breakdown voltage of 250 V was obtained.
- (3) An extra diffusion "channel stopper" was carried out in the form of a ring around the device of the same polarity as the wafer, i.e., n-type. The ring, although not eliminating channels, should reduce them extensively by allowing the channel to spread from the p-n junction only to the channel-stopper ring, rather than over the entire surface of the die. This proved successful. Finished devices exhibited no channel leakage ($<1 \mu\text{A}$ on Tektronix 576 scope) and the theoretical breakdown voltage of 250 V was achieved.

The resulting experimental devices are presently being mounted, bonded and tested in the 10 to 15 kV electron beam. Samples of the new package using the complete shield, which prevents the electron beam from contact with the device except in the active region, have been received. Thermal resistance measurements show that Au-Si eutectic mounting produces $\leq 1^\circ\text{C}/\text{W}/\text{unit}$.

Nuclear Particle Detectors:- Several detectors have been made with 20 diodes, each 1 mil wide, 50 mils long, and with a 1-mil separation on both sides of a 2-mil-thick, 30,000-ohm-cm silicon wafer. Although the diode yield is excellent, the chip yield is considerably reduced due to the losses incurred in handling the thin wafers. Breakdown voltages of 700 to 900 V are typical, while depletion voltage is desirably low at 17 V. The devices have been packaged and electrically tested and are awaiting the beta-particle bombardment test to determine detector resolution and stability of the junction under nuclear-particle bombardment.

Diode Matrix:- A 10×10 programmable diode matrix has been completed. The matrix incorporates diffusion isolation and employs metal fuses for programming. Diodes have a 35 V_R and fuses blow at the expected $3/4 \text{ A}$. The worst case series resistance is 65 ohms. The chip is designed so that other chips can be interconnected to increase the size of the matrix. The yield for individual diodes is >99 percent and for chips, 70 percent. An air gap isolated diode matrix has been designed for applications where lower series resistance is required. It should produce a series resistance of 10 to 20 ohms in the worst case.

Surface Wave Amplifier:- Preliminary results show that localized gold diffusion is effective in reducing the junction resistance between an n^+ contact and near-intrinsic n-type silicon used in these acoustic surface wave amplifiers. With the contact biased positive with respect to the silicon, a space charge region forms around the diffused n^+ region and a substantial fraction of the sample voltage appears across this junction. Introducing gold into the junction area reduces carrier lifetime and appears to eliminate the unwanted junction altogether.

Several other programs on TRAPATT diodes, LSI shallow diffusion transistors, integrated circuits and infrared detectors are in progress.

R. A. Cohen

C. MASK MAKING LABORATORY

Recent efforts in the mask making laboratory have been concentrated in three areas:

- (1) Making masks with extremely small circular images
- (2) Finding and correcting causes of defects
- (3) Developing a capability for photorepeating on emulsion.

Masks with perfectly round 2- μm -diameter circles have been produced by starting with hexagons at 100X. These hexagons were generated by the pattern generator, reduced to 10X and photorepeated. This 10X array was again reduced and repeated to produce the final circular images. The plates used for the final reduction were 0.060-inch-thick glass plates coated with chrome and 0.35 μm of Shipley AZ1350 photoresist. The resulting masks have been used successfully for fabricating millimeter wave gallium arsenide mixer diodes.

Mask yield has been quite low because of an excessive number of defects, primarily pin-holes. Some of these problems have been traced to defects in the 10X master reticle. This source of defects has almost been eliminated by carefully cleaning and inspecting the reticle immediately before mounting it on the photorepeater. Also, the use of dark-field reticles should reduce the susceptibility to this type of defect.

Another cause of defective masks has been imperfections in the emulsion on the photographic plates. A technique for visual inspection of these plates under safe-light conditions was developed. This inspection procedure reduces the incidence of defective masks caused by imperfect plates.

Until recently, all photorepeater work had been done on chrome plates. The 5-sec exposure time required made it take around 45 minutes to photorepeat a plate. On the other hand, emulsion was exposed "on the fly" by a Xenon flash, which results in a running time of approximately 15 minutes per mask. In addition, chrome plates cost 10 to 20 times as much as emulsion and are more difficult to develop and etch. For these reasons, it was decided to photorepeat on emulsion all masks whose critical dimensions are larger than 5 μm and which do not require the higher resolution of chrome. If the user requires a chrome mask for durability, the emulsion step-and-repeat master can be contact printed onto chrome. Although start-up problems have been experienced, this change in procedure should eventually improve our operating efficiency and thereby reduce turnaround time.

A new contact printer, stable tables and laminar flow benches have been delivered. This should further improve our capabilities and yield. However, installation is being delayed by difficulties in obtaining the space changes necessary to accommodate the new equipment.

D. L. Smythe, Jr.

D. BONDING AND PACKAGING

E-Bird Units:- Work continues to improve the power-handling ability of these units in the area of bonding. Methods are being explored to reproducibly make void-free bonds to optimize the heat transfer characteristic of the package.

Section V

Prototypes of a studded package design have been received and examined. Metalization of the ceramic ring is required to permit evaluation of this packaging design.

Nuclear Particle Detector:- Several detectors have been bonded and packaged for initial test. Each device has 20 beam leads on the underside of the chip and 20 wire-bond connections on the top surface. It is a 70×74 mil chip 2 mils thick with a slight overhang at the edges. Thus, the chip is very fragile and fractures easily under the light bonding tool pressure. Among the procedures considered for minimizing breakage was the use of a small amount of epoxy under the chip edge. The grains of the available epoxies were too large to fit into the extremely small void, but a survey disclosed the availability of an epoxy, Epotek H54, which met our requirements. Careful deposition of a thin thread of this epoxy supports the edge of the chip and permits wire bonding from the pads to the substrate of the package.

LES Limiter:- Five hybrid limiter circuits have been completed for Group 69. The circuit layout, component placement layout and alumina substrate fabrication were handled in Group 87. The close spacing, which results from the number and size of parts to be positioned on a TO-8 header, required that transistors and diodes be eutectically bonded, while the substrate and other parts were attached with either silicon- or gold-filled epoxy. All devices met initial electrical requirements satisfactorily.

T. F. Clough

E. INTEGRATED CIRCUIT TESTING

The laser scanner system for testing monolithic integrated circuits has been modified to accommodate an additional laser beam for dynamic testing. The additional laser beam is used to exercise the various logic states of the integrated circuit by selectively turning on various transistors. Since the base impedance of most bipolar integrated circuit transistors is in the range of 1 to 5 kohm, the laser beam used for exercising purposes must produce an equivalent circuit current of about 0.2 to 1 mA. Typically, this requires a laser beam of about 10 to 30 mW at the chip, but because of losses in the optics, the input laser power is about 90 mW.

As each new logic state is implemented by the localized laser, the circuit is scanned with the 4-mW scanning laser and electrical data is derived from the resulting video signal or planar oscilloscope presentation. The electrical data available includes information on the degree of saturation for transistors in the "on" state and the threshold sensitivity and relative leakage current of transistors in the "off" state. The localized laser is also being used experimentally to bias transistors into the active region so that their gain can be differentially determined by the scanning laser.

R. E. McMahon
W. H. McGonagle

UNCLASSIFIED

Security Classification

DOCUMENT CONTROL DATA - R&D

(Security classification of title, body of abstract and indexing annotation must be entered when the overall report is classified)

1. ORIGINATING ACTIVITY (Corporate author) Lincoln Laboratory, M.I.T.	2a. REPORT SECURITY CLASSIFICATION Unclassified
	2b. GROUP None

3. REPORT TITLE

Solid State Research

4. DESCRIPTIVE NOTES (Type of report and inclusive dates)

Quarterly Technical Summary - 1 August through 31 October 1971

5. AUTHOR(S) (Last name, first name, initial)

McWhorter, Alan L.

6. REPORT DATE 15 November 1971	7a. TOTAL NO. OF PAGES 84	7b. NO. OF REFS 90
8a. CONTRACT OR GRANT NO. F19628-70-C-0230	9a. ORIGINATOR'S REPORT NUMBER(S) Solid State Research (1971:4)	
b. PROJECT NO. 649L	9b. OTHER REPORT NO(S) (Any other numbers that may be assigned this report) ESD-TR-71-300	
c. d.		

10. AVAILABILITY/LIMITATION NOTICES

Approved for public release; distribution unlimited.

11. SUPPLEMENTARY NOTES None	12. SPONSORING MILITARY ACTIVITY Air Force Systems Command, USAF
-------------------------------------	---

13. ABSTRACT

This report covers in detail the solid state research work of the Solid State Division at Lincoln Laboratory for the period 1 August through 31 October 1971. The topics covered are Solid State Device Research, Quantum Electronics, Materials Research, Physics of Solids and Microelectronics. The Microsound work is sponsored by ABMDA and is reported under that program.

14. KEY WORDS

solid state devices quantum electronics materials research microelectronics	infrared photo diodes laser spectroscopy Raman scattering	semiconductor x-ray lithography magneto-optical research crystal growth
--	--	--